c.1

MAGNETIC FEEDBACK AND QUANTUM OSCILLATIONS IN METALS

by

ANDRÉ JOHN VAN SCHYNDEL

B.Sc., McMaster University, 1978

A THESIS SUBMITTED IN PARTIAL FULFILMENT OF

THE REQUIREMENTS FOR THE DEGREE OF

MASTER OF SCIENCE

in

THE FACULTY OF GRADUATE STUDIES

Department of Physics

We accept this thesis as conforming

to the required standard

THE UNIVERSITY OF BRITISH COLUMBIA

October 1980

In presenting this thesis in partial fulfilment of the requirements for an advanced degree at the University of British Columbia, I agree that the Library shall make it freely available for reference and study. I further agree that permission for extensive copying of this thesis for scholarly purposes may be granted by the Head of my Department or by his representatives. It is understood that copying or publication of this thesis for financial gain shall not be allowed without my written permission.

Department of PHYSICS

The University of British Columbia
2075 Wesbrook Place
Vancouver, Canada
V6T 1W5

Date OCT. 10 1980

ABSTRACT

A feedback technique is presented for the reduction of the Shoenberg magnetic interaction in metals. The method allows the spin splitting parameter g_c for extremal orbits on the Fermi surface to be obtained from de Haas-van Alphen measurements, now essentially free from the oft-times severe distortions resulting from magnetic interaction. The feedback technique also offers several advantageous side effects, the most important one being a simple and reliable method for determining absolute amplitudes of de Haas-van Alphen oscillations. Explicit formulae are derived showing the dependence of several key observable quantities on the amount of magnetic feedback, and these formulae are found to be in good agreement with experiment. The technique is applied to the determination of g_c for the [110] γ oscillations in Pb.

TABLE OF CONTENTS

	page
Abstract	ii
Table of Contents	iii
List of Tables	v
List of Figures	vi
Acknowledgements	viii
CHAPTER I - INTRODUCTION	1
CHAPTER II - SPIN SPLITTING OF LANDAU LEVELS	5
CHAPTER III - THE SHOENBERG MAGNETIC INTERACTION EFFECT	13
CHAPTER IV - REDUCTION OF MAGNETIC INTERACTION USING A FEEDBACK TECHNIQUE	20
CHAPTER V - EXPERIMENTAL DETAILS	27
5.1 Sample Preparation	27
5.2 Detection Apparatus	31
5.3 Modulation Coil and Superconducting Magnet	36
5.4 Cryogenic Apparatus	37
5.5 Signal Processing	39
CHAPTER VI - EXPERIMENTAL TEST OF THE FEEDBACK TECHNIQUE	50
6.1 Preliminary Considerations	50

page

6.2 Minimization of Sidebands.... 52

6.3 The Mass Plots 62

6.4 The Beat Pattern 69

6.5 Phase Information 86

6.6 The Linearity of A_1/A_3 vs. $(A_1/A_2)^2$ 91

6.7 Conclusions 91

CHAPTER VII - EXTRACTION OF THE g_c FACTOR FROM A_1/A_3 vs. $(A_1/A_2)^2$ 94

CHAPTER VIII - A SEARCH FOR THE 4 MG OSCILLATIONS.. 99

8.1 Preliminary Remarks 99

8.2 Review of the Standard Weak Modulation Solution 100

8.3 Large Modulation 103

8.4 Modification to the Apparatus and Analysis for the F $\sim$ 4MG Search 112

APPENDIX A: Flexible Gear Rotator 114

APPENDIX B: The Discrete Fourier Transform 119

APPENDIX C: Computer Programs 122

BIBLIOGRAPHY 134

LIST OF TABLES

		page
I	Fourier Coefficients p, q	16
II	Effective Mass for Observed Oscillations in Pb:H$\|\|$/[110]...	64
III	Ranking the Terms	109

LIST OF FIGURES

FIGURE		page
1.	The Spin-split Magnetization at Absolute Zero	9
2.	The dHvA Magnetization at Finite Temperature	10
3.	Crystal Diameter as a Function of Melt Heater Voltage	28
4.	Detection Arrangement	34
5.	General Schematic Cryogenic Assembly	38
6.	Fine Tuning Circuit	40
7.	Equivalent Circuit for Tuning Arm	40
8.	Block Diagram of Apparatus	44
9.	Circuit Diagram of Integrator and Adder	45
10.	Synchronization of the Time Window	48
11.	dHvA Oscillations in Lead Along [110]	51
12.	Fourier Transforms Around 160 MG	53
13.	Fourier Amplitudes as a Function of Feedback Gain	54
14.	Mass Plots with No Feedback	65
15.	Mass Plots with Near-Optimal Feedback	66
16.	Mass Plots at Optimum Feedback	70
17.	Beat Envelopes with No Feedback	73
18.	Beat Envelope with Near Optimum Feedback	74
19.	Calculation of Apparent Beat Periods	79

		page
20.	Calculated Solutions for A_2	80
21.	The Beat Envelope with Optimum Feedback ...	84
22.	Ideal L.K. Beat Envelope	85
23.	Individual Oscillations at the "Magic Field"	88
24.	Individual Oscillations at $1/H_2$ of Figure 22	89
25.	Phase Difference and Amplitude of A_2 at a "Magic Field"	90
26.	A_1/A_3 vs. $(A_1/A_2)^2$ with and without Feedback	92
27.	Fundamental γ Beat Envelope	97
28.	Sample Rotator Assembly	115
29.	Sample Rotator Assembly with Driving Gear and Coil Former	117

ACKNOWLEDGEMENTS

It is a sincere pleasure to thank Dr. A.V. Gold for his support and direction in the supervision of this work, and his close personal interest in providing advice and encouragement.

I am grateful to the National Sciences and Engineering Research Council for their financial support in the form of a Postgraduate Scholarship.

CHAPTER ONE

INTRODUCTION

In 1930, de Haas and van Alphen noticed that the magnetization of bismuth oscillated as a function of an externally applied magnetic field at low temperatures. This remained a laboratory curiosity for almost 20 years until it was realized that this de Haas-van Alphen (dHvA) effect could be used as a powerful tool in the study of the Fermi surface of metals. Valuable information on the detailed shape of the Fermi surface can be obtained from the frequency of the magnetization oscillations in the inverse field domain, and it was soon found that the oscillations are exhibited by most metals in the periodic table.

There is also a wealth of information contained in the harmonic content of the oscillations, in particular about the spin properties of conduction electrons. Amplitude measurements of the fundamental frequency component are usually straightforward (although absolute determinations

of the amplitude require great care). However, various difficulties are encountered when studying the higher harmonics and these difficulties often make it well-nigh impossible to obtain meaningful interpretations of the data. The most serious of these difficulties is the significant harmonic distortion caused by the Shoenberg magnetic interaction effect.

In this thesis, we present an original technique for the minimization of the Shoenberg effect, thereby allowing the spin parameters to be determined reliably, and without the use of correction factors. These spin parameters are Landé spin splitting factors g_c appropriate to cyclotron orbits in the metal, and the relation of the factors g_c to the harmonic amplitudes in the dHvA effect is reviewed in Chapter II.

In Chapter III we discuss the magnetic interaction, how it arises, and how it has been dealt with (to a very limited extent) by extraordinarily tedious deconvolution of the experimental data.

In the past, several attempts have been made to reduce the magnetic interaction experimentally, but these have met with only modest success. After summarizing these experimental approaches to the problem, we present in Chapter IV the principles of the feedback technique which is central to this thesis.

Putting the idea of feedback to work in the laboratory is the subject of Chapter VI. The dependences of various key observable quantities on the amount of feedback are calculated, and compared with experiment.

The experimental apparatus used for the feedback measurements is described in detail in Chapter V. This section includes the circuitry which the concepts developed in Chapter IV dictate, along with special design considerations to make the technique simple, practical, and reliable.

Having developed the procedure for obtaining data which are essentially free of magnetic interaction, we present in Chapter VII the first application of the feedback technique to the determination of g_c for the γ oscillations in lead along [110].

Recent observation of oscillations of very long period in lead using sound attenuation and the magneto-resistance (Shubnikov-de Haas effect) prompted a search for similar oscillations in the dHvA effect. The detection of such long period oscillations benefitsgreatly by the use of very large modulation fields, of an amplitude larger than can be treated analytically by existing formulations. In Chapter VIII we derive an exact solution for the response of dHvA oscillations to a modulation field of arbitrary amplitude. This is followed by the details of an experiment in which a concerted but unsuccessful attempt was made to find the long-period oscillations.

Had they been found, the feedback technique would have shown them either to be genuine dHvA oscillations, or oscillations generated by magnetic interaction. The best we could do was place an upper limit on their amplitude in the three major symmetry directions [100], [110], and [111].

We conclude with some suggestions for further work, both in the technique itself, and its application.

CHAPTER TWO

SPIN SPLITTING OF LANDAU LEVELS IN METALS

In the same year as de Haas and van Alphen's discovery Landau (1930) independently remarked that the magnetization of a metal would be expected to show oscillations because of the quantization of the helical orbits of the conduction electrons.

Onsager (1952) predicted on the basis of general semi-classical arguments that the periodicity was simply related to extremal areas of the Fermi surface normal to the magnetic field. Shortly thereafter Lifshitz and Kosevich (1955) confirmed Onsager's prediction and proceeded to work out expressions for the amplitudes of the oscillations. The result of this rather beautiful work, with some modifications by Dingle, (1952) is equation [1], the general form of the de Haas-van Alphen magnetization:

$$[1a] \qquad \tilde{M} = \sum_{\text{orbits}} \sum_{r} A_r \sin \left[2\pi r\left(\frac{F}{B} - \gamma\right) \pm \pi/4\right]$$

$$[1b] \qquad A_r = r^{-3/2} D(B)(rX/\sinh rX) \exp(-rXT_D/T) \cos(r\pi S)$$

$$[1c] \qquad X = 2\pi^2 m_c^* k_B T/e\hbar B$$

$$[1d] \qquad S = g_c m_c^*/2m$$

The symbol $\tilde{M}$ refers to the oscillating magnetization, and does not include the steady magnetization arising from orbital quantization and spin. The oscillations are periodic in 1/B, and each orbit has its own characteristic frequency F. The phase factor $\pi/4$ is positive for minimal crossectional areas and negative for maxima. D(B) is a function of the magnetic induction, and also of Fermi surface parameters. rX/sinh rX is a measure of the thermal broadening of the quantized orbits. The imperfections of the crystal result in a similar broadening, and are characterized by the Dingle temperature T_D of the crystal.

The factor $\cos(r\pi S) = \cos(r\pi g_c m_c^*/2m)$ is the one of major concern in this thesis since from it g_c itself is determined.

The electron spin will interact with the applied magnetic field symmetrically splitting the Landau levels by

the amount $g\, e \hbar B/2m$, where m is the mass of the free electron. g is a splitting factor which may differ from its free electron value (2.0023) because of spin-orbit-coupling. Each Landau level is thus split, resulting in two sets of levels each separated by $e \hbar B/m^*$, but shifted in phase by the amount $2\pi\ (g\ m^*/2m)$. Each set will give similar oscillations in the magnetization with the same fundamental frequency F, and half the amplitude of that in the absence of spin splitting. In $1/B$, the 2 sets will be displaced from one another by an amount $gm^*/2mF$, so the resulting magnetization will become

$$\frac{1}{2}\ [\tilde{M}(\frac{1}{B} + gm^*/4mF) + \tilde{M}(\frac{1}{B} - gm^*/4mF)].$$

The cosine spin factor in the amplitude expression [1b] follows immediately when this average is applied to a wave-form of the kind given in [1a].

To give a clearer picture of the effect of the spin splitting, let us examine equations [1a]-[1d] at absolute zero ($T=0$) and in a perfect crystal ($T_D=0$). In this case, [1b] reduces to

$$A_r = D(B)\ r^{-3/2} \cos r\pi S$$

which are the Fourier coefficients of a cusplike waveform for $S = 0$. A discontinuous change in the magnetization occurs when the uppermost Landau level becomes depleted as it crosses

the Fermi energy. The effect of cos $r\pi S$ as we have just seen is to sum the contributions from the two sets of Landau levels spin split about the value at S = 0. The two sawtooth waveforms, along with their sum is shown in Figure 1. With a waveform such as that shown in Figure 1, it would be a simple matter to determine the phase shift between the two sawtooth waves, and thereby determine S. At temperatures available to us in the laboratory, the thermal damping factors preferentially reduce the higher harmonics, resulting in a waveform more like that shown in Figure 2, which is an experimental recording taken with typical experimental parameters. The trace is not purely sinusoidal, but it is quite evident that S cannot be measured directly from the waveshape.

To exploit the cos $r\pi S$ dependence in the hopes of extracting the g_c factor from dHvA amplitude data, it would be convenient to obtain a method in which the other amplitude factors played little or no role. Gold and Schmor (1976) showed that with some manipulation of [1b] an algorithm could be obtained using the first three harmonic amplitudes to determine the value S.

Forming the dimensionless quantity $\alpha = A_2^2/A_1A_3$, [1b] gives

[2a] $$\alpha = \alpha_o[1 + 1/3 \tanh^2 X]$$

$$= 3/4\ \alpha_\infty\ [1 + 1/3 \tanh^2 X]$$

where

[2b] $$\alpha_\infty = (\sqrt{3}/2)(1 - \tan^2 \pi S)^2/(1 - 3 \tan^2 \pi S)$$

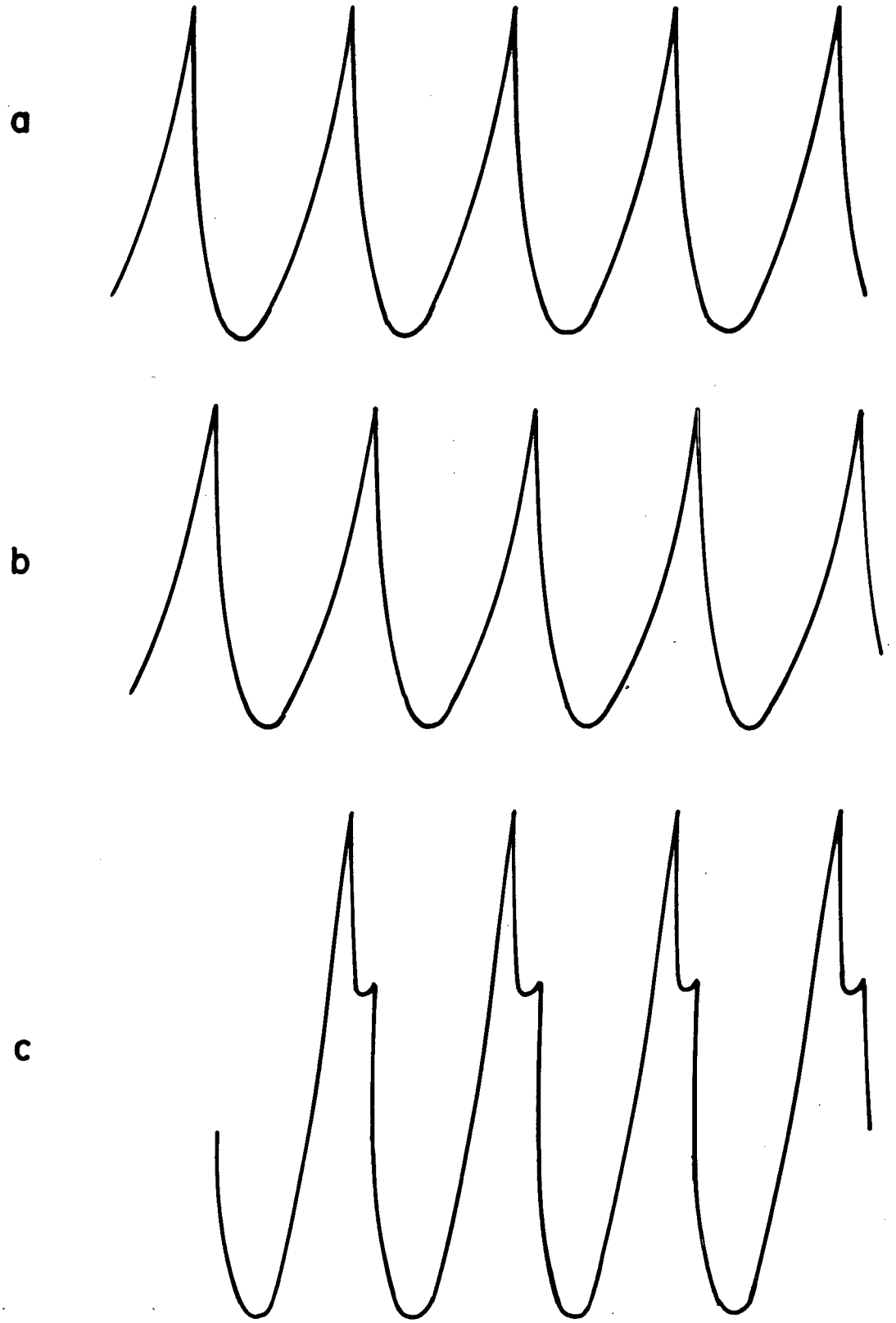

Figure 1. The Spin Split Magnetization at Absolute Zero
a, b : contributions from each of the 2 spin directions c: resultant magnetization

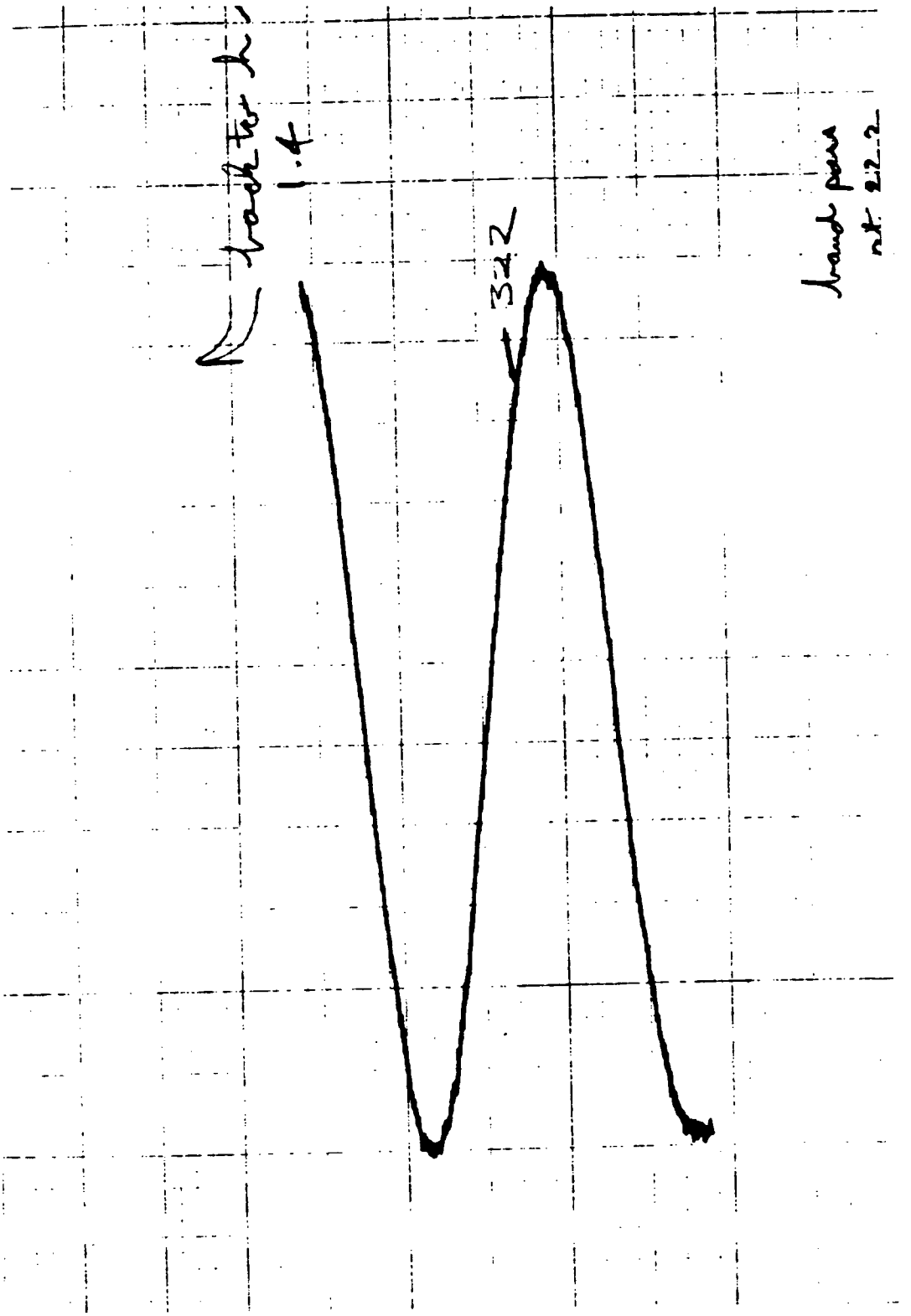

Figure 2. The dHvA Magnetization at Finite Temperature

and the subscripts refer to the limiting cases $X \to 0$ and $X \to \infty$.

Using the harmonic content itself as an implicit gauge of the bath temperature, the hyperbolic functions of X can be eliminated between [1b] for r = 1, 2 and [2a] to give the simple relation

$$[3a] \qquad A_1/A_3 = \alpha_\infty \left[(A_1/A_2)^2 - 1/4 \; (A_1/A_2)_0^2\right]$$

where

$$[3b] \qquad (A_1/A_2)_0 = 2\sqrt{2} \exp (XT_D/T) \cos \pi S/\cos 2\pi S$$

is independent of the temperature T. The value α_∞ can therefore be obtained as the slope of a straight line plot of A_1/A_3 vs. $(A_1/A_2)^2$ as the temperature is varied and the field held constant.

From [2b] it is clear that the solution for S will be obtained from a quadratic equation in $\tan^2 \pi S$ and the solution is therefore multivalued. The physically meaningful solution can be selected with the aid of relative phase measurements and a rough estimate of the Dingle temperature T_D which can be obtained from the field dependence of the fundamental amplitude.

This multivalued nature arises from the fact that we do not know the absolute sign of the harmonic amplitudes. A further multiplicity arises from the periodic nature of $\tan \pi S$ in [2b]. Equivalent solutions are $\pm S \pm p$ where p is an integer. This difficulty is inherent in the use of quantum oscillations to

determine g_c and arises from the periodicity of the cosine in [1b]. One can use a band structure calculation to hopefully resolve the ambiguity.

The three harmonic method offers the major advantage of focusing on the S dependence of the amplitude. Other methods require further information about Fermi surface parameters or scattering rates since complete cancellation of the other amplitude factors is not accomplished.

CHAPTER THREE

THE SHOENBERG MAGNETIC-INTERACTION EFFECT

The discussion in the previous chapter assumed that the oscillations were measured as a function of the magnetic induction B. In practice, the oscillations are measured as a function of the applied field H, related to B by

$$[4] \qquad B = H + 4\pi\ (1-\delta)\ \tilde{M}$$

for a second degree surface with H parallel to a principal axis. δ is the demagnetizing factor. In the normal laboratory situation, $4\pi(1-\delta)\tilde{M}/H \lesssim 10^{-5}$, however since B is in the argument of a rapidly oscillating sinusoid (see [1a]), the correction term often constitutes a large part of one cycle.

The necessity of distinguishing between B and H was first pointed out by Shoenberg (1962).

The substitution of [4] into [1a] results in an implicit equation for $\tilde{M}$ as a function of H, convolving the harmonics into often hopeless contortions, thereby severely modifying the ideal amplitudes A_r and the phases of the harmonics. Recovery of the

ideal amplitudes and phases is the central theme of this thesis.

There are varying degrees of the severity of this magnetic interaction (M.I.). In the limit of small $\tilde{M}$ corrections can be made, but often the distortions are so severe that it is impossible to extract the ideal amplitudes and phases from the data.

To see the effects of the term $4\pi(1-\delta)\tilde{M}$, let us re-write [1] by setting

$$x = 2\pi \left(\frac{F}{H} - \gamma\right) \qquad \kappa = \frac{8\pi^2 F}{H^2}(1-\delta)$$

$$z = \kappa\tilde{M} \qquad C_r = \kappa A_r$$

Since $|4\pi(1-\delta)\tilde{M}| << H$, [1a] becomes

$$[5] \qquad z = \sum_r C_r \sin [r(x-z) \mp \pi/4]$$

This implicit equation for z can be solved by a series of successive approximations in a scheme developed by Phillips and Gold (1969) where the n^{th} approximation is given by

$$z^{(n)} = \sum_{r=1}^{n} C_r \sin [r(x-z^{(n-r)}) \mp \pi/4]$$

and $z^{(0)} = 0$.

While the gathering of terms can become quite tedious after a few steps, the procedure is convenient in that $z^{(n)}$ is exact to $0(n)$ in the amplitude factors.

This scheme has been carried out by Phillips and Gold, and the results are most conveniently displayed as a table of Fourier coefficients p_r, q_r in Table 1, where

$$[6] \qquad \tilde{M}^{(n)} = \sum_{r=1}^{n} [p_r \sin (rx \mp \pi/4) + q_r \cos (rx \mp \pi/4)]$$

The "iteration" scheme has been carried out to many more orders by Perz and Shoenberg (1976) with the aid of a computer program designed to perform the algebraic manipulations.

To obtain the amplitudes of the resulting harmonics A_r' in the interacting theory, we merely find the magnitude of the r^{th} term in the complex Fourier expansion i.e.,

$$A_r' = (p_r^2 + q_r^2)^{1/2}$$

For the first 3 harmonics, the result is

$$[7a] \qquad A_1' = A_1 + 0(3)$$

$$[7b] \qquad A_2' = A_2 \left[1 - \frac{1}{\sqrt{2}} \left(\frac{\kappa A_1^2}{A_2}\right) + \frac{1}{4} \left(\frac{\kappa A_1^2}{A_2}\right)^2\right]^{1/2} + 0(4)$$

$$[7c] \qquad A_3' = A_3 \left[1 - \frac{3}{\sqrt{2}} \left(\frac{\kappa A_1 A_2}{A_3}\right) + \frac{9}{4} \left(\frac{\kappa A_1 A_2}{A_3}\right)^2 - \frac{9}{8\sqrt{2}} \left(\frac{\kappa A_1 A_2}{A_3}\right) \left(\frac{\kappa^2 A_1^3}{A_3}\right) + \frac{9}{64} \left(\frac{\kappa^2 A_1^3}{A_3}\right)^2\right]^{1/2} + 0(5)$$

Term	0(1)	0(2)	0(3)	0(4)
p_1	A_1		$\frac{\kappa A_1 A_2}{2\sqrt{2}} - \frac{\kappa^2 A_1^3}{8}$	
q_1			$\pm \frac{\kappa A_1 A_2}{2\sqrt{2}}$	
p_2		$A_2 - \frac{\kappa A_1^2}{2\sqrt{2}}$		$\frac{\kappa A_1 A_3}{\sqrt{2}} + \frac{\kappa^3 A_1^4}{6\sqrt{2}} - \kappa^2 A_1^2 A_2$
q_2		$\pm \frac{\kappa A_1^2}{2\sqrt{2}}$		$\pm \frac{\kappa A_1 A_2}{\sqrt{2}} \mp \frac{\kappa^3 A_1^4}{6\sqrt{2}}$
p_3			$A_3 - \frac{3\kappa A_1 A_2}{2\sqrt{2}}$	
q_3			$\pm \frac{3\kappa A_1 A_2}{2\sqrt{2}} \mp \frac{3\kappa^2 A_1^3}{8}$	
p_4				$A_4 + \frac{\kappa^3 A_1^4}{3\sqrt{2}} - \frac{2\kappa A_1 A_3}{\sqrt{2}} - \frac{\kappa A_2^2}{\sqrt{2}}$
q_4				$\pm \frac{\kappa A_2^2}{\sqrt{2}} \pm \frac{\kappa^3 A_1^4}{3\sqrt{2}} \pm \frac{2\kappa A_1 A_3}{\sqrt{2}} \mp 2\kappa^2 A_1^2 A_2$

Table 1 Fourier Coefficients p,q. From Phillips and Gold (1969).

We recover the amplitudes A_1, A_2, A_3 of the ideal theory if these amplitudes are sufficiently small.

If, as it often happens, the ideal amplitudes are swamped by the terms generated by M.I., we obtain Shoenberg's "strong-fundamental" results. These are found in [7b] and [7c] by taking the limit as A_2 and A_3 approach zero, the result is

[8a] $$A_1' = A_1 + O(3)$$

[8b] $$A_2' = -\frac{1}{2}\kappa A_1^2 + O(4)$$

[8c] $$A_3' = \frac{3}{8}\kappa A_1^3 + O(5)$$

There are other noticeable effects of M.I., besides the distortion of the harmonic content. If two or more fundamental dHvA frequencies are present, M.I. acts like a mixer, and generates sidebands and combination tones. The simplest of these should be sum and difference frequencies of fundamental oscillations from different orbits on the Fermi surface. If we consider just the fundamentals from two extremal sections, we have (assuming a long rod $\delta = 0$).

[9] $$\tilde{M} = \tilde{M}_a + \tilde{M}_b = A_a \sin\left[2\pi\left(\frac{F_a}{H+4\pi(\tilde{M}_a+\tilde{M}_b)} - \gamma_a\right) \pm \pi/4\right] + A_b \sin\left[2\pi\left(\frac{F_b}{H+4\pi(\tilde{M}_a+\tilde{M}_b)} - \gamma_b\right) \mp \pi/4\right]$$

where the subscripts refer to the two sections.

Since $\frac{F}{H^2}\ [4\pi(\tilde{M}_a + \tilde{M}_b)] << 1$, we can write [9] as

$$[10] \qquad \tilde{M} = A_a \sin (x_a - \kappa_a \tilde{M}) + A_b \sin (x_b - \kappa_b \tilde{M})$$

where $$x_{a,b} = 2\pi\left(\frac{F_{a,b}}{H} - \gamma_{a,b}\right) \mp \pi/4$$

and $$\kappa_{a,b} = \frac{8\pi^2 F_{a,b}}{H^2}$$

From [7a] we see that for one frequency alone the amplitude of the fundamental remains unchanged to second order, so that replacing $\tilde{M}$ on the right side of [10] by the ideal Lifshitz-Kosevich magnetization should be a reasonable approximation for calculating the lowest order combination terms. We then obtain

$$[11] \qquad \tilde{M} = A_a \sin [x_a - \kappa_a A_a \sin (x_a) - \kappa_a A_b \sin (x_b)] + A_b \sin [x_b - \kappa_b A_a \sin (x_a) - \kappa_b A_a \sin (x_b)] .$$

Assuming the quantities κA to be small, we keep only the linear terms in such quantities giving

$$[12] \qquad \tilde{M} = -\frac{\kappa_a A_a^2}{2} \sin (2x_a) - \frac{\kappa_b A_b^2}{2} \sin (2x_b) - \frac{A_a A_b}{2} [(\kappa_a + \kappa_b) \sin (x_a + x_b) - (\kappa_a - \kappa_b) \sin (x_a - x_b)]$$

Thus, to lowest order, the amplitudes of the sum and difference frequencies are given by

[13a] $$A_s = \frac{A_a A_b}{2} (\kappa_a + \kappa_b)$$

and

[13b] $$A_d = \frac{A_a A_b}{2} (\kappa_a - \kappa_b)$$

The results obtained so far apply when the absolute amplitude of the dHvA oscillations is much smaller than the field spacing, $\Delta H \simeq \frac{H^2}{F}$ or in the reduced notation, $C_r \ll 1$. There are many cases where this is no longer true. The dHvA magnetization can approach or even exceed the field spacing. In such cases the magnetization formally becomes multivalued, and the resulting magnetization is the one with the greatest thermodynamic stability. When $C_r > 1$ the magnetization is no longer uniform inside the sample, and Condon domains are formed (see Condon 1966, Condon and Walstedt 1968).

The M.I. results discussed in this chapter clearly alter the temperature dependence from that given by the ideal Lifshitz-Kosevich (L.K.) amplitudes [1b]. For example, in the case of combination tones generated by M.I., the temperature dependence of the amplitudes of the sum and difference frequencies from [13a] and [13b] is $\tilde{M}_{s,d}(T) = \frac{X_a X_b}{\sinh X_a \sinh X_b}$.

CHAPTER FOUR

REDUCTION OF MAGNETIC INTERACTION USING A FEEDBACK TECHNIQUE

From the discussions of the previous chapter, it is evident that magnetic interaction must play only a very small role if any information from the harmonic content is to be obtained.

It is clear that the absolute amplitude of the magnetization determines the relative sizes of the M.I. generated harmonics. One might consider reducing these troublesome M.I. effects by exploiting the temperature dependence. At a high enough temperature, the absolute amplitude can be made arbitrarily small, thereby reducing the M.I. harmonics. Unfortunately the L.K. second and higher harmonic amplitudes drop off faster than their M.I. counterparts with increasing temperature thereby increasing, not decreasing the waveform distortion.

The dependence on the demagnetizing factor δ in [4] has been used with some success to minimize or control the effects of M.I. Everett and Grenier (1978) have cut crystals into

ellipsoids of varying aspect ratios to study the dependence of the harmonic structure on three different values of δ. In previous g_c factor measurements, Gold and Schmor (1969) have cut very thin (0.5 mm) disks with $\delta \approx 0.9$ to reduce M.I. Unfortunately, this thin disk method is tedious, and has some undesirable side effects. The method about to be described avoids most of the undesirable features of the "disk method" and offers some advantages as well.

Experimentally, one usually modulates the quasi-static background field H with a small perturbation $h(t)$ produced by a modulation coil so that

$$[15] \qquad B = H + 4\pi\ (1-\delta)\ \tilde{M} + h(t).$$

The fact that the modulation field $h(t)$ enters into the equation for B in the same way as $\tilde{M}$ is the seed for the feedback idea. If we separate $h(t)$ into two components

$$[16] \qquad h(t) = h_m + h_f$$

and we let $h_f = -\beta\tilde{M}$, where β is an experimentally adjustable feedback gain, then the equation for B can be made independent of $\tilde{M}$, i.e., if

$$[17] \qquad \beta\tilde{M} = 4\pi\ (1-\delta)\ \tilde{M}$$

the M.I. will be effectively suppressed. It is therefore necessary to obtain a signal proportional to $\tilde{M}$, adjust the gain accordingly, and apply this signal as a field to the sample.

Suppression of M.I. by means of magnetic feedback was first achieved by Testardi and Condon (1970) in the course of their sound velocity measurements in beryllium. In their work, a coil was wrapped tightly around a cubic sample, and a current in the coil approximated the equivalent surface currents in the sample and thus could be made to cancel the dHvA magnetization. The appropriate current was found by imposing a null detection criterion on an external pickup coil. In the Testardi-Condon arrangement, the sample could not be rotated, and for a cubic sample, the magnetization is inherently non-uniform. We have developed a different type of technique which allows the sample to be rotated, and in which the dHvA effect itself is used to establish the correct amount of feedback. There are several such criteria, and the ones which are easiest in practice will be discussed in turn.

1. Minimization of M.I. Combination Terms

As we have seen, M.I. acts as a mixer in the sense that if two genuine frequencies F_1 and F_2 are present, M.I. generates $nF_1 \pm mF_2$ where n and m are integers. These terms are not present in the ideal theory, of course, and the criterion becomes the minimization (ideally the zeroing) of these combination frequencies.

2. Mass Plots

The temperature dependence of the L.K. harmonics is given by

$$A_r(T) \propto \frac{rX}{\sinh rX} \approx X\, e^{-rX}$$

where $X = \lambda m_c^* T/H$ and $\lambda = 2\pi^2 k_B/e\hbar$.

The M.I. terms have a different temperature dependence for each harmonic, so that optimum feedback is found when plots of ln A/T vs. T/H for the first, second, and third harmonic are straight lines with the slopes precisely in the ratio 1:2:3.

3. The Beat Envelope

When 2 signals are close in frequency, all the harmonics beat. The M.I. terms generally beat at the difference frequency of the first harmonic because it is the strongest in amplitude. The feedback can be adjusted to make the harmonics beat at their proper frequencies.

4. Phase Information

The relative phases of the harmonics of the ideal L.K. terms are easily calculated, and since the M.I. terms add in a different phase, one need simply adjust β until the L.K. phase relationships are established.

5. Linearity of A_1/A_3 vs. $(A_1/A_2)^2$

As discussed in Chapter Two, (see [3a]), a plot of A_1/A_3 vs. $(A_1/A_2)^2$ should yield a straight line if the harmonic amplitudes follow the ideal L.K. form. Curved plots are obtained in the presence of M.I.

As presented, the feedback technique seems to accomplish the same desirable objectives which have previously been attained by exploiting the demagnetizing field.

Perhaps the most tedious feature in the disk-method is the actual preparation of the sample. In each sample, only one direction can be studied, the one perpendicular to the plane of the sample. The demagnetizing field is very sensitive to orientation, so that special care must be taken to ensure that the external field H is precisely perpendicular to the plane of the disk. Disk-shaped samples are fragile, and when using soft materials such as lead, it is difficult to keep the sample free of strain. The sensitivity of the detection apparatus is also dependent on $(1-\delta)$, so that reducing M.I. reduces the sensitivity by the same factor.

The above drawbacks are all related to the requirement that the sample be a thin disk. In the feedback method there is no such constraint, and any ellipsoid can be used. The ellipsoidal shape is necessary only to achieve a uniform induction field, and it is felt that for some applications of the feedback technique, the sample need not even be ellipsoidal (discrimination between genuine dHvA terms and M.I. terms; see below). In the case of a spherical sample all directions in the crystal can be studied in the same experiment, and only one sample need be prepared. The spherical sample is evidently not subject to the precise orientation requirement of the disk, and a sphere is the optimum shape for mechanical stability. Finally, the sphere has a large filling factor for solenoidal pick-up coils, and it can be shaped quite precisely.

There is a distinct advantage to the feedback system when one is faced with the problem of deciding whether or not an observed frequency is genuine, or generated by M.I. Increasing the feedback gain from zero causes the M.I. generated terms to fall in amplitude, while the genuine dHvA frequencies stay the same or rise in amplitude. This can be very helpful in cases where M.I. generates tens of sidebands, many of which may be larger than the genuine frequency (c.f. van Weeren and Anderson, 1973). To acquire the same information unambiguously from the disk method, one would have to make at least two disks with different aspect ratios.

A valuable side effect of using feedback is that the absolute amplitude of the dHvA oscillation can be very easily measured. In the past, careful measurement of sample volume and geometrical coupling constants between the sample and the detection coil were required, as well as the net gain of the amplification system, with all its filters. (c.f. Knecht 1975) Using feedback, the only calibration constant which is required is the Gauss to amp ratio γ of the modulation coil. When optimum feedback is attained, one simply measures the amplitude of the feedback current I_f in the modulation coil, and the dHvA magnetization $\tilde{M}$ is given absolutely by

$$[18] \qquad \tilde{M} = \frac{\gamma I_F}{4\pi(1-\delta)} = \frac{3\gamma I_F}{8\pi} \quad \text{(for a sphere)}$$

where δ is the demagnetizing factor.

The feedback principle could be used with advantage in measurements of the quantum oscillations in other electronic

properties of metals eg. Shubnikov-de Haas effect, ultrasonic attenuation etc. One would still need to measure the dHvA magnetization oscillations in order to obtain the required feedback signal. For example, feedback could be used to determine whether a set of quantum oscillations in, say, the ultrasonic attenuation are genuine ones or generated by M.I.

As we shall see, an integrator is present in the feedback loop, bringing inevitable drifts in the zero level of the feedback signal. When this occurs, there is a D.C. current added to the modulation field which appears as a D.C. shift in the external field H. In our experiment, this drift could easily be kept below 5 Gauss during the course of the measurements, which was insufficient to materially affect the amplitude data. However, these drifts make the phase information less reliable.

A slight imbalance in the pickup coil does not turn out to be a problem since this would simply increase or decrease the modulation range. The coils could easily be balanced to reject the homogeneous modulation field to 1 part in 10^3, so that a modulation range of 1 kG might have been altered by at most ± 1 Gauss.

CHAPTER FIVE

EXPERIMENTAL DETAILS

5.1 Sample Preparation

The experiments were performed on single crystals of lead. Previous use of the Czochralski method for crystal growth (c.f. Phillips and Gold 1969) showed its great success in producing single crystals of extremely low Dingle temperatures. The apparatus centers around a melt of zone refined lead (6NT grade) from Cominco Ltd., electrically heated in a vacuum of 10^{-6} to 10^{-7} Torr. A single crystal seed is dipped into the melt, and the heat conduction through the seed is enough to keep all but the submerged portion solid. In the process of reaching equilibrium, the meniscus turns upward, and the seed is slowly pulled from the melt. Typical growth rates are 0.5-1.0 cm/hr., 0.5 being the slowest possible. The diameter of the resulting single-crystal cylinder was found to be rather insensitive to pulling speed, but critically dependent on melt temperature. Figure 3 shows the dependence of crystal diameter on heater voltage. The crystal diameter is very sensitive to heater voltage, and this dictates the need for a rather high degree of long term stability and

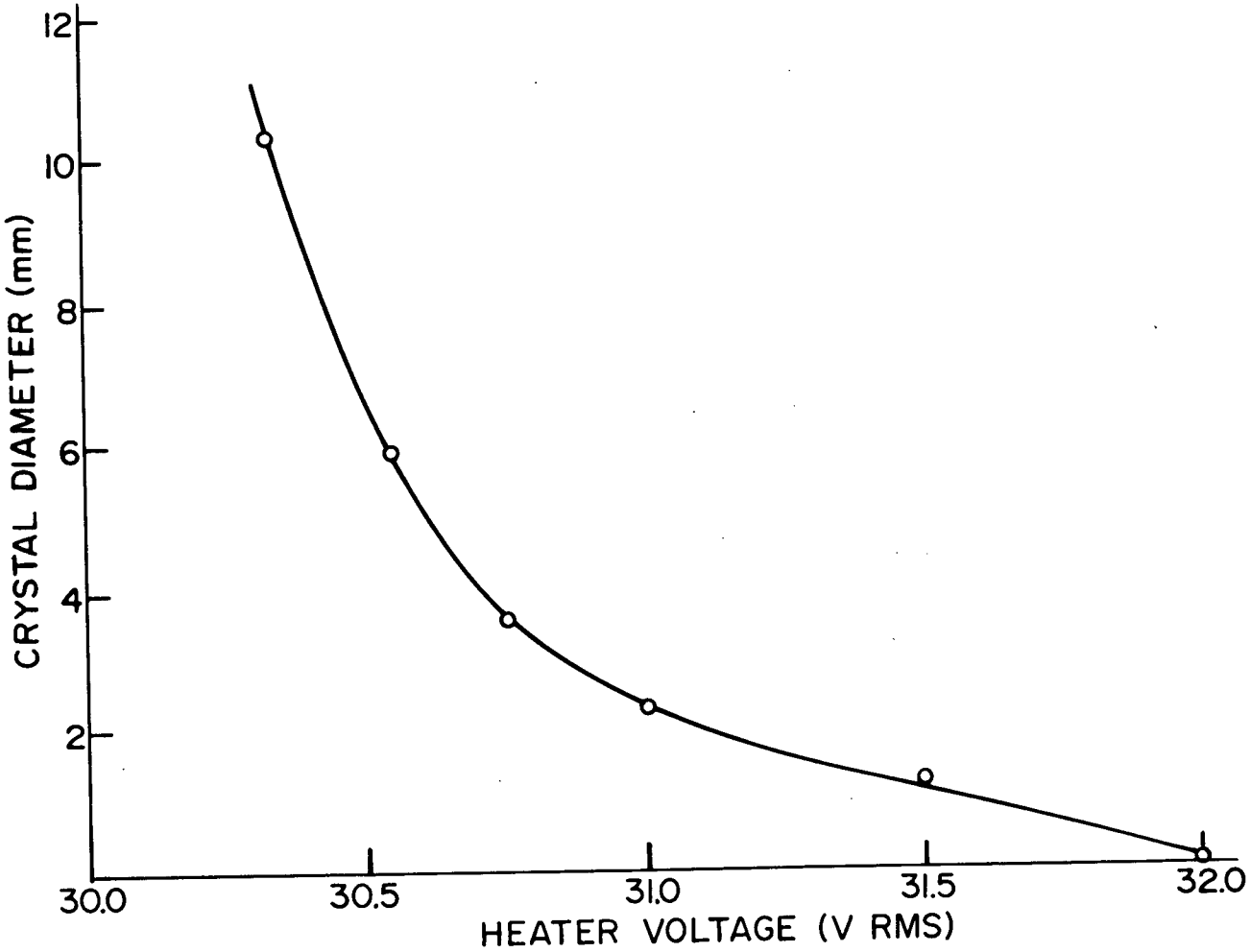

Figure 3. Crystal Diameter as a Function of Melt Heater Voltage

measurement accuracy. The more direct measurement of temperature with the use of a thermocouple had inherent thermal lag and irreproducibility drawbacks, requiring the operator's constant attention during the growth process. In the voltage measurement, one need only set the voltage to obtain a crystal of any predetermined diameter. Four figure accuracy was required in the absolute (A.C.) voltage measurement and a Sola 5008 constant voltage transformer provided the required stability. To adjust the voltage, a variac was used in conjunction with two rheostats. The fine control had a range of ± 1 part in 10^3 of the absolute voltage. Crystals ranging in diameter from 1 to 10 mm were pulled reproducibly using this method. The experiment required a spherical crystal of roughly 7 mm diameter, so that crystals pulled for the feedback experiment had a diameter slightly larger than this.

After pulling a crystal roughly 5 cm long, it was separated from the melt by raising the voltage on the heater. Once the cylinder was removed from the growing apparatus, it was carefully mounted in a rotating chuck. A hollow copper circular cylinder was used as a spark cutting tool. The wall was kept below 0.010 in, and the tool was rotated during the cutting procedure since the tool erodes as well as the sample. As the rotating tool was lowered with its axis perpendicular to the rotating crystal cylinder, a spherical sample resulted if the axes intersected.

The intersection was closer than 0.002 in, as this could be carefully adjusted during the final cutting stages by making sure that the tool was cutting on all of the circle inscribed in the crystal.

When the sphere was near completion, there remained two points or "ears" on which the tool was cutting. One held the sphere to the unused part of the crystal cylinder, the other holds the endpiece to the sphere. It was desirable for the latter to cut through first, so the tool axis was positioned 5^{o} away from being perpendicular to the crystal axis, keeping both axes coplanar. Using this cutting procedure, crystals forming better than 1% spheres were usually obtained.

Since lead is a strong absorber of X-rays, the surface of the crystal must be very good in order to obtain adequate Laue back-reflection photographs. A suitable etching procedure was needed to remove the pitted surface layer generated by the spark erosion process. This procedure consisted of a 45 minute etch in strong etchant (250 cc glacial acetic acid, 187.5 cc distilled H_2O, and 62.5 cc 30% H_2O_2) immediately followed by a wash in ethanol.

After carefully mounting the crystal on a goniometer, 5 minute Polaroid X-ray photographs could be taken for orientation. The X-ray process included rotating to major symmetry directions to ensure both a single crystal, and an unambiguous final orientation.

5.2 Detection Apparatus

In the inductive method for measuring magnetic susceptibility the sample is placed in a balanced pickup coil and also a separate modulation coil. The latter provides a time dependent (often sinusoidal) deviation in the steady background field, and the pickup coil is balanced to be insensitive to this change. Any net magnetization inside the balanced pickup coil induces a voltage in it proportional to $\frac{d\tilde{M}}{dt}$. The balanced pickup coil consists of two coils, one for the detection of the total induction (the pickup coil) and the other to buck out the contribution from the modulation field (the bucking coil).

Since large modulation was envisaged, mechanical rigidity was of primary concern since in this regime vibrations are the major source of noise. To this end, the modulation coil took the form of a long solenoid, mechanically fixed inside the bore of the main magnet providing the steady background field.

The pickup coil and the counter-wound bucking coil, again to achieve maximum mechanical rigidity, were wound as two concentric solenoids directly on top of one another. The centre tap was made available to fine tune the balance when the coils were cooled. It is true that some sensitivity is lost in this arrangement because the flux due to the magnetization of the sample threads both the pickup and the bucking coils. For the worst case of a long rod sample, this loss for our coils is less than a factor of 2, but the gain in signal-to-noise is well worth it.

Some thought was given to the size of the wire which should be used. A simple calculation taking into account the Johnson noise given by the Nyquist equation and the total induced signal S gives the signal to noise ratio S/N as a function of the radius of the wire r.

$$[19] \qquad S/N \approx \frac{d}{dt}\,[4\pi M]\left(\frac{h}{4}\right)(4k_B T\Delta f)^{-1/2}\,\sqrt{\frac{\pi w}{\rho}}\,\left(\frac{1}{r}\right)$$

where M is the magnetization of the sample

h is the height of the coil

w is the width of the coil

T is the temperature

Δf is the frequency bandwidth

and ρ is the resistivity of the wire.

[19] has no maximum as a function of r, so that r should be made as small as possible, with only the mechanical strength of the wire to be considered. The resistivity dependence suggests pure copper wire or superconducting wire.

When this solenoid-on-solenoid arrangement is used, one must carefully calculate the ratio of turns in the pickup to that in the bucking coil, as the combined width of the coils is limited by the available space. One must also be careful to overwind the bucking coil so that in the process of balancing, turns need be removed, not added.

In the final model, the pickup-bucking coil pair had an inside diameter of 0.300" and an outside diameter of 0.500".

The pickup coil had 9500 turns, and the bucking coil had 6016¼ turns of #46 copper wire. (0.0017 inches in diameter, insulation included).

The balancing was done by constructing a modulation coil similar to that in the cryostat, and placing the sample-bucking coil arrangement inside. Turns were removed from the bucking coil until zero pickup resulted. This could be done to an accuracy of ¼ turn (~ 1 in 10^5 at room temperature but worsening to ~ 1 in 10^4 upon cooling to 4.2K). For best noise immunity, the connection to the outermost windings was put at ground potential.

The spherical sample (radius a) and balanced pickup coil form a very convenient detection arrangement. The sphericity of the sample ensures a uniform magnetizing field inside, and concurrently forms a spatially inhomogeneous dipole magnetizing field outside the sphere as shown in Figure 4.

The coil former for the sample coil (a full description is given in Appendix A) formed the housing of an intricate rotation system designed to rotate the sample about an axis 90° away from the only direction of access. Pippard and Sadler (1969) describe a system which uses very little space in the sample region by employing a Mylar gear wheel. Several modifications to this design were made to accommodate our spherical sample, and compactness requirements. The details of the construction are presented in Appendix A.

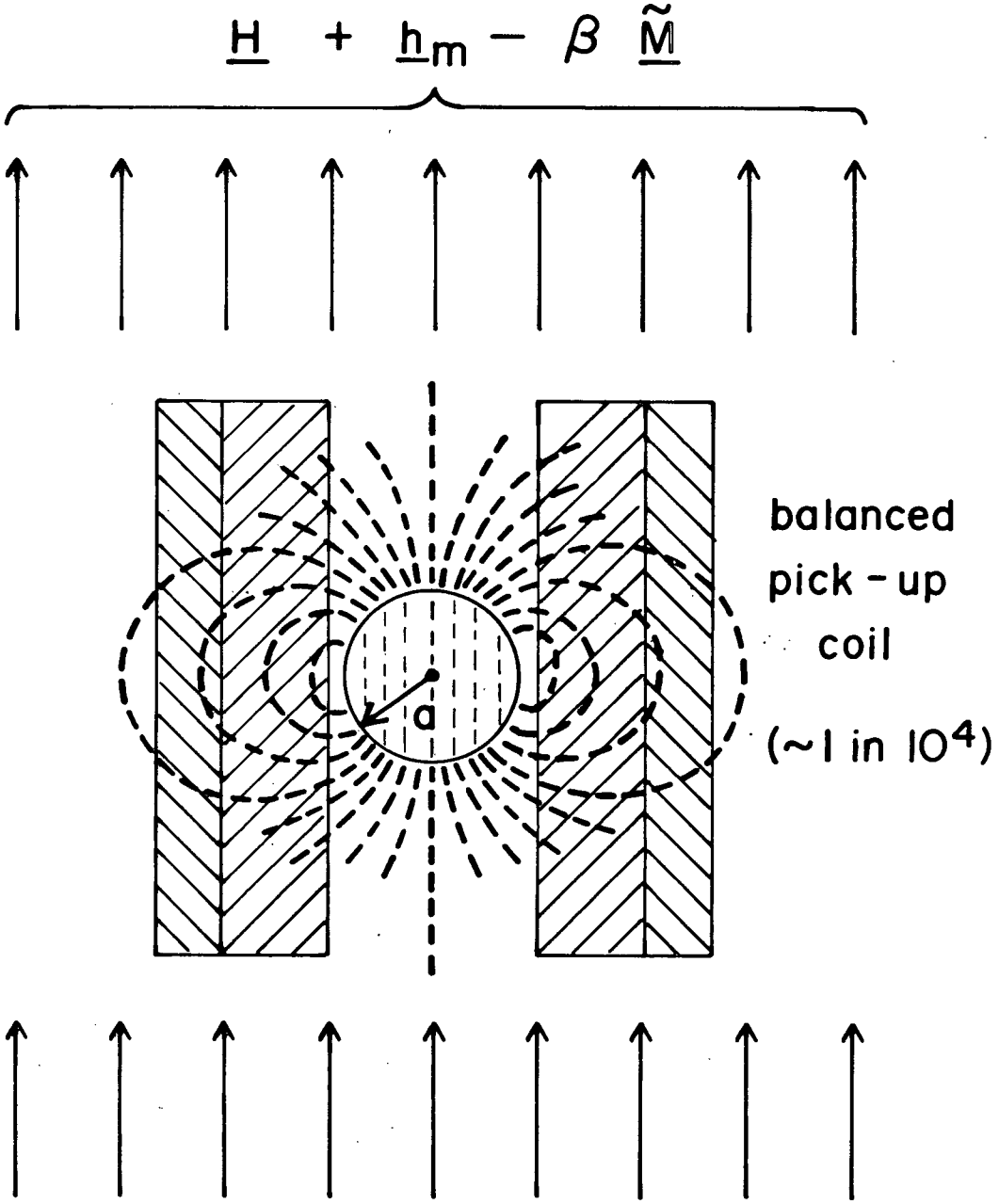

$\underline{B}$ (r < a): add uniform field $\frac{2}{3} 4\pi \underline{\tilde{M}}$

$\underline{B}$ (r > a): add $\underline{\tilde{M}} \frac{4\pi}{3} \left(\frac{a}{r}\right)^3 \left\{2\hat{\underline{r}} \cos\theta + \hat{\underline{\theta}} \sin\theta\right\}$

(dipole field)

Figure 4. Detection Arrangement

Although [19] gives a $1/\rho$ dependence to the signal to noise ratio, we were working in the regime where the total noise was predominantly determined by the input noise of the front end differential amplifier. For frequency response considerations, however, (see section 5.5) a superconducting sample coil was wound. Unfortunately, it turned out that the large modulation employed in our measurement techniques rendered the coil normal in parts of the modulation cycle where $\frac{d^2h}{dt^2}$ was large. The second derivative is important since it, along with the self capacitance of the coil determines the internal induced currents. A calculation performed after the coil was wound and used showed that these induced currents exceeded the critical current for the wire at the fields in which we were working.

5.3 Modulation Coil and Superconducting Magnet

Both the use of the feedback technique, and the detection of long period dHvA oscillations benefit greatly from the use of large modulation. Homogeneous modulation of >1 kG peak to peak amplitude could be achieved with the final apparatus. Wrapped by Richard Christie, the coil took the form of an 0.0602 m long solenoid with an 0.00986 m inner radius. Four layers of 316 turns each were wound using a niobium 48% titanium alloy superconducting wire (0.0065 inches in diameter, insulation included). The finite solenoid equation gives a Gauss-to-amp ratio of γ=251 for this geometry. In order to modulate with amplitudes of $\gtrsim$ 1 kG, several amps are required to power the coil. Since the transmission of this current would be a major heat leak to the helium bath, a simple calculation was done to optimize the diameter of the leads to the modulation coil. Taking the resistive heating and conduction into account, copper and brass wire gave roughly the same heat leak for typical currents (the optimum diameters were, of course, very different). Brass was chosen because of its smaller temperature coefficient of resistance. For typical currents, the heat leak was estimated to be 0.1 Watt for the 1.4 mm optimized diameter brass wire. Superconducting wire was continuously soldered to the brass up to the maximum level of the helium bath.

In addition to screw mounts, grease was used as a low temperature glue to ensure the rigidity of the mount. The

main magnet was built by American Magnetics (A.M.I. #10066) and was rated at 80 kG with a homogeneity of 1 part in 10^5 over a 1 cm diameter sphere at its centre. Vapour cooled current leads were used to minimize the heat loss; the current at peak field was 65 Amperes. The flow rate of helium through these leads could be constantly monitored while running. The Gauss to amp ratio of the main magnet was 1229. The assembly included a persistent current switch, which allowed the magnet to run without an external power supply once it was energized.

5.4 The Cryogenic Apparatus

Housing the main magnet is an Oxford liquid helium dewar with the usual liquid nitrogen jacket. The vacuum spaces contain super insulation for maximum thermal isolation. Inside this outer dewar is an inner dewar with a tail extending into the main magnet core, inside the modulation coil.

Built by Peter Haas in the Physics machine shop at U.B.C., the inner dewar featured an externally controlled vacuum tight valve which when opened allowed a transfer of liquid helium from the outer dewar to this inner dewar. Not only does this make the transfer process more convenient, but the helium transferred to the inner dewar (and sample) could be filtered to remove solid-air particles. The vacuum jacket of the inner dewar allowed the pumping of the helium inside to attain temperatures of about 1.2K. For best noise immunity, the inner dewar was isolated mechanically from the main magnet, and modulation coil. This

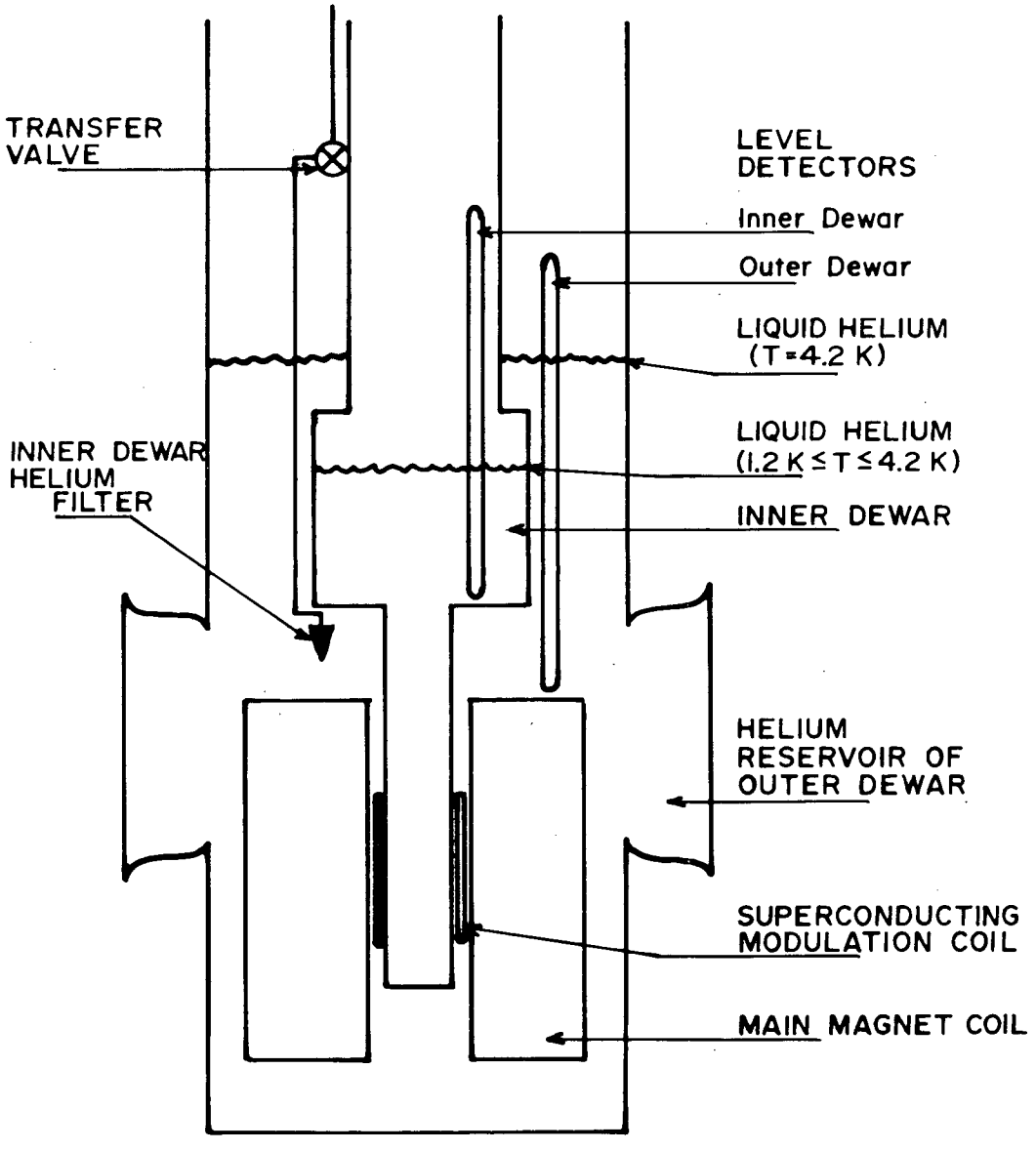

Figure 5. General Schematic Cryogenic Assembly

isolation could be checked externally with a contact resistance test. Both the outer and inner dewars contain liquid helium level detectors manufactured by American Magnetics. Figure 5 shows a composite drawing of the cryogenic apparatus.

5.5 Signal Processing

As previously discussed (Section 5.2), the pickup coil consisted of 2 counter-wound solenoids balanced at room temperature to be insensitive to uniform fields. A lead from the centre tap of these coils was made available at the top of the cryostat to fine tune the balance as the coils were cooled.

The major consideration in the design of the detection circuitry was the elimination of any frequency dependent components in the feedback network. Since the pickup coils, and modulation coils would have considerable inductance, the following procedures were used to eliminate possible phase shifts caused by their reactance. Care was taken in the design of the fine tuning circuit to ensure that the coils were not loaded to the point where phase shifts might be important at the maximum frequency.

The pickup coil's inductance was calculated to be 18 mH as an upper limit, and 500 Hz was chosen as the maximum frequency to be handled by the feedback network.

The balancing arrangement is shown in Figure 6. The equivalent circuit for the balancing circuit is shown in Figure 7.

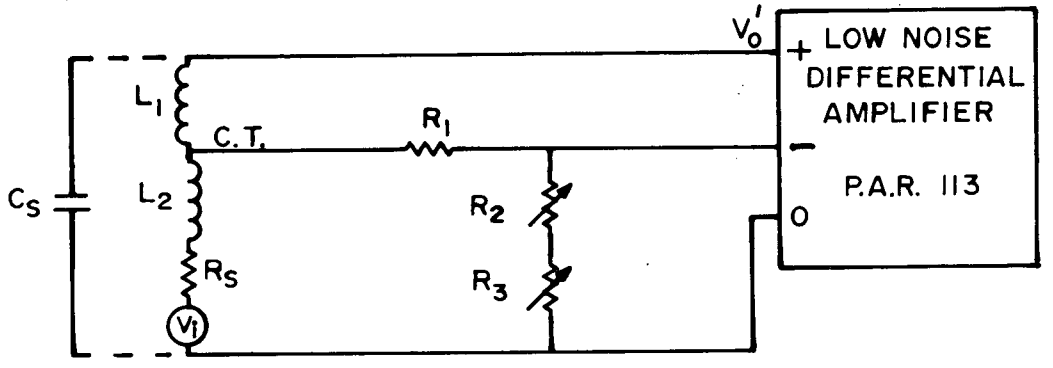

Figure 6. Fine Tuning Circuit

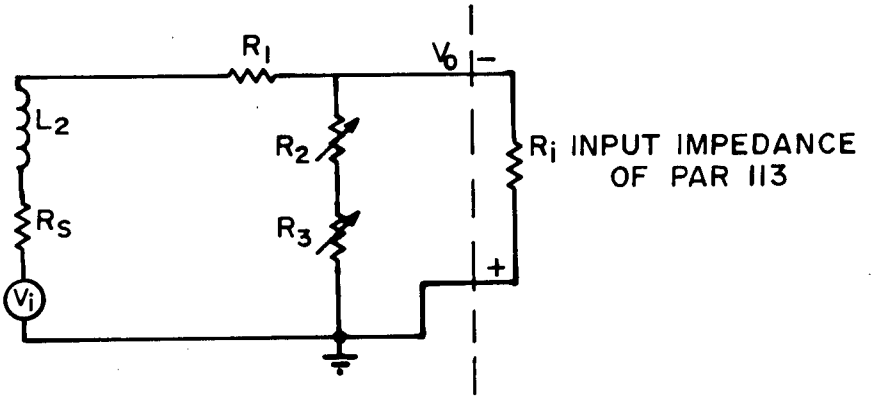

Figure 7. Equivalent Circuit for Tuning Arm

The external load on the centre tap (C.T.) is at most R_1. If R is the parallel combination of $R_2 + R_3$ and R_i,

$$R = \frac{R_i(R_2 + R_3)}{R_i + R_2 + R_3}$$

Then $$V_o = \frac{V_i R}{R_S + j\omega L_2 + R_1 + R}$$

[21] $$\frac{V_i R\,(R_S + R_1 + R - j\omega L_2)}{(R_S + R_1 + R)^2 + (\omega L_2)^2}$$

The phase shift is

[22] $$\phi = \tan^{-1}\left[\frac{-\omega L_2}{R_S + R_1 + R}\right]$$

The D.C. resistance of the counterwound coil was $R_S = 42\Omega$ at 4.2K hence, for a phase shift of $<1°$ at 500 Hz,

$$R_1 + R > 450\ \Omega$$

As it turns out, the self capacitance of the coil was the determining factor. The self capacitance of a coil can to a good approximation, be represented by a parallel capacitor shown as C_S in Figure 6.

The fact that this capacitance was the dominating influence on the frequency characteristics was ascertained by unbalancing the fine tuning slightly, and observing the frequency response

of the pickup coils to the modulation field. When performing this measurement, with $R_1 >> 450\ \Omega$, the frequency response of the pickup coil rolled off to -3db at 90 Hz.

When the self capacitance is taken into account, the voltage V_o' in Figure 6 is given by

[23] $$V_o' = -\frac{j}{\omega C_s}\left(\frac{1}{j(\omega L - \frac{1}{\omega C}) + R_s}\right) V_i$$

where $L = L_1 + L_2$. Hence

[24] $$\frac{V_o'}{V_i} = \frac{1-\omega^2 LC - jR\omega C}{(1-\omega^2 LC)^2 + (\omega RC)^2}$$

If we assume L is negligibly small,

$$\left|\frac{V_o'}{V_i}\right|^2 = \frac{1}{1+(\omega R_s C_s)^2}$$

From the frequency characteristics, C_s was determined to be 25.8 μF. Using the full equation [24] with L = 18 mH did not change the rolloff frequency, proving our assumption that L is negligible. The frequency characteristic of the coil is the limiting factor in the feedback loop, and in fact sets the upper bound to the usable feedback band.

The modulation coil was energized with a Crown M600 D.C. amplifier. The coil was placed in a series combination with a 5 Ω non-inductive monitor resistor. The inductance of the coil

produced a large phase shift even for frequencies as low as 50 Hz. This situation is easily remedied by using current feedback. A tap was taken between the 5 Ω resistor, and the modulation coil (see Figure 9), and used to provide a feedback voltage for the operational amplifier feeding the Crown amplifier. The Crown amplifier gain is then immaterial so long as it is large enough and the current gain of the op-amp-Crown configuration is determined by only 2 resistors. Using this idea, the phase shifts were eliminated up to 1 kHz, above which the gains needed would set the system into oscillations.

There is a safety precaution which must be emphasized at this point. Since the Crown amplifier can deliver enough current to damage the apparatus, its gain, while still being sufficient to assure linearity, must be kept below the point where accidental disconnection of the feedback resistor results in catastrophe. The Crown gain setting can be used as a limit, without harming the overall open-loop gain, since the op-amp provides most of the gain and merely saturates if the Crown cannot deliver the current needed (see Figure 9). The Crown gain was set to deliver the maximum allowable output current for a 15V input signal.

The voltage appearing on the well-balanced pickup coils is proportional to $\frac{d\tilde{M}}{dt}$. $\tilde{M}$ can be retrieved easily by analogue integration. The signal proportional to $\tilde{M}$ was then added to the modulation signal and fed to the modulation coil as a current. A block diagram of the apparatus appears in Figure 8. The circuit diagram appears in Figure 9.

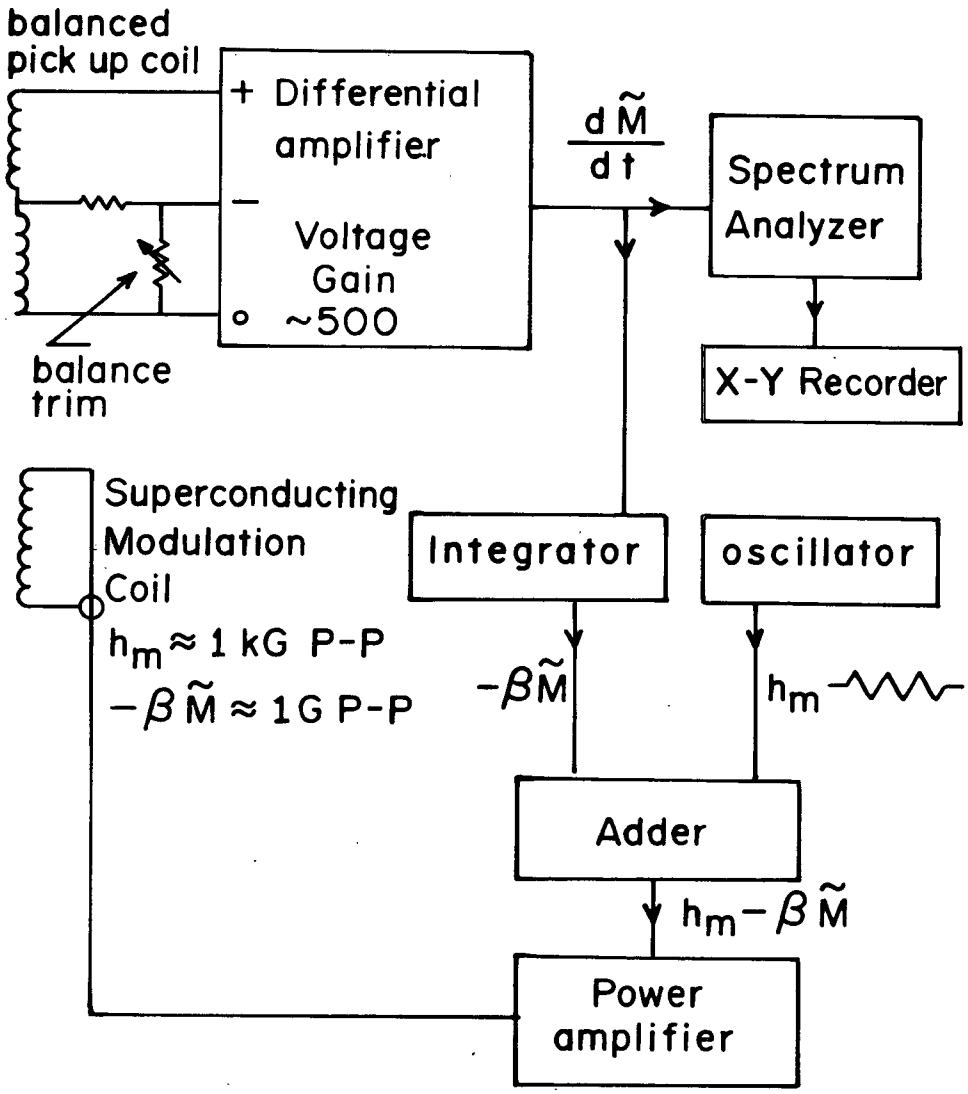

Figure 8. Block Diagram of Apparatus

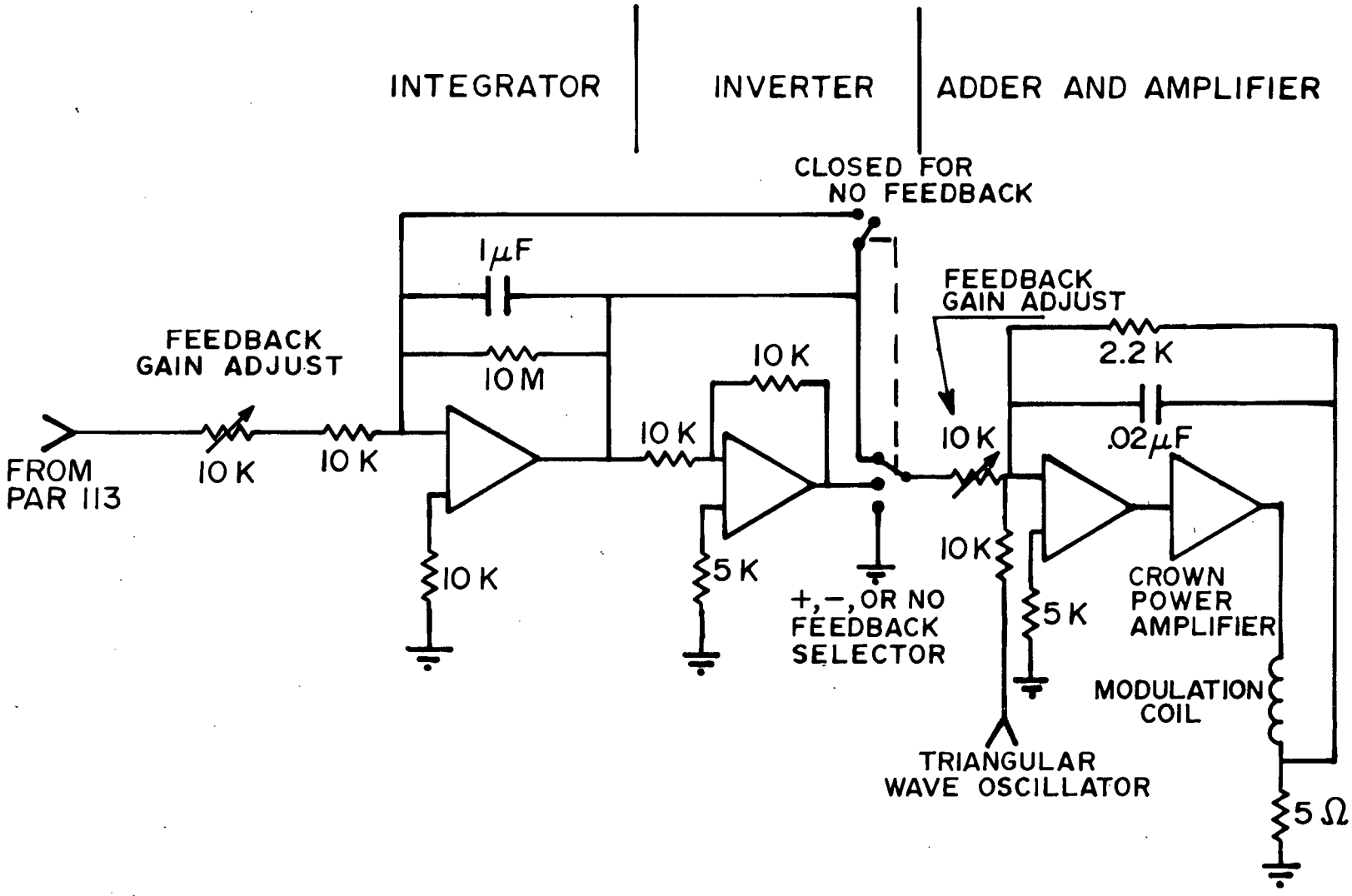

Figure 9. Circuit Diagram of Integrator and Adder

A simple arrangement was used for testing the frequency response of the entire circuitry. The procedure involved unbalancing the pickup coil slightly, and observing the signal after integration on one channel of a dual-trace oscilloscope. The feedback path was broken at the adder, so that only the modulation signal was fed to the modulation coil. The modulation signal from the oscillator was monitored on the second trace of the 'scope. The two traces were carefully superimposed at some low frequency, and then the frequency of the modulation was increased until a separation between the 2 traces became noticeable. The usable feedback band determined in this way was 0.2 to 79 Hz. It must be pointed out that this limited bandwidth is not very restrictive. The low frequency limit was imposed by a 10 sec time constant on the integrator which could be increased in the future. In the procedure used here, the lowest frequency is that of the field modulation and dHvA terms can always be made to appear at higher time frequencies.

Initially the lead sphere was oriented close to the [110] direction. So oriented, lead exhibits a pair of strong γ oscillations with $F_\gamma \sim 17.9$, and a single α oscillation with $F_\alpha \sim 160$ MG. We were most fortunate to obtain the use of a digital spectrum analyzer (Hp3582A) which is essentially an on-line Fourier transformer. When appropriately set up, this computer could resolve the harmonics of the γ doublet, as well as the sidebands appearing at $F_\alpha \pm nF_\gamma$ due to M.I. This "appropriate" setup will now be described.

A triangular wave was used to provide a ramp in the modulation field, and its amplitude was chosen to sweep through enough dHvA oscillations for the resolution of the analyzer to exceed F_γ = 18 MG. When a Hanning window is used, (see Appendix B) 4 oscillations of the fundamental were enough to easily resolve all the harmonics. In practice it was not difficult to sweep through about 5 fundamental γ oscillations at 60 kG; this number of cycles could be increased by working at lower fields because of the H^2 dependence of the field spacing $\Delta H \approx \frac{H^2}{F}$.

At 60 kG, the field at which most of the work was done, $\Delta H_\gamma \simeq 200$ G, and a peak to peak ramp of 1 kG sweeps through 5 γ oscillations.

The spectrum analyzer obtained its input directly from the front-end differential amplifier (see Figure 8).

The modulation frequency was chosen to be 1 Hz, hence the time window on the analyzer should be a little less than 0.5 sec, triggered at the beginning of the rising ramp of the triangular modulation. Figure 10 shows the synchronization of the trigger and the time window.

If a limited number of cycles is considered, the oscillations are essentially periodic in H, and a linear field ramp will transform the dHvA oscillations to the time domain where their time frequency is given by

$$[25] \qquad f = \frac{h\, F\, f_{mod}}{H^2 D}$$

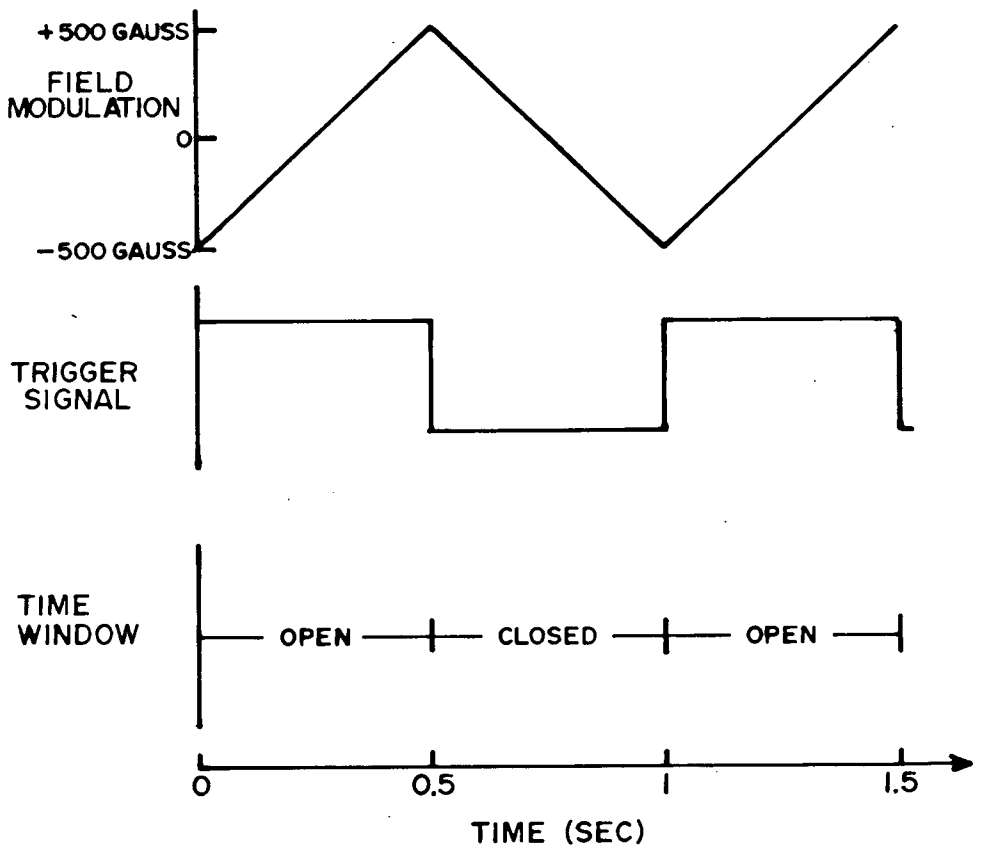

Figure 10. Synchronization of the Time Window

where

H is the steady background field

h is the P-P modulation ramp amplitude

f_{mod} is the modulation frequency

F is the dHvA frequency

and D is the duty cycle of the modulation waveform.

For a triangular wave, the duty cycle is 1/2 so that

$$f = \frac{2h\ F\ f_{mod}}{H^2}$$

For f_{mod} = 1 Hz, H = 60 kG, h = 1 kG, the γ oscillations appear at a frequency of $\sim$ 10 Hz, the α's at $\sim$ 89 Hz.

CHAPTER SIX

EXPERIMENTAL TEST OF THE FEEDBACK TECHNIQUE

6.1 Preliminary Considerations

Initial experiments were performed on a single crystal lead sphere oriented with the total applied field along [110]. In this direction, lead exhibits strong γ oscillations consisting of two frequencies separated by 0.42 MG at $F_\gamma \approx 18$ MG. These 2 frequencies γ^a, γ^b have approximately equal amplitudes of $A_\gamma^a \approx A_\gamma^b \approx 1$ Gauss at 1.2K in a field of 60 kG. There are also somewhat weaker α oscillations at a frequency of 160 MG, and under the above conditions, $A_\alpha \approx 0.03$ Gauss. These oscillations are shown in Figure 11 ($H \sim 60$ kG, $T \sim 1.2$ k)

It turned out that the expansion parameter κA_γ was about 0.4 in the conditions under which we usually worked, so we expected the harmonic distortion to be quite high.

In this chapter, we interpret the dependence of several observable quantities on feedback gain. The technique appears to agree well with the expected results for no M.I. at the optimum feedback gain using the criteria presented in Chapter IV. Much of what follows, therefore is the analysis of the quantities under non-optimal feedback conditions, to ensure an understanding

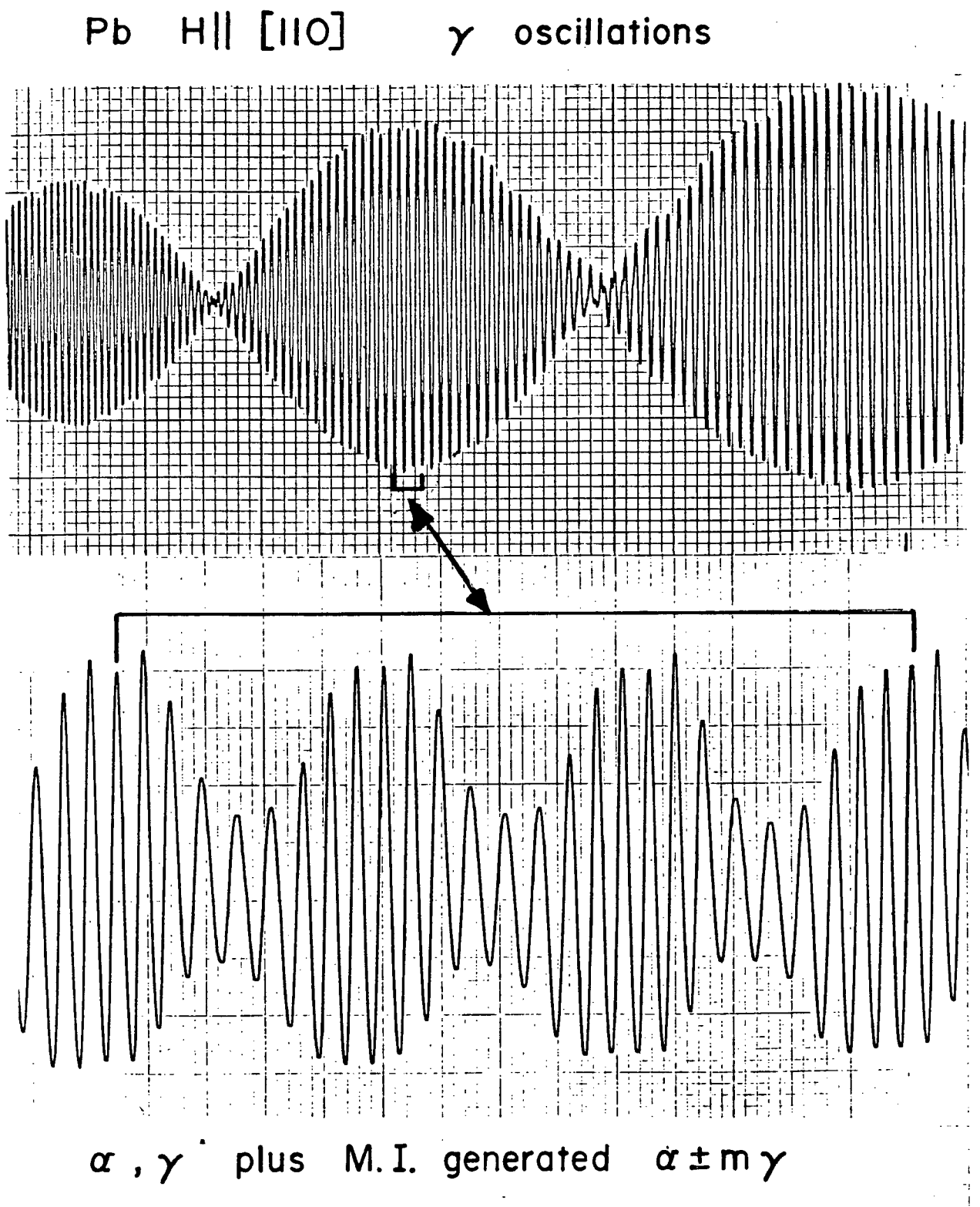

Figure 11. de Haas-van Alphen Oscillations in Pb:H|| [110]
Above: γ oscillations, below: ∿4γ oscillations which were experimentally suppressed to bring out the α oscillations and M.I. sidebands

of the mechanisms involved, and at the same time, it clearly shows the very tedious mathematics one avoids by using the feedback technique. While it is important to check this once, one must remember that at the optimum feedback position, the correction factors in any of the results are no longer needed. For each quantity discussed, we shall, in turn, look at the cases of no feedback, non-optimum feedback and optimum feedback. In some cases, a variety of feedback settings were used.

6.2 Minimization of Sidebands

In order to obtain an idea where the optimum feedback setting was, the minimization-of-sidebands criterion was used first. It is the simplest and perhaps also the most dramatic. Using the triangular modulation, about 5 fundamental γ oscillations were swept out, and analyzed by the spectrum analyzer. About seven sidebands at $F_\alpha \pm nF_\gamma$ were easily resolved. Using the minimization of sidebands criterion, the object was to adjust the feedback gain until these sidebands reached a minimum. Changing the gain from zero in either direction produced the expected results, the sidebands decreased for negative feedback, and increased for positive feedback. Examples of the Fourier amplitude spectrum for several feedback settings appear in Figure 12. Figure 13 is a quantitative presentation of the dependence of the α, $\alpha+\gamma$, and $\alpha-\gamma$ amplitudes on the feedback gain.

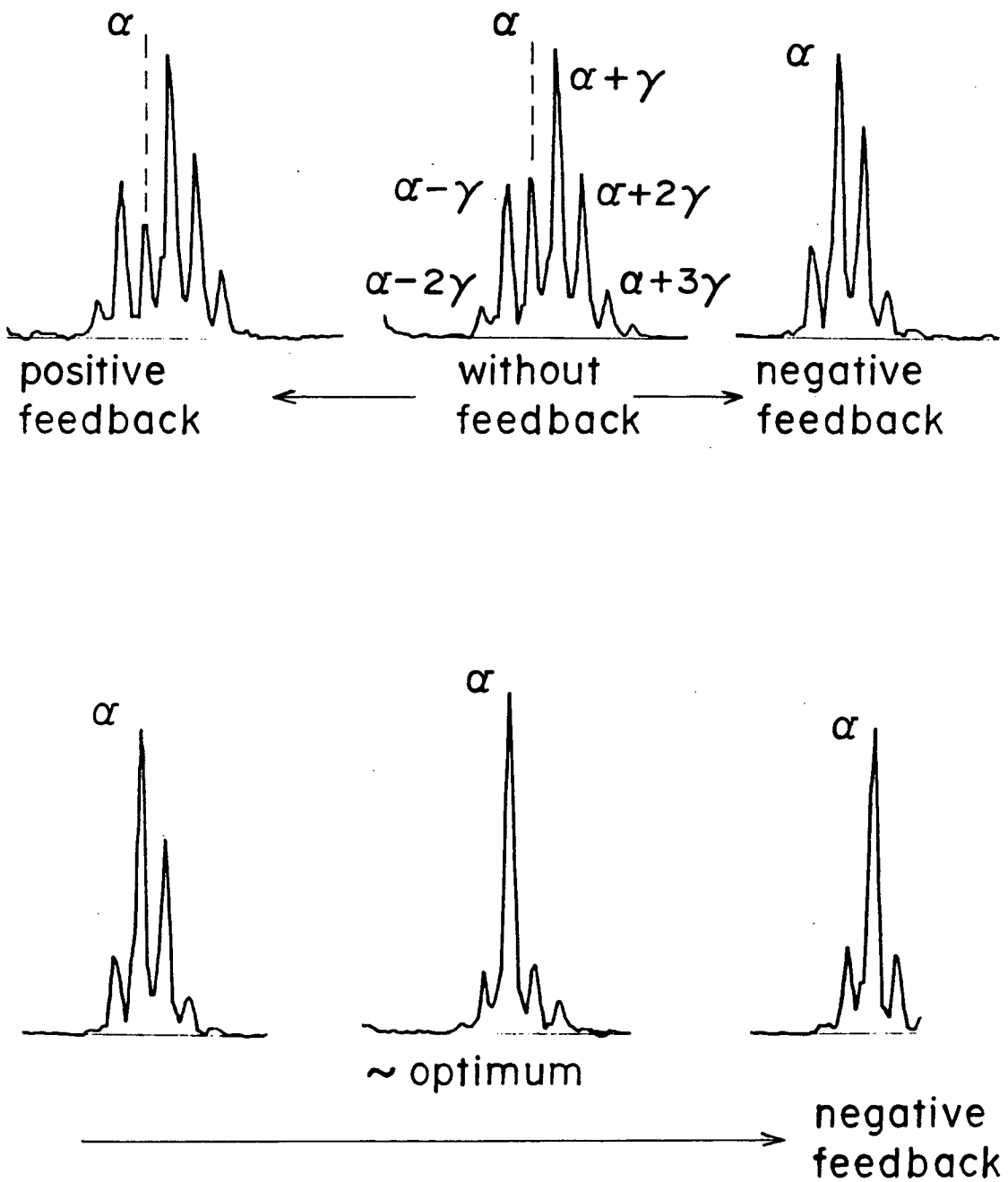

Figure 12. Fourier Transforms Around 160 MG
As A Function Of Feedback Gain.
(The transforms do not start at F=0)
H = 61.79 kG T = 1.2K

$$A_{\alpha}^{(M.I.)} = A_{\alpha}\, J_0 (f_{\alpha} \varepsilon A_{\gamma})$$

$$A_{\alpha \pm \gamma}^{(M.I.)} = A_{\alpha}\, J_1 (f_{\alpha} \varepsilon A_{\gamma}) \pm A_{\gamma} J_1 (f_{\gamma} \varepsilon A_{\alpha})$$

$$\varepsilon = 1 - \frac{\beta}{4\pi(1-\delta)}$$

$$f = 2\pi \frac{F}{H^2}$$

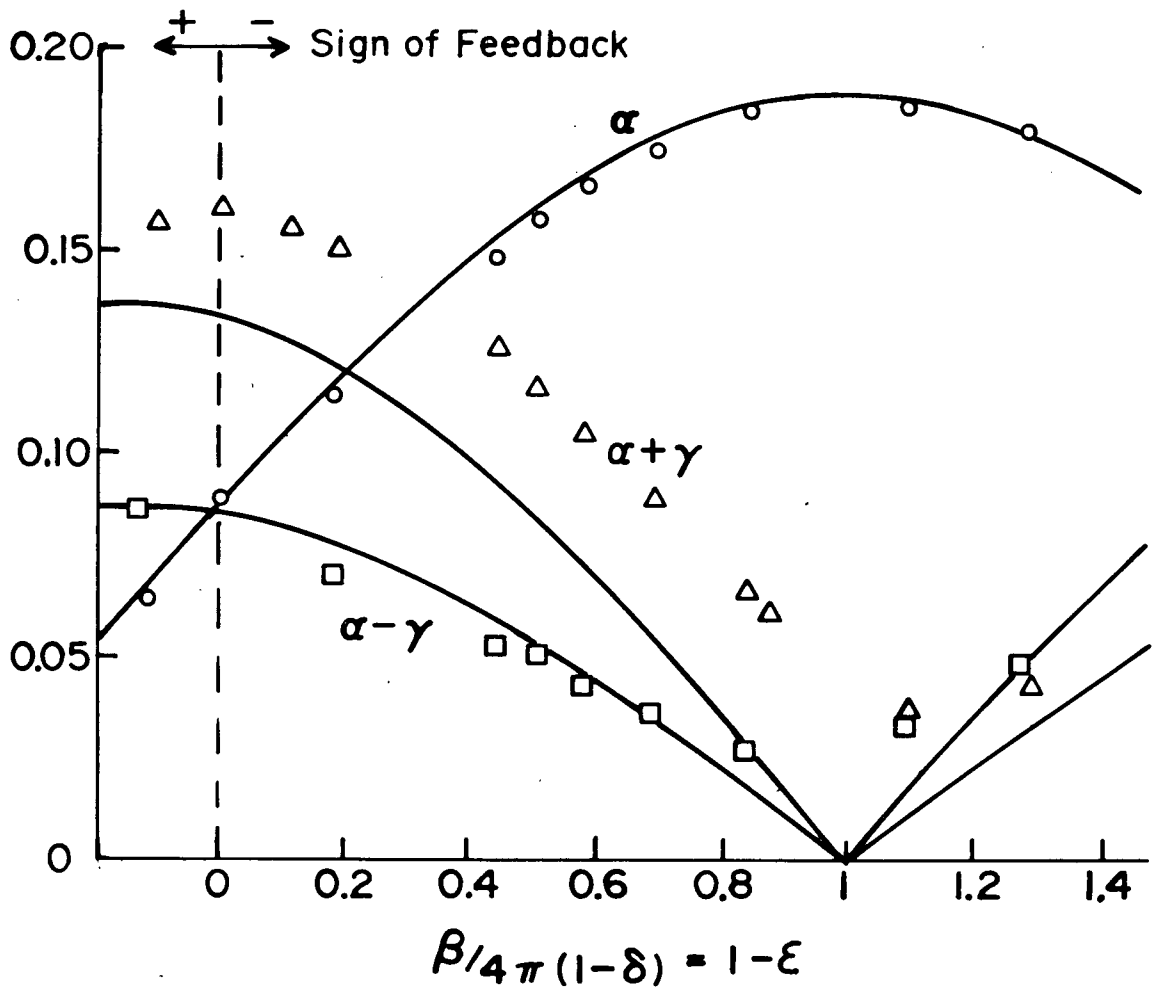

Figure 13. Fourier Amplitudes As A Function Of Feedback Gain

To compare the observed amplitude with theory, let us use the convenient notation:

$$f_{\gamma,\alpha} = \frac{2\pi F_{\gamma,\alpha}}{H^2} \qquad A^*_{\gamma,\alpha} = 4\pi(1-\delta)\left|\tilde{M}_{\gamma,\alpha}\right|$$

$$\varepsilon = 1 - \frac{\beta}{4\pi(1-\delta)} \qquad M_{\gamma,\alpha} = 4\pi(1-\delta)\tilde{M}_{\gamma,\alpha}$$

We expect the strongest M.I. contribution from the effect of the γ term on α. The fundamental dHvA magnetization for α is given by

$$[26] \qquad M_\alpha = A^*_\alpha \sin\left[2\pi\left(\frac{F_\alpha}{B+h} + 1/2\right) - \pi/4\right]$$

where h is a small change in H.

The phase factors need not concern us for the present, and we can expand the denominator for $\frac{F_\alpha h}{H^2} << 1$ to obtain a first order approximation

$$M^{(1)} = A^*_\alpha \cos\left[f_\alpha(h+\varepsilon A^*_\gamma \cos f_\gamma h)\right]$$

assuming that the dominant contribution to the total magnetization in B is $A^*_\gamma \cos f_\gamma h$. This can immediately be decomposed into harmonics

$$[27] \qquad M^{(1)} = A^*_\alpha J_0(f_\alpha \varepsilon A^*_\gamma) \cos f_\alpha h$$

$$- A^*_\alpha J_1(f_\alpha \varepsilon A^*_\gamma)[\sin(f_\alpha + f_\gamma) h + \sin(f_\alpha - f_\gamma)h]$$

$$- A^*_\alpha J_2(f_\alpha \varepsilon A^*_\gamma)[\sin(f_\alpha + 2f_\gamma) h + \cos(f_\alpha - 2f_\gamma)h]$$

$$+ A^*_\alpha J_3(f_\alpha \varepsilon A^*_\gamma)[\sin(f_\alpha + 3f_\gamma) h + \sin(f_\alpha - 3f_\gamma)h]$$

where $J_\nu(x)$ is the Bessel function of the first kind of order ν and argument x.

This first step generates sidebands around f_α, and the next step in the calculation is to allow these sidebands and f_α itself to interact with the γ oscillations. The equations are identical to those in the first step with the subscripts referring to the corresponding reversed roles. One only needs careful bookkeeping. This step is carried out only to the J_1 contributions. For example, when f_α interacts with γ, we get terms in $f_{\alpha+\gamma}$ and $f_{\alpha-\gamma}$. The result is as follows:

$$
\begin{aligned}
[28]\qquad M^{(2)} = {} & A_\gamma^* J_1(f_\gamma\ \varepsilon A^*_{\alpha+\gamma})\cos[f_\gamma-(f_\alpha+f_\gamma)] \\
& + A_\gamma^* J_1(f_\gamma\ \varepsilon A^*_{\alpha-\gamma})[-\cos\{f_\gamma+(f_\alpha-f_\gamma)\}] \qquad \text{terms at frequency } f_\alpha \\
& - A_\gamma^* J_1(f_\gamma\ \varepsilon A^*_{\alpha})\ \sin\ (f_\gamma+f_\alpha) \\
& + A_\gamma^* J_1(f_\gamma\ \varepsilon A^*_{\alpha+2\gamma})\ \sin\ (f_\gamma-f_{\alpha+2\gamma}) \qquad \text{terms at frequency } f_{\alpha+\gamma} \\
& - A_\gamma^* J_1(f_\gamma\ \varepsilon A^*_{\alpha})\ \sin\ (f_\gamma-f_\alpha) \\
& + A_\gamma^* J_1(f_\gamma\ \varepsilon A^*_{\alpha-2\gamma})\ \sin\ (f_\gamma+f_{\alpha-2\gamma}) \qquad \text{terms at frequency } f_{\alpha-\gamma} \\
& + A_\gamma^* J_1(f_\gamma\ \varepsilon A^*_{\alpha+\gamma})[-\cos(f_\gamma+f_{\alpha+\gamma})] \\
& + A_\gamma^* J_1(f_\gamma\ \varepsilon A^*_{\alpha+3\gamma})[-\cos(f_\gamma-f_{\alpha+3\gamma})] \qquad \text{terms at frequency } f_{\alpha+2\gamma} \\
& + A_\gamma^* J_1(f_\gamma\ \varepsilon A^*_{\alpha-\gamma})\cos(f_\gamma-f_{\alpha-\gamma}) \\
& + A_\gamma^* J_1(f_\gamma\ \varepsilon A^*_{\alpha-3\gamma})\cos(f_\gamma+f_{\alpha-3\gamma}) \qquad \text{terms at frequency } f_{\alpha-2\gamma}
\end{aligned}
$$

In this second step $M^{(2)}$, the amplitudes A are to be taken from those generated in the first step $M^{(1)}$.

This expansion should be a reasonable approximation to the gain dependence in our plots of the sideband amplitude (Figure 13). The expansion reduces to the simpler form given earlier ([13a],[13b]) if we consider only the first 2 combination frequencies, and allow only γ to interact with α. We then obtain

$$A^*_{\alpha+\gamma} = A^*_\alpha J_1(f_\alpha \varepsilon A_\gamma) + A^*_\gamma J_1(f_\gamma \varepsilon A_\alpha)$$

and using the small argument approximation

$J_1(x) \simeq \frac{x}{2}$, $x << 1$, this reduces to

$$A^*_{\alpha+\gamma} \simeq \frac{\varepsilon A^*_\alpha A^*_\gamma}{2} (f_\alpha + f_\gamma)$$

Similarly,

$$A^*_{\alpha-\gamma} \simeq \frac{\varepsilon A^*_\alpha A^*_\gamma}{2} (f_\alpha - f_\gamma)$$

A^*_α remains unchanged in this approximation. This is the simplified result obtained earlier with $\varepsilon=1$ for no feedback (see [13a],[13b]). We immediately see that the simple approximation is insufficient to describe the large effect M.I. has on our data, since A^*_α does indeed change, and the sidebands do not rise linearly as this predicts.

In order to use the more detailed formulae [28], we must find the absolute magnetization of at least one of the fundamental terms. This can be done in a few ways. The most satisfying way is to measure A^*_γ by observing the feedback field at the optimum β. The relative magnitudes of A^*_γ and A^*_α can be read directly off the Fourier transform. An alternate method is to fit the gain dependence of the α oscillations to $J_o(f_\alpha \varepsilon A^*_\gamma)$. When there is no feedback, $\varepsilon = 1$, and the magnetization at this point is $M_{\alpha,\varepsilon=1} = A^*_\alpha J_o(f_\alpha A^*_\gamma)$.

At optimum feedback, $\varepsilon = 0$, and $M_{\alpha,\varepsilon=0} = A^*_\alpha$, hence

$$\frac{M_{\varepsilon=1}}{M_{\varepsilon=0}} = J_o(f_\alpha A^*_\gamma)$$

which yields A^*_γ.

Using the feedback technique and [18], A^*_γ was measure to be 6.2 Gauss in a field of 61.82 kG. (Keep in mind that $4\pi(1-\delta)$ is included in this notation). An independent fit to the J_o curve yielded 6.0 Gauss. This is good agreement especially since in these early stages, the feedback was not set particularly carefully. The amplitude of the α oscillations was then obtained by their relative strength in the Fourier transform. This gave $A^*_\alpha \approx 0.189$ Gauss.

Using the derived formulae for A^*_α, $A^*_{\alpha+\gamma}$, and $A^*_{\alpha-\gamma}$, we obtain the feedback dependence:

[28] $$A^*_\alpha(\varepsilon) = A^*_\alpha(0)\ J_o(f_\alpha \varepsilon A^*_\gamma)$$

[29] $$A^*_{\alpha\pm\gamma}(\varepsilon) = A^*_\alpha(0)\ J_1(f_\alpha \varepsilon A^*_\gamma) \pm A^*_\gamma J_1(f_\gamma \varepsilon A^*_\alpha) \pm A^*_\gamma J_1(f_\alpha \varepsilon A^*_{\alpha+2\gamma}(\varepsilon))$$

$$= A^*_\alpha(0)\ J_1(f_\alpha \varepsilon A^*_\gamma) \pm A^*_\gamma J_1[f_\gamma A^*_\alpha J_0(f_\alpha \varepsilon A^*_\gamma)]$$

$$\pm A^*_\gamma J_1[f_\gamma A^*_\alpha J_2(f_\alpha \varepsilon A^*_\gamma)]\ .$$

The results of this calculation are shown as solid curves along with the measured data in Figure 13. It should be mentioned that there are no adjustable parameters in the sense that all the quantities

needed for the calculations were measured by independent means. The agreement is exceptionally good for A^*_α, and the general trends for the sidebands seem correct.

An independent check on the $A^*_\alpha(\varepsilon)$ dependence is conveniently afforded by Aoki and Ogawa (1978) who used rod shaped samples. In their data the α oscillations have a very small amplitude, and only the sidebands appear in the transform. We expect $A^*_\alpha \propto J_o(f_\alpha A^*_\gamma)$. We measure $A^*_\gamma = 6.0$ Gauss, for a sphere, (δ=1/3), so that for a rod (δ=0), A^*_γ will have increased by the ratio $\frac{1}{(1-1/3)} = 3/2$. The argument of the Bessel function becomes

$$f_\alpha A^*_\gamma = \frac{2\pi(160\ \text{MG})}{(61.82\ \text{kG})^2}\ (3/2)\ (6.0) \approx 2.36.$$

This is very close to the first zero of J_o, which is 2.405. Extrapolating our data, which was possible at a later date from an amplitude vs. field measurement, (see Figure 27) we can obtain a more realistic estimate at the field used by Aoki and Ogawa. At their field, 50.5 kG, we measure $A^*_\gamma = 4.10$. For their field,

$$f_\alpha A^*_\gamma = \frac{2\pi(160\ \text{MG})}{(50.5)^2}\ (3/2)\ (4.10) = 2.42$$

which again is in good agreement with their observation of small fundamental α amplitude.

We notice from Figures 12 and 13 that the sidebands never completely disappear. There are many reasons why this might occur, the most obvious being a frequency dependence of the feedback network. There is a clue to the origin of this imperfection in the

amplitudes of the sidebands $f_{\alpha+\gamma}$ and $f_{\alpha-\gamma}$ relative to each other. The data show a change in their relative amplitude, so the mechanism must explain this change.

The frequency response of the feedback network might be such a mechanism if the time frequency of the γ term is correctly fed back, but that of the higher α term is not; however, this is not the case, as was shown by a simple experiment. Decreasing the modulation frequency by a factor of 10 decreases all the feedback components by the same amount. There is no doubt that the system's response is very flat below 10 Hz, yet even when α was made to appear at only 7 Hz, the sidebands at optimum feedback still appeared with the same amplitude.

It was thought that a spatially inhomogeneous feedback field might also cause the residual sidebands. While the feedback field itself is only of the order of 1 Gauss, the superimposed triangular modulation was about 500 Gauss at its peak value. This inhomogeneity would not however, cause the relative sideband amplitudes to change. Even if the field is spatially inhomogeneous, there would be no dependence of the feedback field on orbit i.e. F_γ and F_α would both be fed back the same. This inhomogeneity may impose a limit on the minimum amplitude of the sidebands, but would not change their relative amplitudes. Eddy currents induced in the sample would cause a similar inhomogeneity. The magneto-resistance of lead gives it a skin depth of about 1 meter for our typical fields and frequencies. The skin depth, then should not be a problem, but if eddy current inhomogeneities

were present, they would not account for the non-vanishing sidebands.

The most likely explanation is phase smearing in the sample. This sample had been thermally cycled between room temperature and 4.2K three times before these data were taken. If dislocations and strain had built up, the change in electron density would change the frequency of the orbits in the immediate area, making the optimum feedback a function of the oscillations under consideration.

6.3 The Mass Plots

The temperature dependence of one dHvA harmonic amplitude is given by (see [1b])

$$A_r(T) \propto \frac{X}{\sinh rX} \quad X = 2\pi^2 \, m_c^* \, k_B \, T/(e \hbar B).$$

In the high temperature limit ($X \gtrsim 3$), the hyperbolic sine function can be replaced with its exponential approximation: $\sinh X \approx \frac{1}{2} e^{X}$. Then, letting

$$\lambda = 2\pi^2 m k_B/(e\hbar) = 146.9 \frac{kG}{K}, \text{ we have}$$

$$[31] \qquad A_r(T) \propto T e^{-r\lambda\mu T/H} \qquad \mu = \frac{m_c^*}{m}$$

hence, a plot of $\ln \frac{A}{T}$ vs. T/H should yield a straight line of slope $-r\lambda\mu$. This approximation usually holds, but in the case of the fundamental γ oscillations at [110], the value of X at 1°K and a field of 60 kG is about 1.4, and the error in the exponential approximation becomes about 6%. A simple correction term can be used, and it follows from an iterative scheme to determine μ from data which are not satisfactorily far into the high thermal smearing limit ($X \gtrsim 3$). To develop this scheme, we start with the basic hyperbolic form

$$CTA_r = \frac{rX}{\sinh rX} = \frac{2rXe^{-rX}}{1-e^{-2rX}}$$

where C is a temperature independent constant. Then at constant field we have

$$\ln \left(\frac{A_r}{T}\right) + \ln \left(1-e^{-2rX}\right) + \text{constant} = -rX$$

or

$$\ln \left\{ A_r \frac{\left(1-e^{-2r\lambda\mu\, T/H}\right)}{T} \right\} = -\, r\lambda\mu\, T/H \,.$$

If n is the order of iteration, the value $\mu^{(n)}$ is obtained from

$$[32] \qquad \ell n \left\{ \frac{A}{T} \left(1 - e^{-2r\lambda\mu^{(n-1)}T/H} \right) \right\} = -r\lambda\mu^{(n)}T/H$$

where $\mu^{(0)} \to \infty$. Convergence is achieved when $\mu^{(n-1)} = \mu^{(n)}$ to the desired degree of accuracy.

When the γ oscillations are observed without feedback, a plot of $\ell n \frac{A}{T}$ vs. T/H results in curves for all but the first harmonic. This is shown in Figure 14. Application of near-optimal feedback promptly straightens out these curves as shown in Figure 15. Table II shows the effective masses measured with near optimal feedback in the [110] direction, along with their counterparts derived from data given by Phillips and Gold (1969).

Table II

Effective Mass for Observed Oscillations in Pb:H [110]

Oscillation	μ(Measured)	μ(Derived)
α	1.08	1.10±0.01
$\alpha+\gamma$, $\alpha-\gamma$	1.74	1.66±0.02
γ fundamental	0.565	0.56±0.01
γ 2nd Harmonic	1.00	1.12±0.02
γ 3rd Harmonic	1.35	1.68±0.03

[Values of μ (measured) are derived from the slopes of Figure 15 for non-optimal feedback]

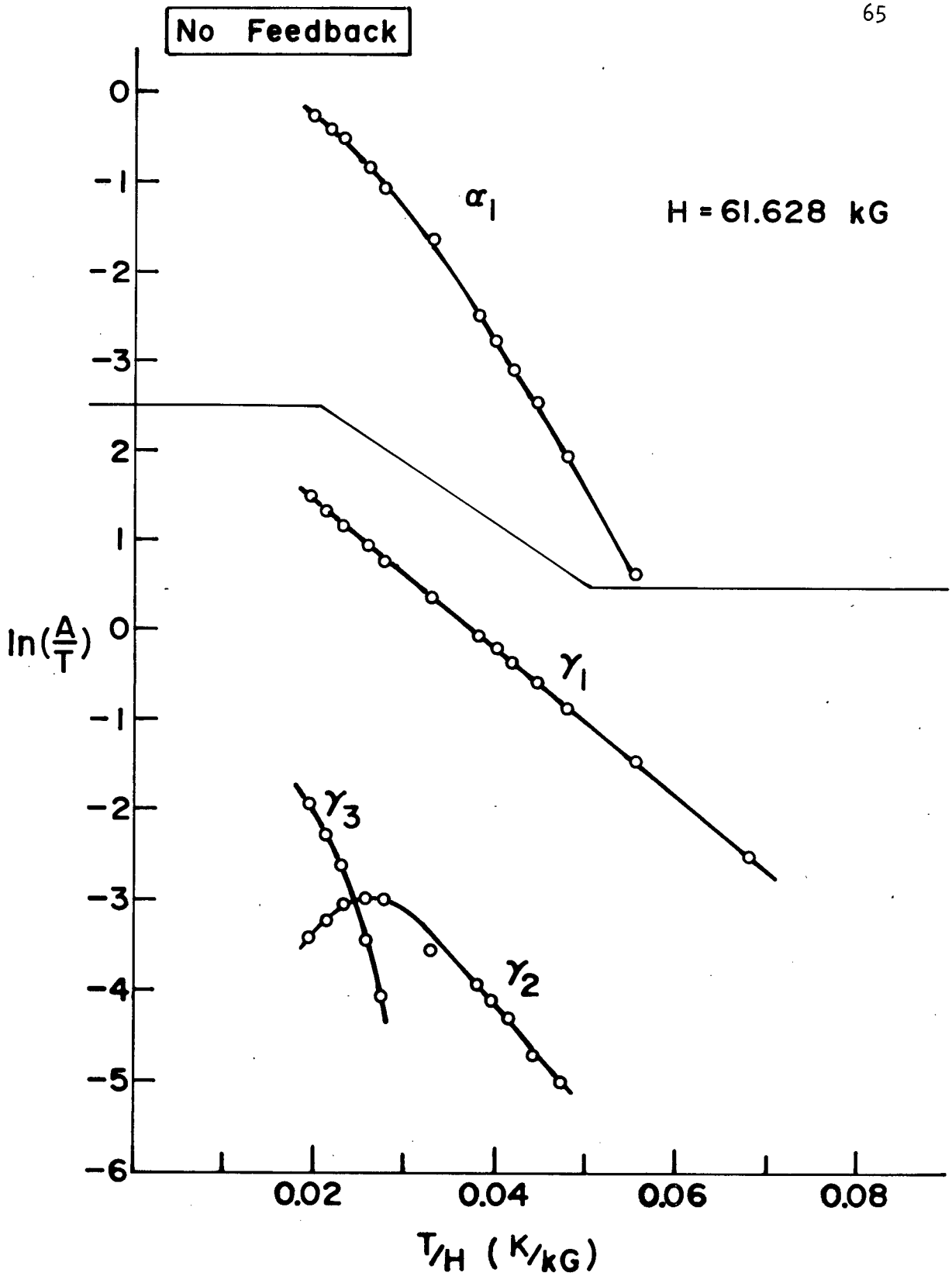

Figure 14. Mass Plots With No Feedback

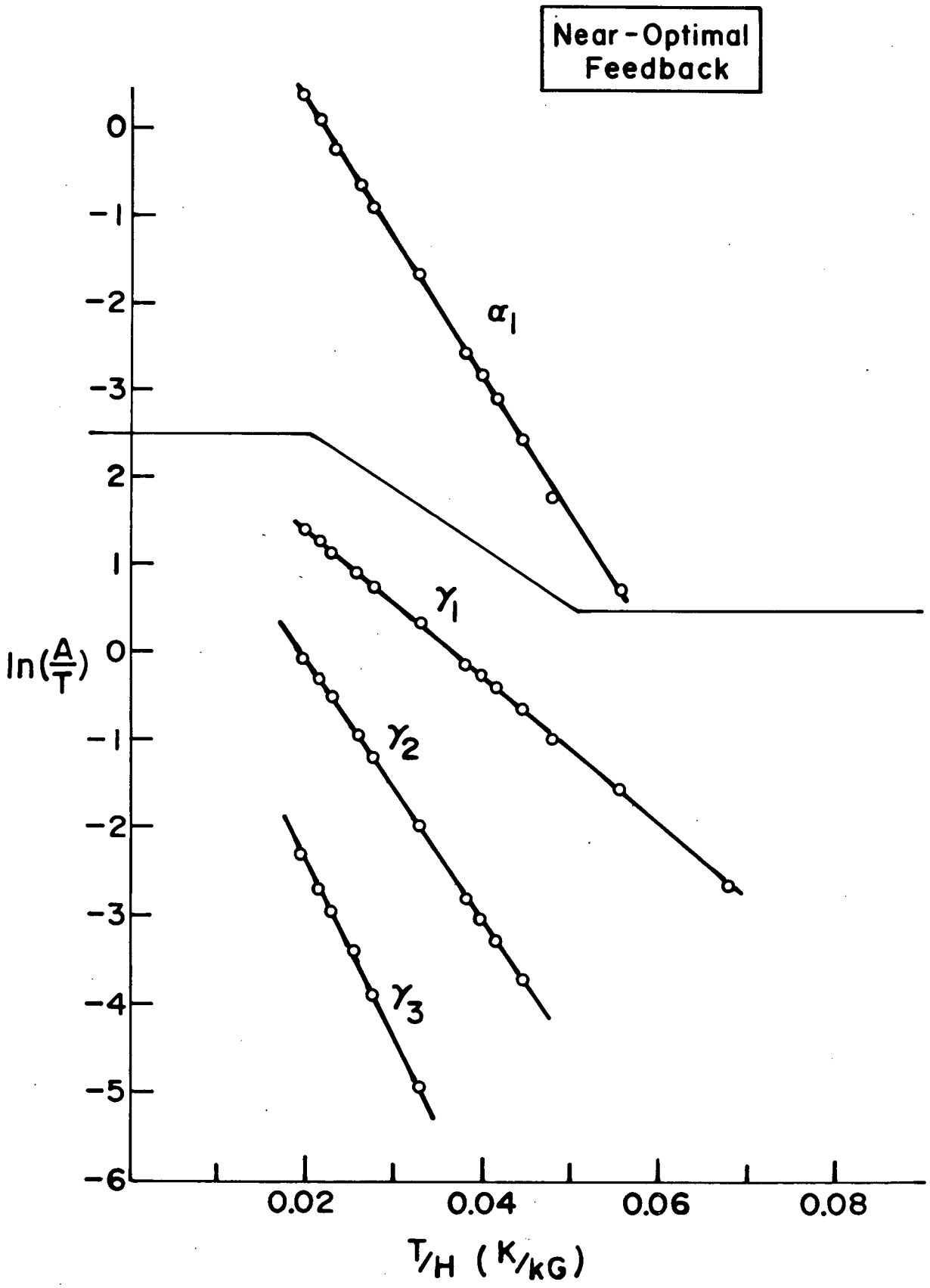

Figure 15. Mass Plots With Near-Optimal Feedback

The agreement for the fundamental oscillations is good, which is to be expected because they are essentially unaffected by M.I. The combination terms $\alpha+\gamma$, $\alpha-\gamma$, are generated by M.I., and in the simple approximation

$$A_{\alpha\pm\gamma} = \frac{A_\alpha A_\gamma}{2} (f_\alpha \pm f_\gamma) .$$

The temperature dependence is

[33] $$A_{\alpha\pm\gamma}(T) = T^2 \, e^{-\lambda(\mu_\alpha+\mu_\gamma)T/H}$$

Our measured value comes from the slope of a plot of $\ln \frac{A_{\alpha\pm\gamma}}{T^2}$ vs. T/H, and the derived value is the sum of μ_γ and μ_α. In the ideal theory, the ratio $\mu_1:\mu_2:\mu_3$ is 1:2:3. The derived values in Table II are μ_1, $2\mu_1$ and $3\mu_1$, since μ_1 can be measured with minimal interference from M.I. Upon measurement of these values, we found them not in accord with this ratio suggesting the presence of residual M.I. In order to take account of the residual M.I., present because the feedback gain was not set to optimum, the conventional theory of M.I. is applicable.

In the conventional theory, if A represents the L.K. amplitude, and A' is the interacting amplitude,

[34] $$A_2' = A_2 \left\{ 1 - \frac{\kappa \varepsilon A_1^2}{\sqrt{2}\, A_2} + 1/2 \left(\frac{\kappa \varepsilon A_1^2}{\sqrt{2}\, A_2} \right)^2 \right\}^{1/2}$$

To find the amount of M.I. still present, we calculate A_2' from [34] adjusting ε until the temperature dependence plot yields the ideal effective mass.

Writing $A_1 = \xi_1 \, X \, e^{-X}$ and $A_2 = \xi_2 \, X \, e^{-2X}$ to extract the temperature dependence, we obtain

$$[35] \qquad A_2' = \xi_2 \, X \, e^{-2X} \{1 - \zeta X + 1/2 \, \zeta^2 \, X^2\}^{1/2}$$

where $$\zeta = \frac{\kappa \varepsilon \, \xi_1^2}{\sqrt{2} \; \xi_2}$$

and

$$[36] \qquad \ell n \left[\frac{A_2'}{X[1 - \zeta X + 1/2 \zeta^2 X^2]^{1/2}} \right]$$

Plotting the left side of this equation against T/H should yield an ideal slope of $-2\lambda\mu_\gamma \simeq 165$. A numerical calculation gave the value $\zeta = 0.62$ as the best fit line with the desired slope. With this value of ζ, the correction factor $[1 - \zeta X + 1/2 \, \zeta^2 X^2]^{1/2}$ attains the values 1.47 to 0.71 between 3.4K and 1.2K, respectively which is appreciable, but not drastic enough to warrant further terms in the expansion.

The same treatment can be applied to the third harmonic. The conventional interacting theory in the presence of feedback gives (see [7c]).

$$[37] \qquad A_3' = A_3 \left\{ 1 - \frac{3\kappa \varepsilon \, A_1 A_2}{\sqrt{2} \; A_3} + 1/2 \left(\frac{3\kappa \varepsilon \, A_1 A_2}{\sqrt{2} \; A_3} \right)^2 \left[1 - 1/2 \left(\frac{\kappa \varepsilon \, A_1^2}{\sqrt{2} \; A_2} \right) \right] + \left(\frac{3 \, \kappa^2 \varepsilon^2 A_1^3}{8 \, A_3} \right)^2 \right\}^{1/2} .$$

As before $A_3 = \xi_3 \; X \; e^{-3X}$, and introducing

$$\eta = \frac{\xi_2^2}{\xi_1 \xi_3} \quad , \quad \text{the equation becomes}$$

[38] $$A_3' = A_3\{1-3\zeta\eta X + 1/2\,(3\zeta\eta X)^2[1-1/2\,\zeta X]+(3/4\,\zeta^2\eta X^2)^2\}^{1/2}$$

The curly brackets give the correction factor, so that plotting $\ell n \frac{A_3'}{X\{\;\}^{1/2}}$ vs. T/H should give a slope of $-3\lambda\mu_\gamma$ for the appropriate choice of η. Using the value of ζ calculated before, a value of $\eta = 1.1$ yields the correct slope for the third harmonic temperature dependence.

The agreement of the calculation with the expected results suggests we correctly understand the mechanics of the non-optimal feedback setting, and hence we can use the slopes of the mass plots as a criterion for realizing optimum feedback. The mass plots made at optimum feedback are shown in Figure 16. The largest source of scatter was the temperature measurement; this is indicated in Figure 16 by a systematic shift in the points of each line which were taken at the same temperature. The ratio of the slopes are now 1:2:3 within 4%. The γ_1 data were known to be insufficiently far into the high thermal smearing limit, and the correction term developed earlier was employed in their analysis.

6.4 The Beat Pattern

The dominant contribution to magnetic interaction usually comes from the fundamental dHvA frequency since it is usually the

Figure 16. Mass Plots at Optimum Feedback

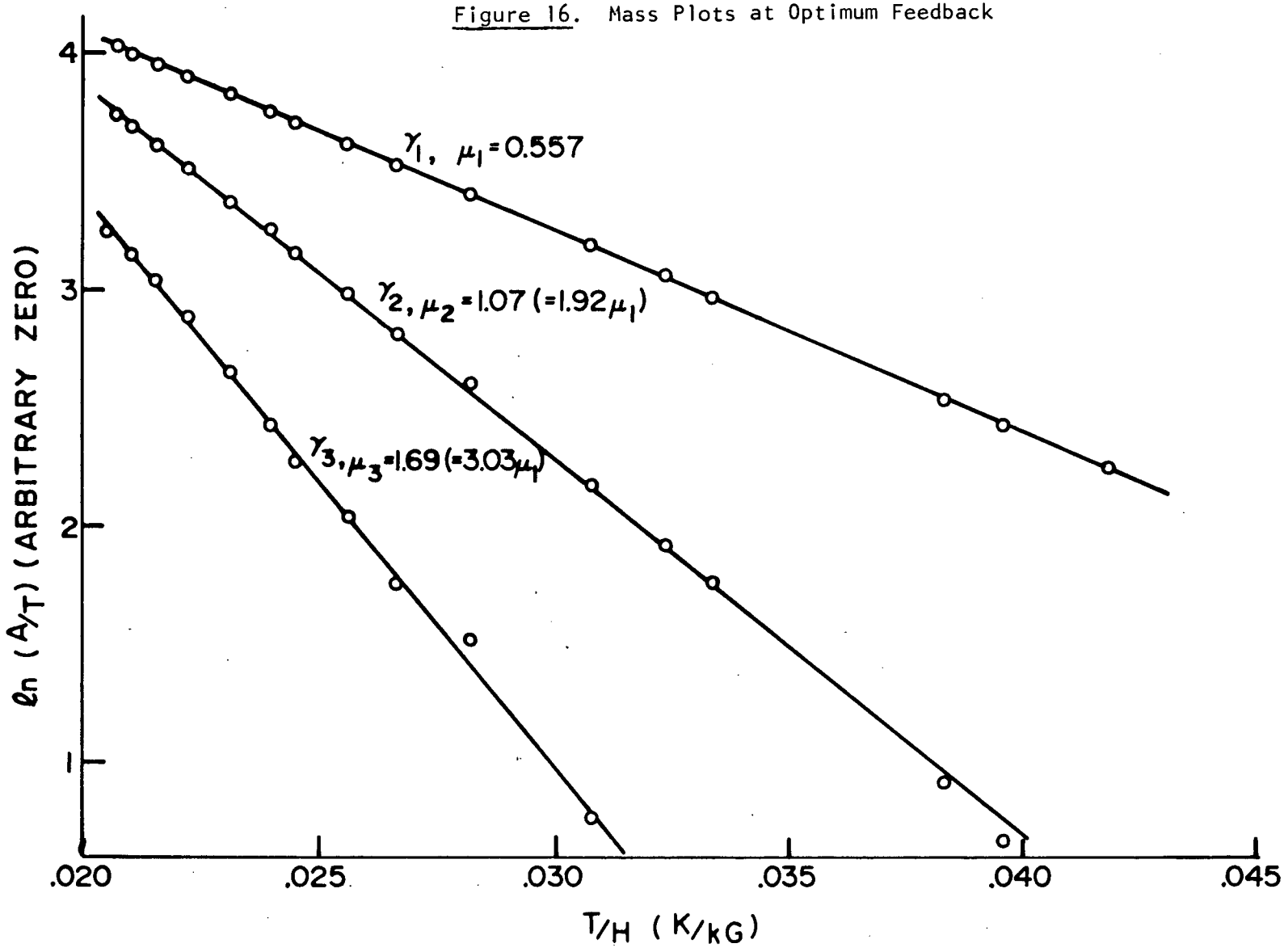

strongest. If there are two neighbouring frequencies present, and beating occurs, the terms from M.I. at the second harmonic frequency will beat with a frequency equal to that of the fundamental beats rather than at twice the fundamental beat frequency as would normally be expected. The same is true for all the M.I. harmonics. As a result, the beat frequency will only be proportional to the harmonic index (r) if there is no M.I. present.

In lead along [110], we have such a situation with the γ frequencies (see Figure 11). The fundamental is about a factor of 10 stronger than the second harmonic, and the fundamental beat frequency is roughly 0.42 MG. In the ideal theory we can represent the magnetization due to the two γ frequencies (γ^a, γ^b) by

$$M^a = \sum_r A_r^a \sin\left[2\pi r\left(\frac{F+\delta F}{H} - \gamma\right) - \pi/4\right]$$

$$M^b = \sum_r A_r^b \sin\left[2\pi r\left(\frac{F-\delta F}{H} - \gamma\right) + \pi/4\right]$$

and $$M^{total} = M^a + M^b$$

where $$\delta F = F^a - F^b \text{ and } F^a > F^b$$

The sign reversal of the phase factor $\pi/4$ is required since the area of one of the corresponding Fermi surface areas is a maximum, while the other is a minimum. (see Ogawa and Aoki (1978)).

If we let $\eta = \dfrac{A^a - A^b}{A^a + A^b}$, then elementary trigonometric manipulations lead to

$$[39] \qquad M^{total} = \sum_r (A_r^a + A_r^b)\frac{\sqrt{2}}{2}\{(1+\eta^2)+(1-\eta^2)\sin(2\pi r\delta F/B)\}^{1/2} \times \sin\left[2\pi r\left(\frac{\overline{F}}{B} - \gamma\right) + \psi_r\right]$$

where $$\psi_r = \tan^{-1}\{\eta \tan\left(\frac{\pi r\delta F}{B} - \pi/4\right)\}$$

and $$\overline{F} = \frac{F^a + F^b}{2}$$

Unfortunately, the phase of the beats is very sensitive to orientation. This is clearly shown by the large spread in field values of the minima reported in the literature. This sensitivity results from the relatively low symmetry in the γ oscillations along [110]. Beats in oscillations corresponding to orbits of higher symmetry such as β at [100] do not appear to be so sensitive.

The beat envelopes for the first three γ harmonics without feedback are shown in Figure 17. The envelope of the first harmonic appears as we expect, however that of the second harmonic clearly has the periodicity of the first. The third harmonic beat envelope has a part which is beating at thrice the fundamental beat frequency however, the position at the field corresponding to a first harmonic maximum has higher amplitude, indicating that at least some of the amplitude is due to terms generated from M.I.

With near-optimal feedback, shown in Figure 18, the second harmonic appears to be approaching a beating pattern at twice the fundamental frequency. The third harmonic is still affected by M.I. effects.

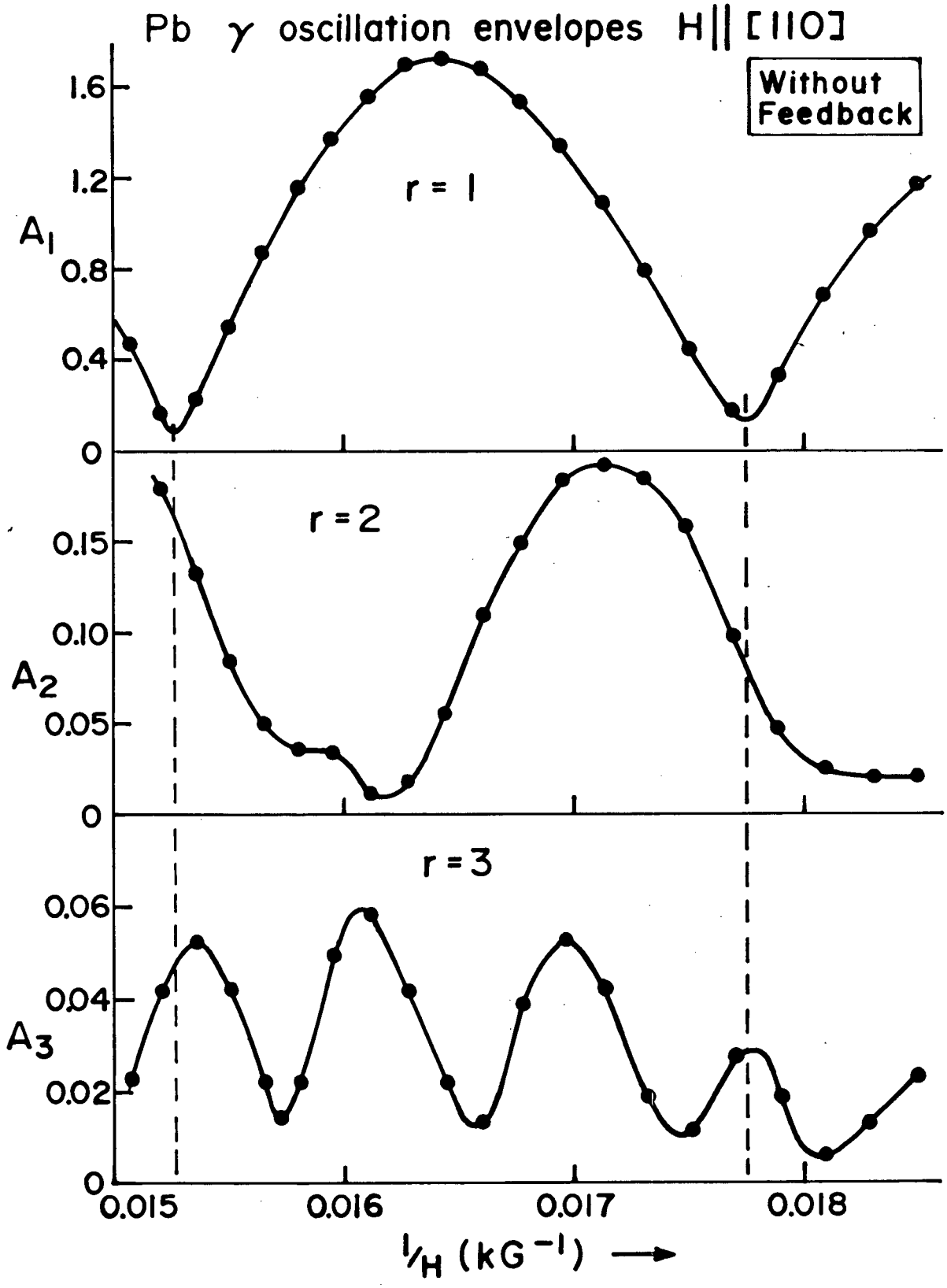

Figure 17. Beat Envelopes Without Feedback (A_1, A_2, A_3 in Gauss)

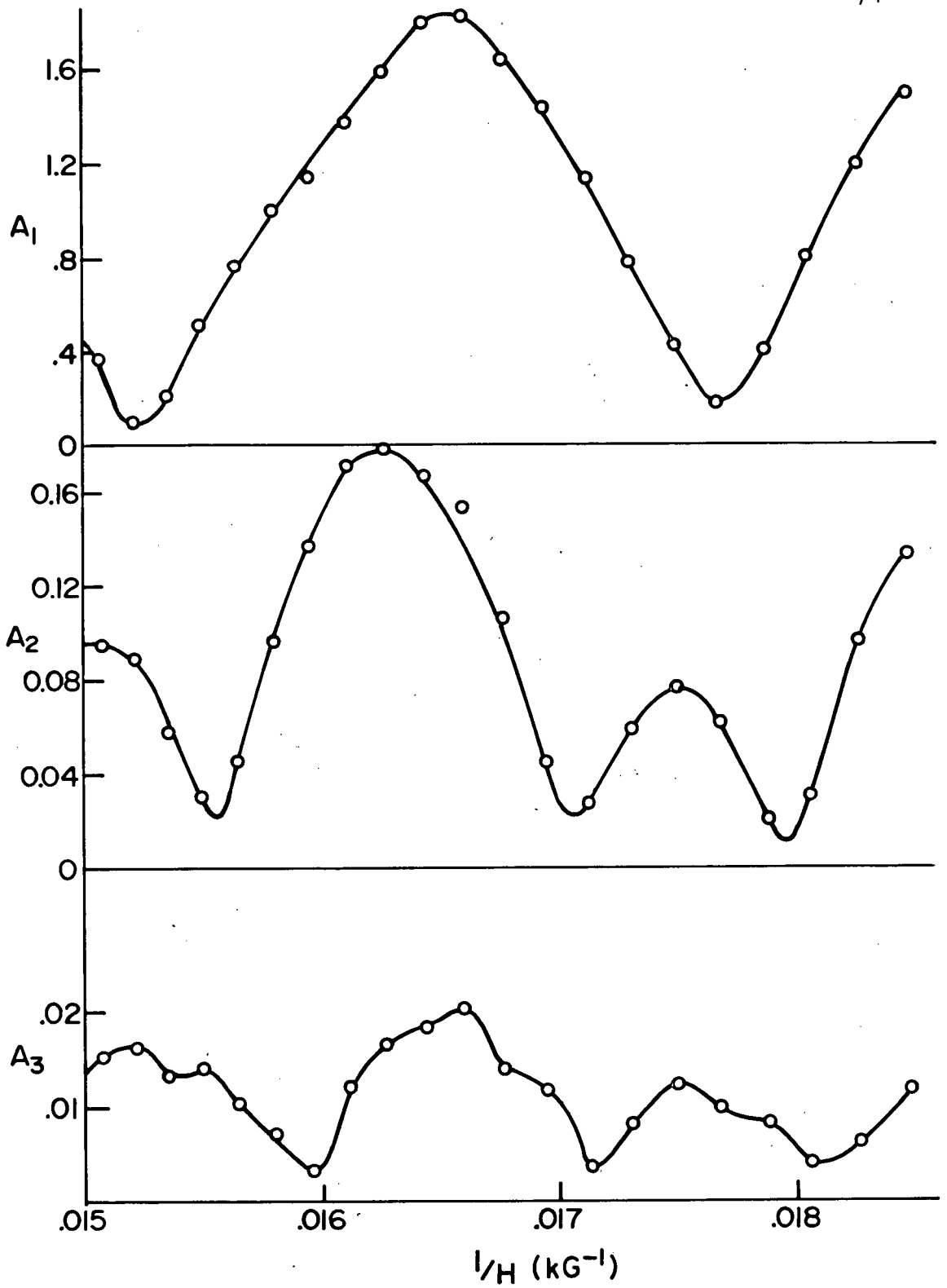

Figure 18. Beat Envelopes With Near-Optimum Feedback (A_1, A_2, A_3 in Gauss)

Concentrating on the second harmonic, we observe a sequence of alternating large and small beat maxima. The apparent beat period also alternates.

To explain these results we can call upon a result derived earlier (see [7b]) for the second harmonic amplitude in the presence of M.I., and feedback, namely,

$$[40] \qquad A_2' = A_2\left[1-\frac{1}{\sqrt{2}}\ \frac{\kappa\varepsilon\ A_1^2}{A_2} + 1/4\ \left(\frac{\kappa\varepsilon\ A_1^2}{A_2}\right)^2\right]^{1/2}$$

where $\kappa = \dfrac{8\pi^2 F}{H^2}$

If we take the limit as A_2 approaches zero, we obtain Shoenberg's "strong fundamental" result

$$[41] \qquad A_2' = \pm A_1^2\ \kappa\varepsilon$$

Upon substitution of the beating amplitude of the fundamental A_1 into [41], we can find the contribution of A_1 at the second harmonic.

We see from Figure 17 that it is a good approximation to take the amplitudes of the individual γ oscillations to be equal, $A_r^{(a)} = A_r^{(b)}$. The magnetization due to the fundamentals is then

$$\tilde{M}^{(1)} = A_1\ \{\sin\ [2\pi(\frac{\overline{F} - \frac{\delta F}{2}}{H} - \gamma) - \pi/4]$$

$$+\ \sin\ [2\pi(\frac{\overline{F} - \frac{\delta F}{2}}{H} - \gamma) + \pi/4]\}$$

or

$$[42] \qquad \tilde{M}^{(1)} = 2A_1\{\sin[2\pi(\frac{\overline{F}}{H} - \gamma)]\ \cos[2\pi(\frac{\delta F}{2H}) - \pi/4]\}$$

The envelope is given by

$$2A_1 \cos\left[\frac{2\pi\delta F}{2H} - \pi/4\right]$$

so that the magnetization amplitude appearing at the second harmonic due to the first is

$$\tilde{M}^{(2)} = \frac{-\kappa\varepsilon}{2}\{4A_1^2 \cos^2\left[2\pi\left(\frac{\delta F}{2H}\right) - \pi/4\right]\}$$

or

$$[43] \qquad \tilde{M}^{(2)} = -\kappa A_1^2 \varepsilon\{1 + \cos\left[2\pi\left(\frac{\delta F}{H}\right) - \pi/2\right]\}$$

The genuine second harmonic gives

$$\tilde{M} = A_2\{\sin\left[2\pi\left(\frac{2\bar{F}+\delta F}{H} - 2\gamma\right) - \pi/4\right] + \sin\left[2\pi\left(\frac{2\bar{F}-\delta F}{H} - 2\gamma\right) + \pi/4\right]\}$$

or

$$[44] \qquad \tilde{M} = 2A_2 \sin\left[2\pi\left(\frac{2\bar{F}}{H} - 2\gamma\right)\right] \cos\left(\frac{2\pi\delta F}{H} - \pi/4\right)$$

Adding the 2 contributions gives the total magnetization amplitude at the second harmonic

$$[45] \qquad \tilde{M} = 2A_2 \cos\left(\frac{2\pi\delta F}{H} - \pi/4\right) - \kappa\varepsilon A_1^2\left[1 + \cos\left(\frac{2\pi\delta F}{H} - \pi/2\right)\right]$$

The contribution from the first harmonic can be verified by using an alternate approach. From [12] for two frequencies, the contribution at the sum frequency is

$$[46] \qquad A_{SUM} = -\frac{\kappa_a \varepsilon A_a^2}{2} \sin(2x_a) - \frac{\kappa_b \varepsilon A_b^2}{2} \sin(2x_b) - \frac{\varepsilon A_a A_b}{2} [(\kappa_a + \kappa_b) \sin(x_a + x_b)]$$

Substitution of the two γ fundamental frequencies gives:

$$A_{SUM} = \frac{-\kappa A_1^2 \varepsilon}{2} \{\sin[2\pi(\frac{2\bar{F} + \delta F}{H} - 2\gamma) - \pi/4] + \sin[2\pi(\frac{2\bar{F} - \delta F}{H} - 2\gamma) + \pi/4]\} - \frac{A_1^2 \varepsilon}{2} \cdot 2\kappa \sin[2\pi(\frac{2\bar{F}}{H} - 2\gamma)].$$

Elementary trigonometric manipulations lead to:

$$[47] \qquad \tilde{M} = -\kappa \varepsilon A_1^2 [\cos(\frac{2\pi\delta F}{H} - \pi/2) + 1] \sin[2\pi$$

which reproduces the amplitude in [43].

The interacting result [45] should fit the near-optimal feedback data. In order to obtain values for A_1 and A_2 to fit the curve, one can find the zeros, and match the period ratio, that is, insist that every other beat period be shorter by the observed amount. The zeros of the calculated second harmonic amplitude are determined from

$$2A_2 \cos(2\pi\frac{\delta F}{H} - \pi/4) - \kappa \varepsilon A_1^2 \{1 + \cos(\frac{2\pi\delta F}{H} - \pi/2)\} = 0$$

or

$$[48] \qquad \frac{2A_2}{\kappa A_1^2 \varepsilon} \cos(\frac{2\pi\delta F}{H} - \pi/4) = 1 + \cos(\frac{2\pi\delta F}{H} - \pi/2)$$

[48] is a transcendental equation which can be solved numerically, and iteration leads to a value of $\frac{2A_2}{\kappa A_1^2 \varepsilon}$ for which the ratio of the beat periods agree with the observed response. The details are simply clerical and will not be included, however, a plot of the ratio of the two apparent second harmonic beat periods as a function of $\frac{\kappa A_1^2 \varepsilon}{2A_2}$ appears in Figure 19. At $\varepsilon = 0$ which is equivalent to saying there is no M.I., the corresponding ordinate is 1, indicating the equivalence of all beat periods. The value of 0.737 on the ordinate corresponds to that observed in the near-optimal feedback setting of Figure 18. This ordinate corresponds to

$$\frac{2A_2}{\kappa A_1^2 \varepsilon} = 4.91$$

A similar calculation was done assuming $A_2<0$ which yields the result:

$$\frac{2A_2}{\kappa A_1^2 \varepsilon} = -3.41.$$

Using these solutions, the calculated interacting second harmonic was plotted along with the calculated first harmonic beat envelope in Figure 20. The biggest difference between the positive and negative solutions for $\frac{2A_2}{\kappa A_1^2 \varepsilon}$ is the relative phase of the second harmonic minima with respect to the first harmonic minima. Upon comparison with the measured data (see Figure 18), it becomes obvious that A_2 is indeed negative. With the negative solution

Figure 19. Calculation of the Ratio of the Apparent Beat Periods of γ_2 vs. $\frac{\kappa A_1^2 \varepsilon}{2A_2}$

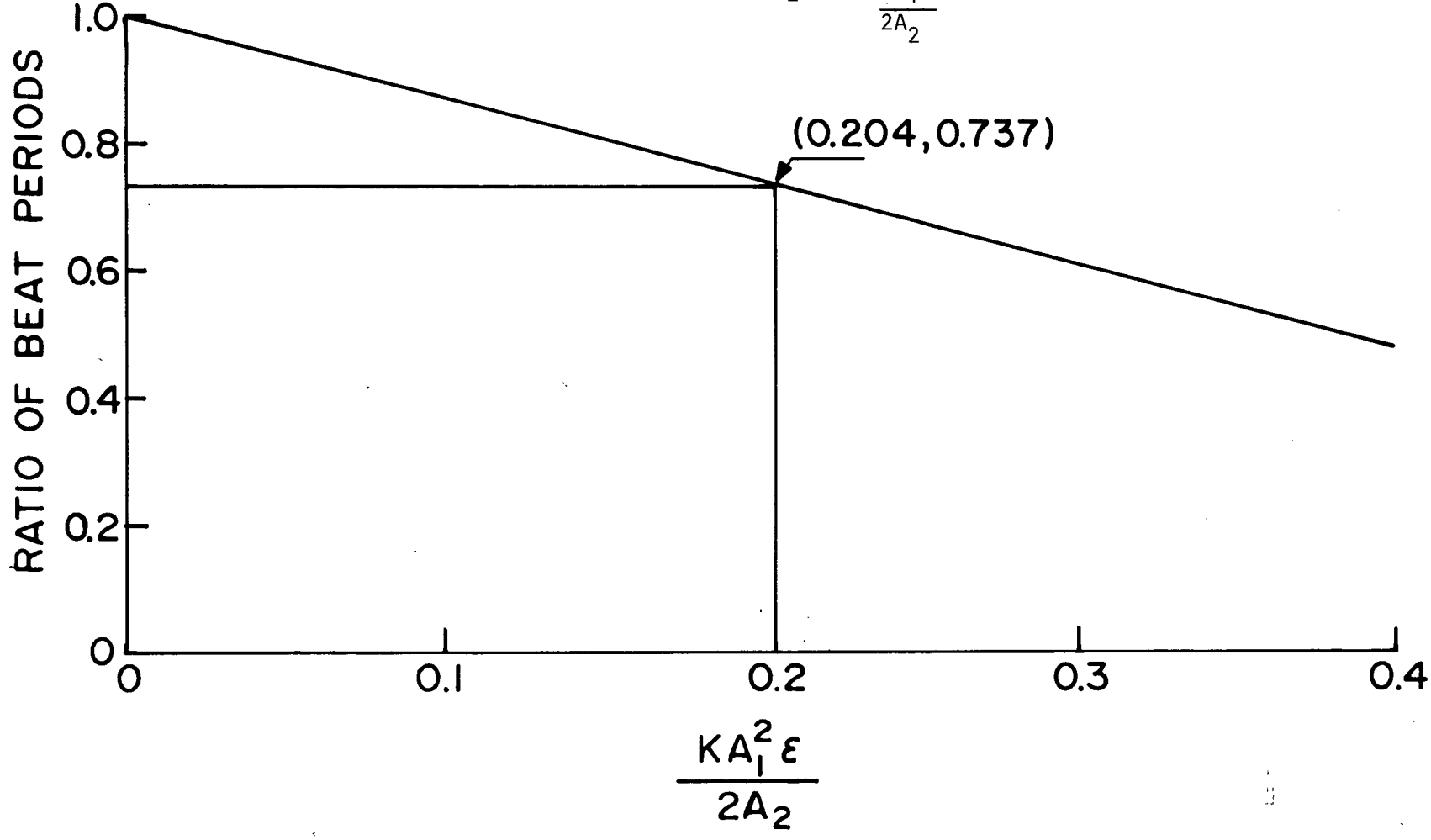

Figure 20. Calculated Solutions For A_2.
$A_2 < 0$: dashed line; $A_2 < 0$: solid line

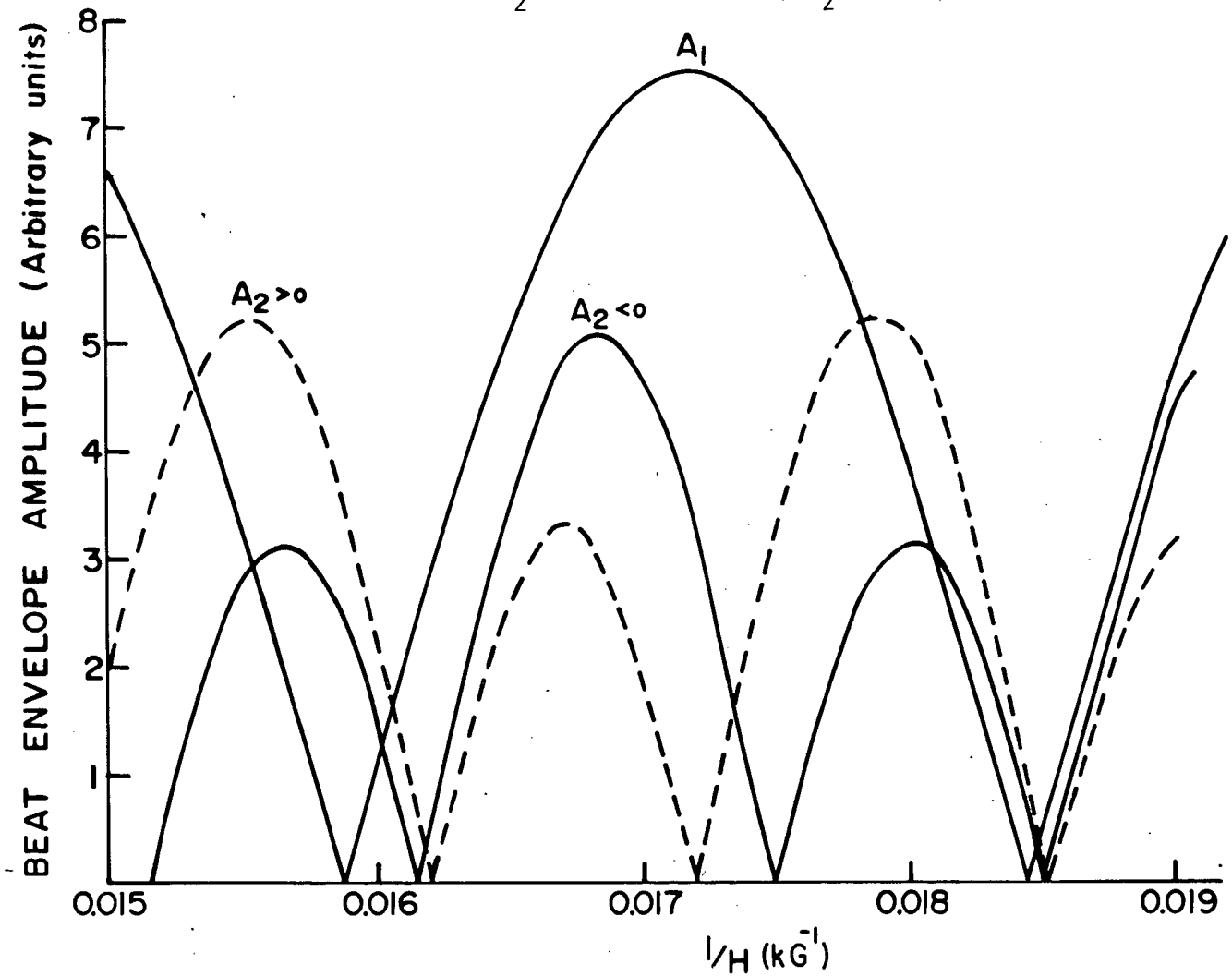

the agreement is really quite good, especially in the relative phase of the first harmonic minimum with respect to the second harmonic minimum. The calculation predicts the 2 minima of the second harmonic to be displaced from a fundamental minimum by $\Delta\ (\frac{2\pi\delta F}{2H}) = 0.748$ rad and 4.33 rad . The observed result from Figure 16 is $\Delta\ (\frac{2\pi\delta F}{2H}) = 0.75$ rad and 4.5 rad.

The calculation of the interacting result for the third harmonic follows similar calculations, but the complexity is much greater, especially in the transcendental equations determining A_3. Since the procedure worked well with the second harmonic, the third harmonic equations were solved by computer. An option in the program enabled us to take the Fourier transform at each field setting requested which is more in keeping with the way the data was obtained experimentally. This program is included in Appendix C.

One could correct the temperature dependence of the near-optimal feedback data by extracting this dependence from the calculated interacting result. This was done at a field corresponding to a maximum in the ideal second harmonic beat envelope. At this fixed field H_o, the arguments of the cosines in the interacting results are constant, and the temperature dependence is extracted from A_1 and A_2. H_o is independent of feedback gain since it is the field at a maximum of the ideal beat envelope. The temperature dependence is:

$$[49] \qquad A_2'(T) \propto \left| \frac{2A_2}{\kappa A_1^2 \varepsilon} \right| \cos\left(\frac{2\pi\delta F}{H_o} - \pi/4\right) + \left\{1 + \cos\left(\frac{2\pi\delta F}{H_o} - \pi/2\right)\right\}$$

$$\propto 2A_2 \left\{\cos\left(\frac{2\pi\delta F}{H_o} - \pi/4\right) + \frac{\kappa A_1^2 \varepsilon}{2A_2}\left[1 + \cos\left(\frac{2\pi\delta F}{H_o} - \pi/2\right)\right]\right\}$$

but

$$\frac{\kappa A_1^2 \varepsilon}{2A_2} = \frac{\kappa \xi_1^2 \varepsilon X^2}{2\xi_2 X} = \frac{\kappa \xi_1 \varepsilon}{2\xi_2} \cdot \frac{1}{X}$$

The quantity $X = \lambda\mu\, T/H$ contains all the temperature dependence, so, letting X_o be the value of X where

$$\frac{\kappa A_1^2 \varepsilon}{2A_2} = \left(\frac{\kappa A_1^2 \varepsilon}{2A_2}\right)_o \quad (= -3.41 \text{ in our case})$$

then

$$\frac{\kappa A_1^2 \varepsilon}{2A_2} = \frac{X}{X_o} \cdot \frac{1}{\left(\frac{2A_2}{\kappa A_1^2 \varepsilon}\right)_o}$$

letting $a = \cos\left(\frac{2\pi\delta F}{H_o} - \pi/4\right)$

and $b = \left\{1 + \cos\left(\frac{2\pi\delta F}{H_o} - \pi/2\right)\right\} \cdot \frac{1}{\left(\frac{2A_2}{\kappa A_1^2 \varepsilon}\right)_o}$

we obtain a temperature dependence of

$$A_2'(T) = 2A_2 \,[a + bX]$$

hence, plotting

$$\ell n\left[\frac{A_2'}{X\{a+bX\}}\right] \quad \text{vs. } T/H$$

should yield a slope of $-2\lambda\mu$.

In our data, $a = 0.642$, $b = 0.352$,

and we obtain a slope of 167 kG/K which corresponds to $\mu = 0.568$. This result, calculated from the second harmonic near-optimum feedback data is in excellent agreement with that derived from the fundamental amplitude (see Table II).

The above agreement again demonstrates the understanding of the detailed mechanisms involved in near-optimal feedback, and we now move on to the optimum feedback position, the results appearing in Figure 21. With optimum feedback, the beat frequencies of the first three harmonics are in the ratio 1:2:3.

From the ideal non-interacting beat envelopes which are now available to us thanks to the use of optimum feedback, it appears that there is a favoured field setting within each fundamental beat cycle where the three beat envelopes are simultaneously close to their maximum values, and the slopes are not very large. This occurs at roughly 1/3 of the way into the beat envelope plotted against 1/H (shown as $1/H_1$ in Figure 22). These positions, affectionately called "magic fields" are the optimum fields to perform a three harmonic measurement. The amplitudes of the harmonics are close to but not at their beat maxima, so that a field dependence measurement is needed to determine the actual relative amplitudes from those measured at the "magic field". Simulation of such a plot appears in Figure 22, with the correction for the fundamental shown

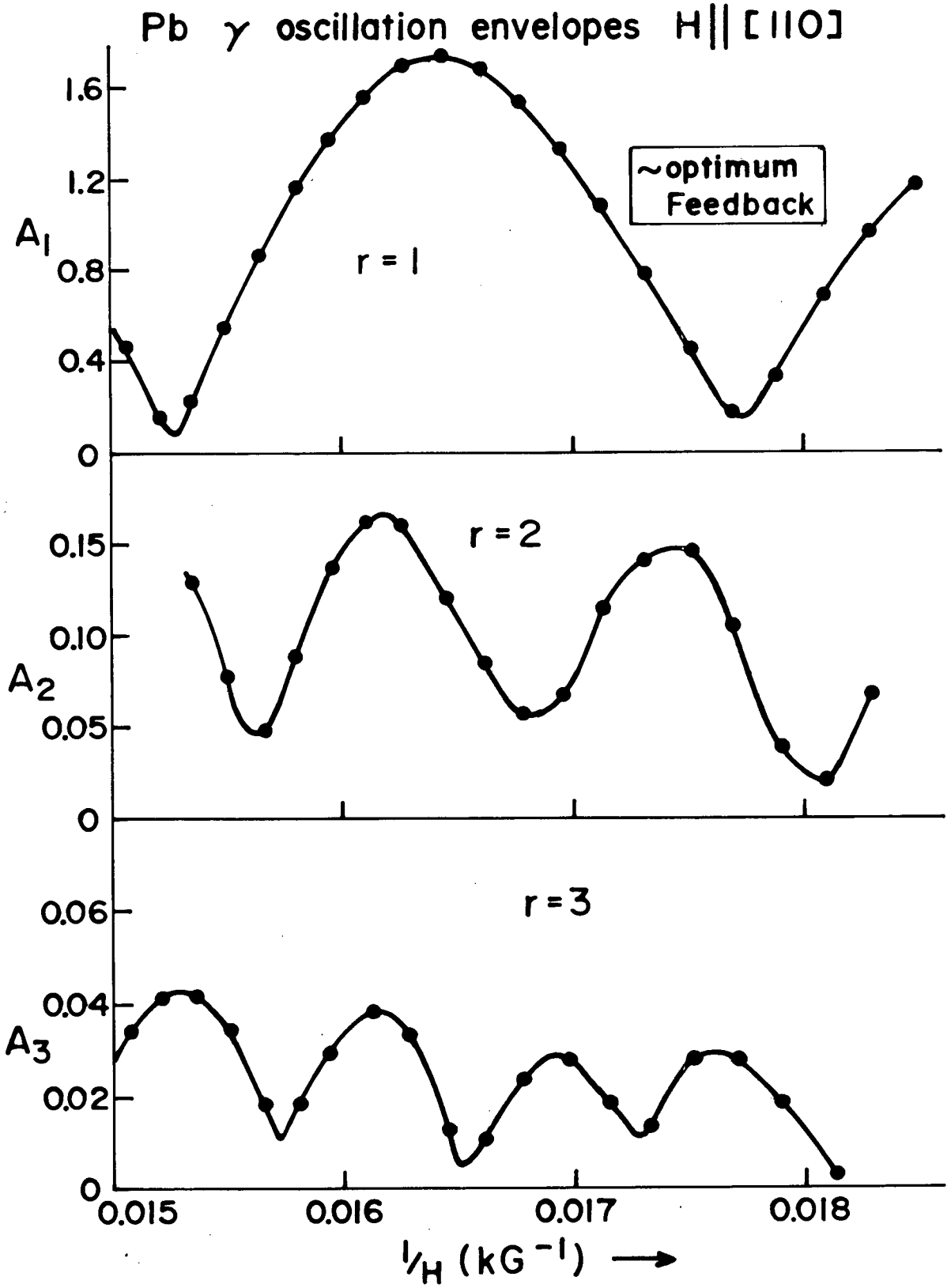

Figure 21. The Beat Envelope With Optimum Feedback

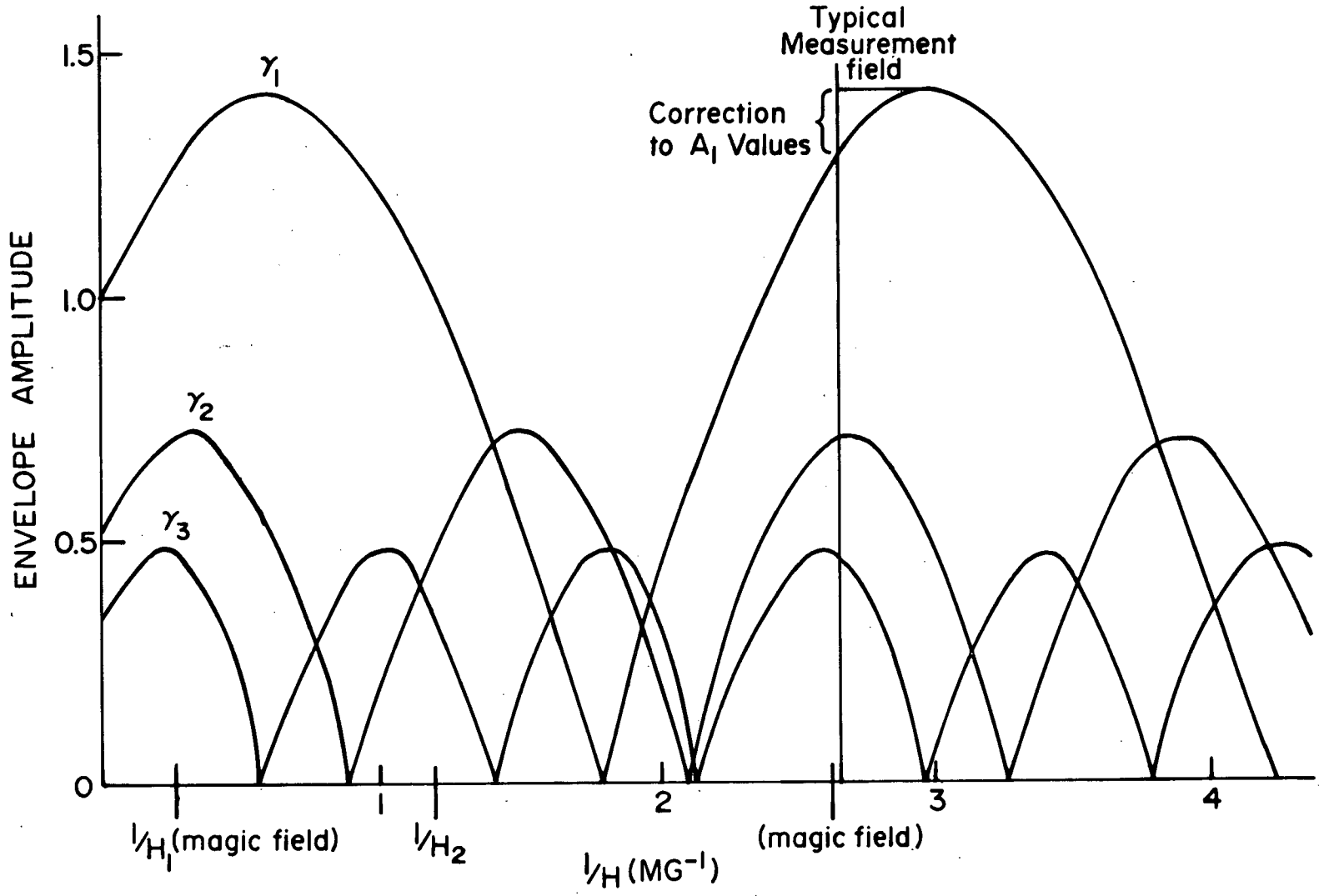

Figure 22. Ideal L.K. Beat Envelopes

The corresponding empirical result for the fundamental appears in Figure 27.

6.5 Phase Information

The value of the argument of the sinusoid describing the dHvA effect is quite large ($\sim 10^4$). Absolute phase measurements thus require great precision in field and orientation if they are to be considered reliable. Fortunately, the phase relationships between harmonics can be measured reliably. However, since we are considering different frequencies (i.e., F_1, $F_2=2F_1$, $F_3=3F_1$), the relative phase must be defined with some care.

The standard definition of the phase shift between a variation of the form $\sin(\omega t+\psi_1)$ and its r^{th} harmonic $\sin(r\omega t+\psi_r)$ involves the construction of a reference sinusoid with frequency ω crossing zero with a positive slope at some arbitrary $t = 0$ (any convenient $t = 2m\pi/\omega$ where $m = 1, 2, 3...$ would also do). Associated with this fundamental reference is another at a frequency $r\omega$ crossing zero with a positive slope at the same $t = 0$. If the phase difference between the fundamental signal and the reference is ϕ_1 and the corresponding quantity for the r^{th} harmonic is ϕ_r, then the quantity $r\phi_1 - \phi_r$ is a constant and serves as the definition of the phase difference.

When dealing with a signal which is the sum of two close frequencies, the short-range modulation may not be enough to resolve the individual frequencies in the Fourier transform. In this case, one must calculate the resultant phase in order to compare with the experiment.

We have already presented the results of a numerical substitution in the envelope equation for a pair of beating oscillations (see [39] plotted in Figure 22). The two inverse fields $1/H_1$ and $1/H_2$ correspond to Figures 23 and 24 where the individual oscillations are plotted out to determine the relative phase. With reference to Figure 22, both the second and third harmonics have undergone one zero crossing between $1/H_1$ and $1/H_2$ but the first has not. At $1/H_2$ we therefore expect the second and third harmonics to have the opposite phase relationship to the first harmonic when compared to that at $1/H_1$. This is indeed shown in Figures 23 and 24. $1/H_1$ corresponds to one of the "Magic fields" (see section 6.4). Figure 23 shows that at the first of these fields i.e. the one with the lowest value of 1/H, the phase difference between the first three harmonics is zero. Generalizing [6] to allow for the phases ψ_r in the presence of beats, and feedback, we obtain

$$[50] \qquad A_2' = A_2 \sin(2x+\psi_2) - 1/2\ \kappa\varepsilon\ A_1^2 \sin(2x+2\psi_1).$$

In addition, from [39] for small η we see that ψ_1 and ψ_2 can attain only 2 values, 0 and π. This makes the two terms in [50] either in phase or π out of phase depending on the sign of A_2, and the value of ψ_2. If the two terms compete in the presence of M.I., we expect a phase reversal of the measured phase of A_2' if the magnitude of the second term in [50] exceeds that of the first. In any case the measured phase difference should for small η (narrow beat waists) be 0 or π. The measured phase difference as a function of feedback gain

Figure 23. Individual Oscillations Near the "Magic Field" $1/H_1$ of Figure 22

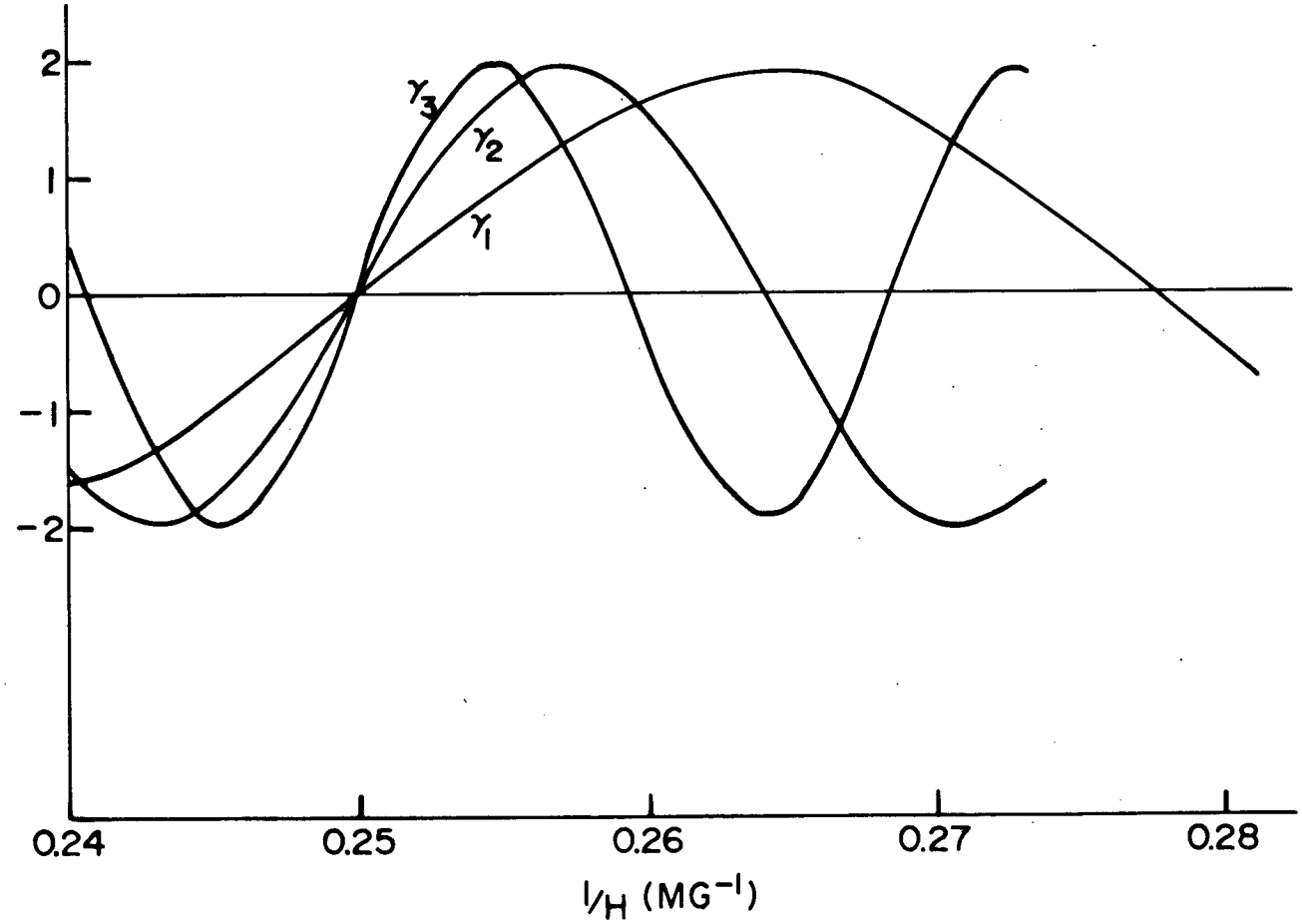

Figure 24. Individual Oscillations Near $1/H_2$ of Figure 22

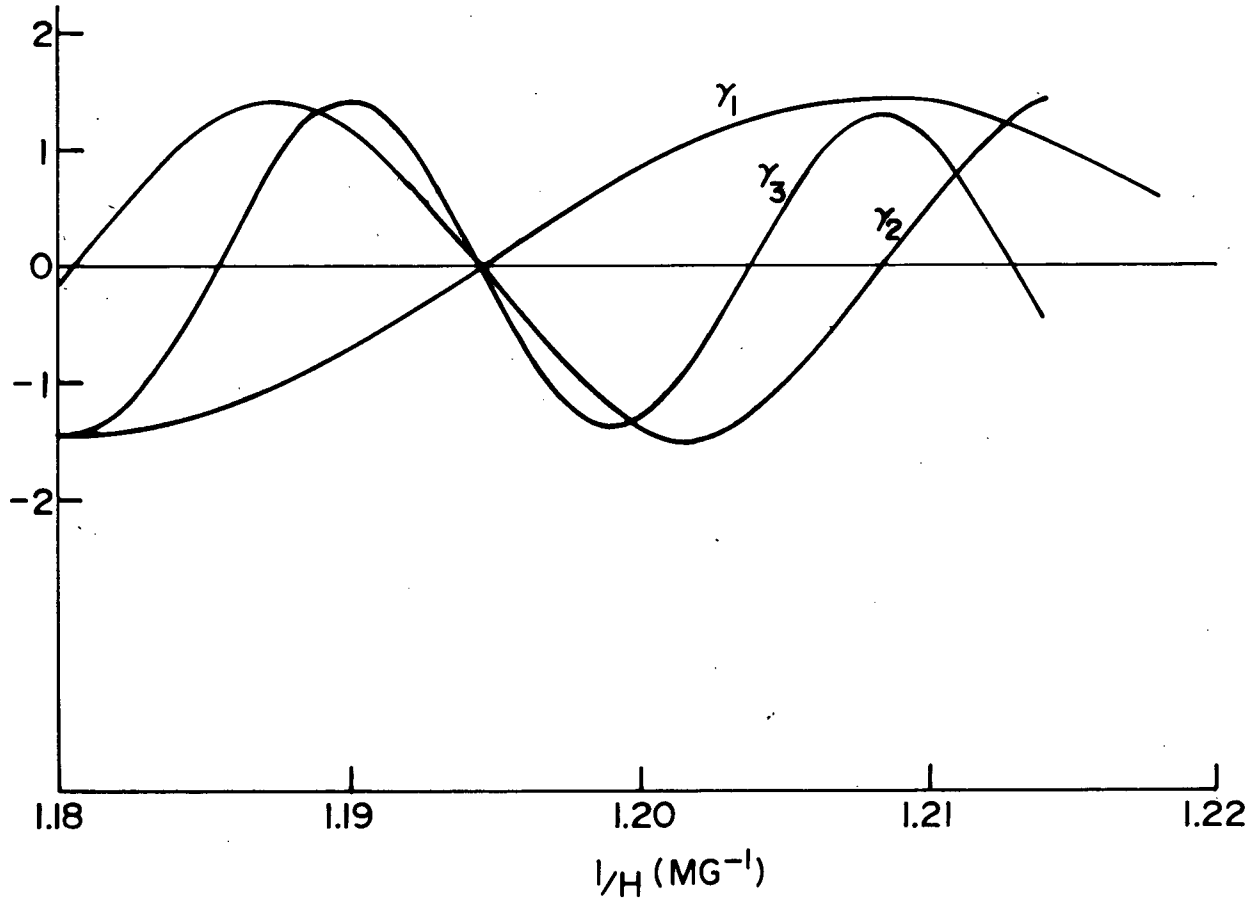

Figure 25. Measured Phase Difference and Amplitude of γ_2 at a Magic Field (61.739 kG)

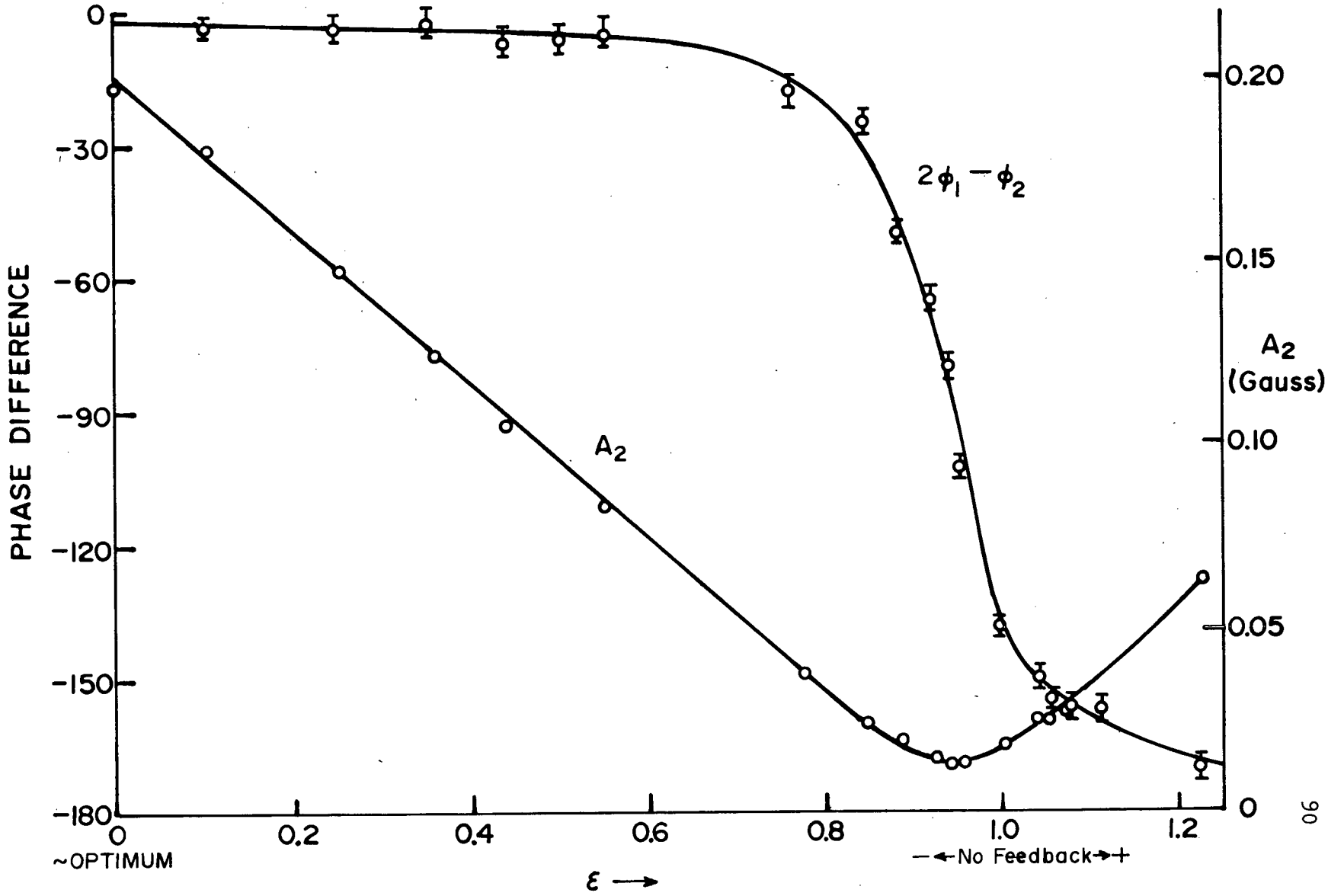

at a magic field appears in Figure 25. Included in this figure is the second harmonic amplitude dependence. From [50] we see that A_2 should be a linear function of ε for small η in [39].

Phase measurements at other parts of the beat cycle were not reliable since the amplitudes of the oscillations were changing quickly, and the large modulation smears the phase.

6.6 The Linearity of A_1/A_3 vs. $(A_1/A_2)^2$

In Chapter II, we found that information leading to the g_c factor comes from the straight line plot of A_1/A_3 vs. $(A_1/A_2)^2$. This line is straight only if the ideal L.K. behaviour is realised. Figure 26 shows plots of this kind for data without feedback and with optimum feedback. The linearity and low scatter in the graph with feedback is surprisingly good to one who has made these plots using other techniques to deal with M.I. This figure shows very dramatically the drastic way in which M.I. interferes with amplitude information, and how this interference has been successfully removed by the feedback technique.

6.7 Conclusions

Before using the feedback technique to measure quantities such as the g_c factor, we must be confident that the technique is working properly, and know the limits within which we can work. This chapter demonstrates the consistency and the effectiveness which feedback has in reducing M.I.

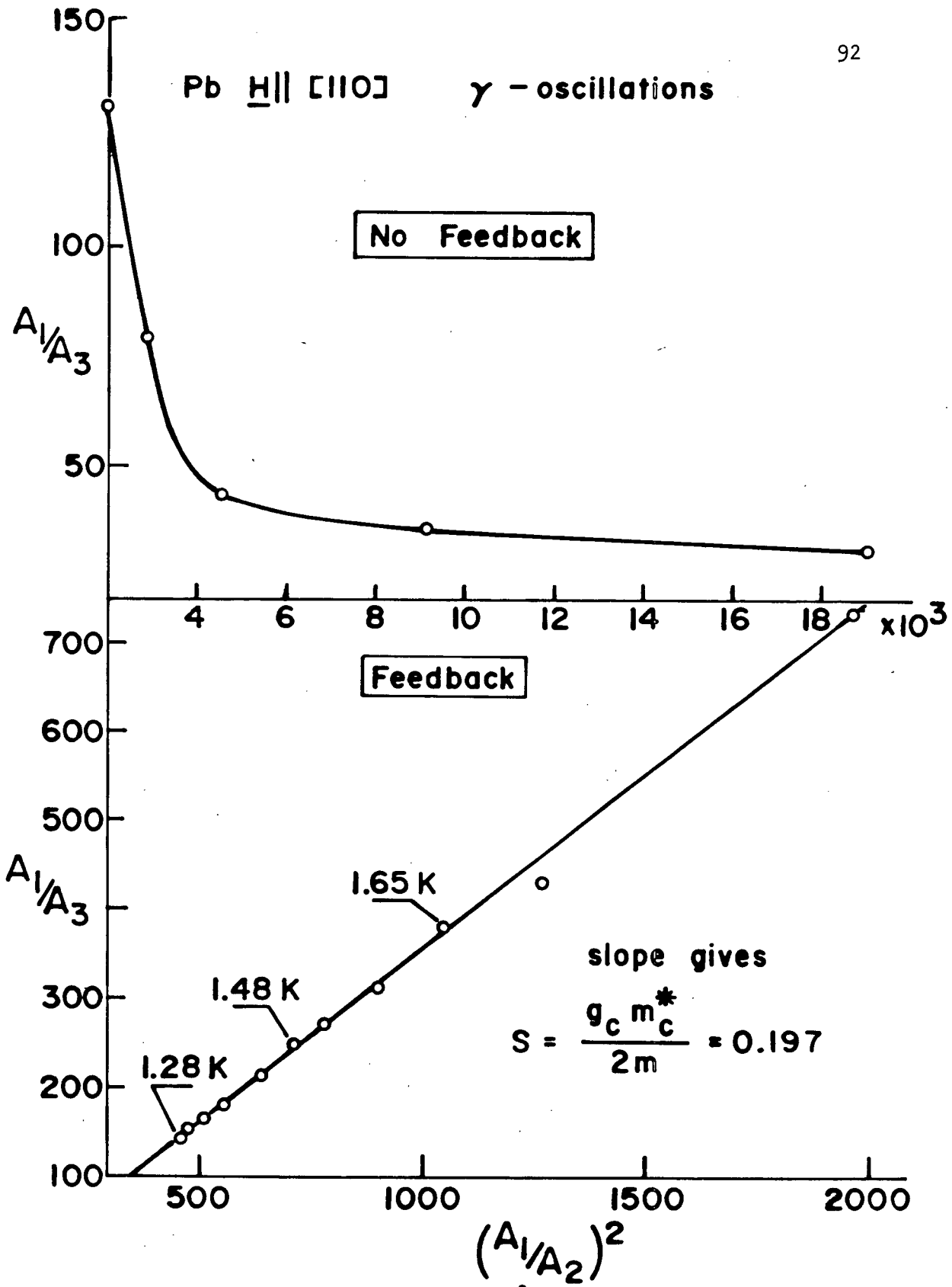

Figure 26. A_1/A_3 vs. $(A_1/A_2)^2$ With and Without Feedback. H is constant at 61.794 kG, and the bath temperature T is varied.

The calculations involving non-optimum and near-optimum feedback give consistent agreement with the experimental results, demonstrating the understanding of the role of feedback in the experiment. Only for the $\alpha + \gamma$ sideband amplitude (Figure 13) do we find a systematic deviation from theoretical expectation. This is presumably related to the non-vanishing of the $\alpha + \gamma$ and $\alpha - \gamma$ sidebands at optimum feedback, and is not yet fully understood. In every other case of optimum feedback, the data conform to the results expected for ideal L.K. behaviour, and it must be stressed that in each section of this chapter, the phrase "optimum feedback" refers to the same feedback gain i.e., the optimum setting for one experiment is the same for all the others. This consistency gives one confidence that the same optimum feedback setting will give reliable g_c factor measurements.

While most of the chapter deals with non-optimum feedback, it clearly demonstrates that at the optimum feedback gain no corrections for M.I. need be applied.

CHAPTER SEVEN

EXTRACTION OF g_c FACTOR FROM A_1/A_3 vs. $(A_1/A_2)^2$ PLOTS

To apply the algorithm presented in Chapter II let us recall a few results:

[3a] $$A_1/A_3 = \alpha_\infty \left[(A_1/A_2)^2 - 1/4\,(A_1/A_2)_0^2\right]$$

[3b] $$(A_1/A_2)_0 = 2\sqrt{2}\ \exp\ (XT_D/T)\ \cos \pi S/\cos 2\pi S$$

[2b] $$\alpha_\infty = (\sqrt{3}/2)(1-\tan^2 \pi S)^2/(1-3\ \tan^2 \pi S) = \lim_{X \to \infty} \left(\frac{A_2^2}{A_1 A_3}\right)$$

$(A_1/A_2)_0$ is independent of the temperature T.

From [3a] we see that the slope of the graph of $|A_1/A_3|$ vs. $(A_1/A_2)^2$ (holding the field H constant, and varying the temperature T) is α_∞. [2b] can easily be inverted to give

[51] $$\tan^2 \pi S = 1 - \sqrt{3}\ \alpha_\infty \left[1 \pm \sqrt{1 - \frac{4\sqrt{3}}{9\alpha_\infty}}\right]$$

The value $|\alpha_\infty|$ from a least squares fit to the points in Figure 26 is $|\alpha_\infty| = 0.392$. The square root in [51] yields an imaginary result for $\alpha_\infty = + 0.392$ so we must conclude that $\alpha_\infty = -0.392$. This implies $A_1/A_3 < 0$. The real solutions of [51] are $S = 0.330$ or 0.197. These values are modulo 1 because of the periodicity of the function $\tan^2 \pi S$. To decide between these two principal values for S we measure the abscissa intercept in Figure 26 to obtain $1/4\ (A_1/A_2)_0^2$ as can be seen from [3a].

[3b] can easily be inverted to give Dingle temperatures corresponding to the two solutions for S.

$$[52] \qquad T_D = \frac{H}{\lambda\mu}\, \ell n\, \left[\frac{(A_1/A_2)_0 \cos 2\pi S}{2\sqrt{2} \cos \pi S}\right]$$

From the least squares fit to the points in Figure 26, $1/4\ (A_1/A_2)_0^2 = 91.0$. Using [52] and the experimental parameters used in the experiment, along with the effective mass μ found in Chapter VI, our previous solutions for S correspond to the following Dingle temperatures

$S = 0.330, \quad T_D = 1.42K, \quad A_1/A_2 < 0$

$S = 0.197, \quad T_D = 0.749K, \quad A_1/A_2 > 0$

The Dingle temperature can also be obtained from the field dependence of the fundamental amplitude and [1b]; only a rough estimate is necessary. In the approximation $X \gtrsim 3$, the complete field and temperature dependence is given by

$$A_1 \alpha (T/\sqrt{B}) \exp \{- \lambda\mu (T/B)(1 + T_D/T)\}$$

so that

[53] $$\ell n(A_1\sqrt{B}) = -\lambda\mu (T/B)(1 + T_D/T)$$

From [53] we see that a plot of $\ell n (A_1\sqrt{B})$ vs. 1/B can give the Dingle temperature. The fact that A_1 is beating does not change this, as long as the points used on the graph are at the same position in the beat cycle. The obvious choice is to use the field and the amplitude at the maxima of the beat pattern.

Figure 27 shows a plot of A_1 vs. 1/H, and a least squares fit to the maxima for T = 1.25K gives

$$-\lambda\mu (T/B)(1+T_D/T) = -164.5 \text{ or } T_D = 0.750K$$

It is quite evident that S = 0.197 is the proper principal value. The phase measurements give $A_1/A_2 > 0$ consistent with this choice. We are thus left with only the trigonometric multiplicity according to which possible solutions are $S = \pm 0.197 \pm P$, $P \varepsilon 1$ each of which gives identical experimental results.

For simple metals such as lead, where the band structure can be derived from a weak pseudopotential together with the spin-orbit interaction, a physical argument given by Pippard (1969) restricts the range of possible values of S according to the

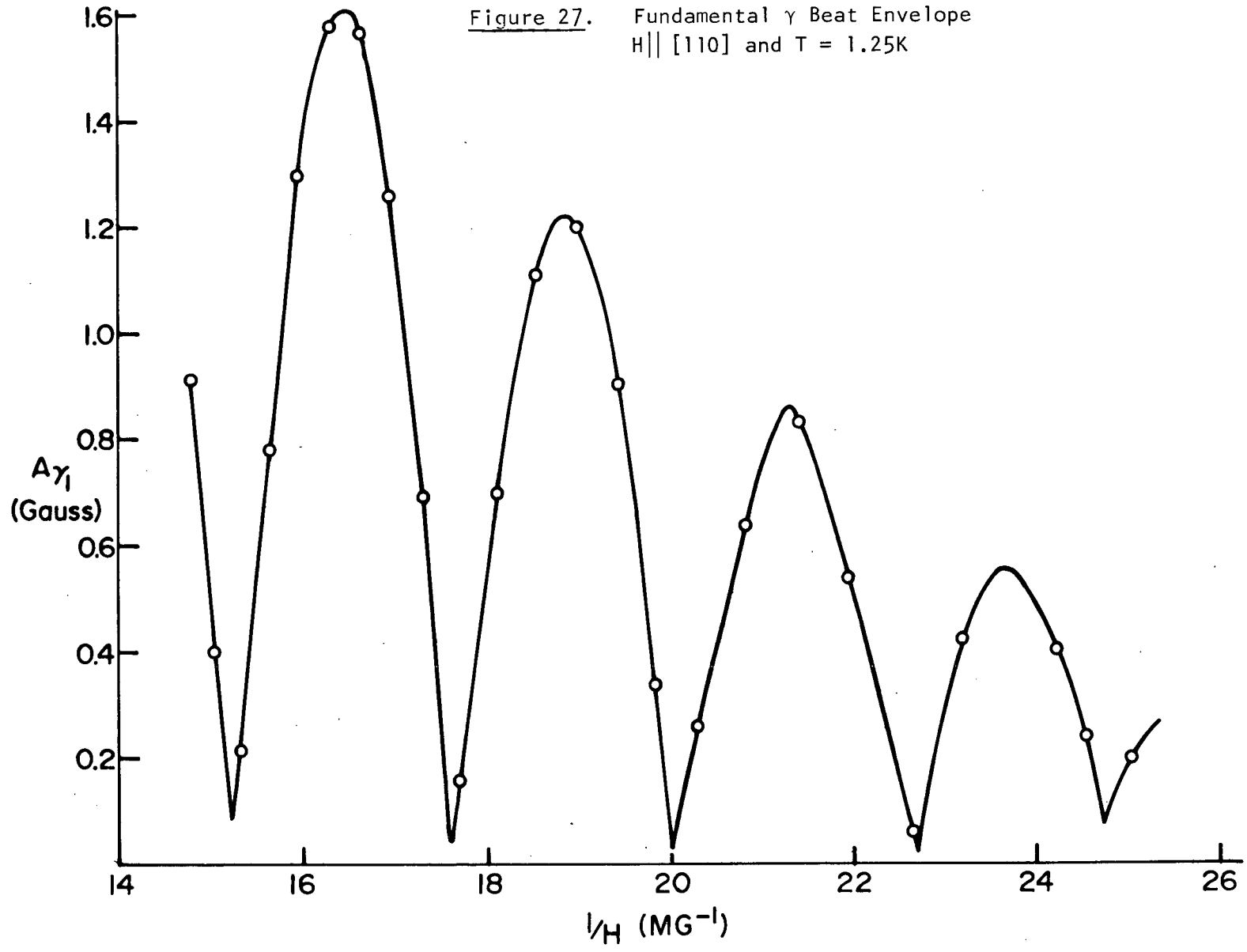

Figure 27. Fundamental γ Beat Envelope
H|| [110] and T = 1.25K

inequality

$$S \leq (m_c^*/m) + (s/2)$$

where s is the number of Bragg reflections undergone by an electron in one cyclotron orbit. This value is 3 for the ζ orbit normal to [110] which gives rise to the γ oscillation, so that with $m_c^*/m = 0.560$, we have

$$0 < S < 2.06$$

Of the 4 values of S which fall into this interval (0.197, 1.197, 0.803, 1.803) two give $A_1/A_2 < 0$ which is inconsistent with the phase and Dingle temperature criteria. We are thus left with the two possible solutions.

$$S = g_c\, m_c^*/2m = 0.197 \text{ and } 1.803$$

corresponding to $g_c = 0.704$ and 6.44 respectively.

The ultimate choice between these 2 relies on a band calculation which includes the spin-orbit interaction.

CHAPTER EIGHT

A SEARCH FOR THE 4MG OSCILLATIONS

8.1 Preliminary Remarks

Quantum oscillations of unusually long period ($\sim$ 4MG) have been observed recently in lead using the Shubnikov-de Haas effect (Tobin et. al., 1969) and sound attenuation (Ivowi and Mackinnon, 1976).

It has been suggested that these long oscillations might arise from small pockets of electrons in the 4th Brillouin zone. While pockets of this kind appear in the empty lattice band structure, all realistic band calculations fitted to the Fermi surface data show the 4th zone to be empty.(c.f. Anderson and Gold, 1965). We are thus led to wonder whether the long oscillations might be an artifact generated by M.I.

A concerted effort was made to detect similar oscillations in the dHvA effect with the hope that they could then be studied with the feedback technique. Unfortunately, no evidence for these long oscillations could be found, so that only an upper limit on their amplitude resulted. In the process of

the search, some useful ideas were developed including the exact solution to the problem of large modulation.

8.2 Review of the Standard Weak-Modulation Solution

Field modulation, followed by phase-sensitive detection, is the most widely used technique for observation of the de Haas van Alphen effect. The problem of calculating the e.m.f. induced in a pick-up coil surrounding the sample has been solved in detail for weak modulation fields. There are, however, circumstances which warrant rather large modulation fields, large enough so that some of the approximations made in the weak-modulation treatment may no longer be valid. One such circumstance is the detection of long-period oscillations such as those reported by Tobin et.al. (1969) having frequencies $F \sim 4$ MG. It is then desirable to modulate with an amplitude $\gtrsim 1$ kG which is a sizeable fraction of the quasi-static background field. We first review the standard formulation for weak modulation, and then develop an exact, explicit solution for arbitrary strength of modulation field.

In its present widely-used form, the modulation field h is sinusoidal, small with respect to the large background field H, and is parallel to it. Thus, the sample experiences a net field $H + h \sin \omega t$. The large background field is made to sweep slowly, so that in treating the modulation field, we can regard the background field as essentially constant. The

criterion for this assumption is

$$\left(\frac{dh}{dt}\right)_{RMS} << \frac{dH}{dt}$$

The treatment for weak modulation is well known, and will just be outlined here.

Without loss of generality, we can ignore various constant phase factors, and write the oscillatory part of the magnetization simply as:

$$\tilde{M} = \sin \left[\frac{2\pi F}{H + h(t)}\right]$$

where $h(t) = h \sin \omega t$ and ω is the modulation angular frequency. The equation is for a reduced magnetization, with the amplitude factors incorporated into it. We might also add that we must work at a low enough frequency ω so that we have no field inhomogeneity due to eddy currents.

In the conventional approximation, the denominator is expanded, and only the linear term in $\frac{h}{H}$ is retained, so that

$$\tilde{M} \approx \sin \left[\frac{2\pi F}{H} \left(1 - \frac{h(t)}{H}\right)\right]$$

Since the approximation is made in the argument of a rapidly oscillating sine function, ($\frac{2\pi F}{H} \sim 10^3$ typically) one must be careful to state the justification correctly.

The criterion to be satisfied must assure that the argument is at most first order in $\frac{h}{H}$. This is true if and only if the second order term is very much less than 2π. The second order term is:

$$\frac{2\pi F}{H}\left(\frac{h(t)}{H}\right)^2$$

So the justification is

$$\frac{2\pi F h^2}{H^3} << 2\pi$$

or simply

$$\frac{F h^2}{H^3} << 1.$$

If this inequality is not satisfied, the argument of the sine must be taken to be at least quadratic in h. This "weak modulation" criterion is usually met in the normal laboratory situation, and $\tilde{M}$ can be developed in a Fourier series as follows

$$\tilde{M} = \sin\left[\frac{2\pi F}{H}\left(1 - \frac{h(t)}{H}\right)\right]$$

$$= \frac{1}{2i}\left(e^{i\frac{2\pi F}{H^2}(h\sin\omega t)}e^{-i\frac{2\pi F}{H}} - e^{-i\frac{2\pi F}{H^2}(h\sin\omega t)}e^{i\frac{2\pi F}{H}}\right)$$

Using the identity

$$e^{-i\,\mu\,\sin y} = \sum_{n=-\infty}^{\infty} J_n(\mu)\, e^{-i\,n\,y}$$

we obtain

$$\tilde{M} \approx \frac{1}{2i}\left[e^{i\frac{2\pi F}{H}} \sum J_n\left(\frac{2\pi FH}{H^2}\right) e^{-in\omega t} - e^{-i\frac{2\pi F}{H}} \sum J_n\left(\frac{2\pi Fh}{H^2}\right) e^{in\omega t}\right]$$

The coil surrounding the sample gives a voltage proportional to $\frac{d\tilde{M}}{dt}$. Taking this derivative,

$$\frac{d\tilde{M}}{dt} \approx -\sum_{n=-\infty}^{\infty} n\omega\, J_n\left(\frac{2\pi Fh}{H^2}\right) \cos\left(\frac{2\pi F}{H} - n\,\omega\,t\right)$$

We now separate the t and H dependences, and find after a little manipulation

$$\frac{d\tilde{M}}{dt} \approx -\sum_{n=1}^{\infty} 2n\omega\, J_n\left(\frac{2\pi Fh}{H^2}\right) \sin\left(\frac{2\pi F}{H} + n\frac{\pi}{2}\right) \sin\left(n\omega t + \frac{n\pi}{2}\right)$$

This is the conventional result for weak modulation. We note in passing that the same result is obtained if the sign of the two phase factors $\frac{n\pi}{2}$ is reversed.

8.3 Large Modulation

By large modulation we mean that our initial assumption about the linearity of the sine argument breaks down. In particular, for the long oscillations having F ∿ 4 MG in an

applied field of 50 kG, for maximum response, we should

modulate over something like one cycle of the waveform which makes h $\sim$ 325 Gauss. Our criterion for neglect of the second, and high order terms was

$$h << \sqrt{H^3/F}$$

Any such long oscillation in the dHvA effect would be swamped by the strong γ oscillations with a frequency of 17 MG, making

$$\sqrt{H^3/F} \approx 2.7 \text{ kG} \qquad (H = 50 \text{ kG})$$

For this situation, it cannot be said that h is then very much less than $\sqrt{H^3/F}$, and it was felt that a deeper study into the effects of the quadratic, and higher order terms, was warranted. A common practice is to exploit the zeros of the Bessel functions to eliminate the unwanted oscillations. Our object, in part, is to determine possible shifts of these zeros when using large modulation fields.

We now present an exact Fourier decomposition which is valid for <u>any</u> strength of modulation. In our basic equation,

$$\tilde{M} = \sin\left[\frac{2\pi F}{H+h\cos\omega t}\right]$$

we can use the cosine phase of the modulation without loss of generality, since the result cannot be dependent on the origin

of time. This choice of phase makes $\tilde{M}$ an even function of time t which simplifies the planned Fourier expansion of the sine argument.

Because only the even, cosine terms can survive, we can write the expansion as:

$$\frac{2\pi F}{H + h\cos\omega t} = \sum_{n=0}^{\infty} a_n \cos n\omega t$$

where

$$a_o = \frac{2\omega}{\pi} \int_0^{2\pi/\omega} \frac{2\pi F}{H + h\cos\omega t}\, dt$$

and

$$a_n = \frac{\omega}{\pi} \int_0^{2\pi/\omega} \frac{2\pi F}{H + h\cos\omega t} \cos n\omega t\, dt$$

These integrals may be reduced to standard form, and we readily obtain (Gradshyeyn and Ryzhik, 1965)

$$a_0 = \frac{2\pi F}{H\sqrt{1-(\frac{h}{H})^2}}$$

$$a_n = \frac{4\pi F}{H\sqrt{1-(\frac{h}{H})^2}} \left\{ \frac{\sqrt{1-(\frac{h}{H})^2} - 1}{\frac{h}{H}} \right\}^n = 2a_0 p^n (-)^n$$

where

$$p = \frac{1-\sqrt{1-(\frac{h}{H})^2}}{h/H} = \frac{H}{h} - \sqrt{(\frac{H}{h})^2 - 1}$$

and

$$0 < p < 1$$

We now write for $\tilde{M}$

$$\tilde{M} = \sin[2a_0(1/2 - p\cos\omega t + p^2\cos 2\omega t - p^3\cos 3\omega t + \ldots)]$$

$$= \mathrm{Im}\left\{ e^{ia_0}\, e^{-2ia_0 p\cos\omega t}\, e^{2ia_0 p^2\cos 2\omega t}\, e^{-2ia_0 p^3\cos 3\omega t} \ldots \right\}$$

Making use of the identity

$$e^{-i\mu\cos y} = \sum_{n=-\infty}^{\infty} (-i)^n J_n(\mu)\, e^{-iny}$$

and its complex conjugate

$$e^{i\mu\cos y} = \sum_{n=-\infty}^{\infty} (i)^n J_n(\mu)\, e^{iny}$$

We obtain the following

$$\tilde{M} = \mathrm{Im}\left\{ e^{ia_0} \sum_{-\infty}^{\infty} (-i)^n J_n(2a_0 p)\, e^{-in\omega t} \sum_{-\infty}^{\infty} (i)^n J_n(2a_0 p^2)\, e^{2in\omega t} \ldots \right\}$$

$$= \mathrm{Im}\left\{ e^{ia_0} \sum_{n_1, n_2 \ldots = -\infty}^{\infty} \left[(i)^{\sum_k n_k}\right]\left[(-)^{k\mathrm{ODD}\ \sum n_k}\right]\left[\prod_{k=1}^{\infty} J_{n_k}(2a_0 p^k)\right] \left[e^{i\omega t \sum_k (-)^k k n_k}\right] \right\}$$

Again, we need the time derivative, which is easily obtained:

$$\frac{d\tilde{M}}{dt} = \mathrm{Im}\left\{ e^{ia_0} \sum_{n_1,n_2\ldots=-\infty}^{\infty} \left[(i)^{\sum_k n_k}\right]\left[(-)^{k\mathrm{ODD}\ \sum n_k}\right]\left[\prod_{k=1}^{\infty} J_{n_k}(2a_0 p^k)\right] \right.$$

$$\left. \times \left[e^{i\omega t \sum_k (-)^k k n_k}\right]\left[i\omega \sum_{k=1}^{\infty} (-)^k\, k n_k\right]\right\}$$

This is the exact solution for $\frac{d\tilde{M}}{dt}$, given that

$$\tilde{M} = \sin\left[\frac{2\pi F}{H + h\cos\omega t}\right]$$

The solution is valid for arbitrary h, provided only that $\frac{h}{H} < 1$.

In order to obtain a tractable and useful formula for $\frac{d\tilde{M}}{dt}$, it is necessary to find suitable approximations for the infinite sums and products in the exact solution. This can be done to any desired accuracy. We are usually interested in the phase-sensitive detection at a particular harmonic of the modulation frequency ω. For the nth time harmonic (nω), the required integers (±n) are related to the various integral indices occurring in the exact result by:

$$n = \left| \sum_{k=1}^{\infty} (-)^k k\, n_k \right|$$

where n_k can be any integer between $-\infty$ and ∞. This equation determines all the sets $\{n_k\}$ for any desired time-harmonic nω, each set giving one term in the solution. A procedure will now be given for ranking these sets in order of importance.

The part of the solution which determines the relative magnitude of a particular time harmonic is

$$\prod_{k=1}^{\infty} J_{n_k}(2a_0p^k)$$

In most cases, $2a_0p^k<<1$ for $k\geq 2$. In all cases, $2a_0p^k<<1$ for a large enough value of k, since $0<p<1$. For smaller values of k, all $J_{n_k}(2a_0p^k)$ are of order 1, and all must be considered. In the normal laboratory situation, there is but one such term.

When $2a_0p^k<<1$, which is usually the case for $k\geq 2$, one may rank the sets by their result in the following order of magnitude estimate. Given the set $\{n_k\}$, the corresponding term is approximately:

$$\prod_{k_c}^{\infty} \frac{(a_0p^k)^{n_k}}{n_k!}$$

where the product starts at a value k_c, which is the lowest integer satisfying $2a_0p^k<<1$ (typically $k_c = 2$). In practice, $n_k\neq 0$ only for small $k(k\leq 3)$, making this a quick method of ranking. One can see that the order depends somewhat on the values of a_0 and p.

Table III is an example of this ranking, along with the order of magnitude of the corresponding terms. It is done for the second time harmonic, and typical values were chosen for a_0 and p.

$n = 2,\ a_0 = 5 \times 10^2,\ p = 10^{-3}$

TABLE III

Ranking The Terms

Order of Mag.	n_1	n_2	n_3	n_4
1	± 2	0	0	0
10^{-3}	0	± 1	0	0
10^{-3}	± 4	± 1	0	0
10^{-6}	± 2	± 2	0	0
10^{-6}	∓ 1	0	± 1	0
10^{-9}	± 4	± 3	0	0
10^{-9}	± 1	± 1	± 1	0
10^{-9}	∓ 3	± 1	± 1	0
10^{-9}	∓ 3	∓ 1	± 1	0

The next term is of order 10^{-12}.

The most important term is invariably $n_1 = \pm n$, $n_k = 0$ for $k \neq 1$. We shall now calculate it separately, and compare it to the result for weak modulation.

$$\frac{d\tilde{M}}{dt} \approx \text{Im}\left\{ e^{ia_0}(-i)^n J_n(2a_0p) \prod_2^\infty J_0(2a_0p^k)\, e^{-in\omega t}(-in\omega) \right.$$

$$\left. + e^{ia_0}(i)^n(-)^n J_n(2a_0p) \prod_2^\infty J_0(2a_0p^k)\, e^{in\omega t}\,(in\omega) \right\}$$

$$= 2n\omega \sin(n\omega t)\, J_n(2a_0p) \prod_2^\infty J_0(2a_0p^k)\, \text{Im}\left\{ i\cdot i\cdot(-i)^n e^{ia_0} \right\}$$

$$\equiv 2n\omega\, J_n(2a_0p) \prod_2^\infty J_0(2a_0p^k) \sin(n\omega t) \sin(a_0 - \tfrac{n\pi}{2})$$

To compare this to the earlier conventional result, which started with the sine phase of the modulation, let us substitute $t \to t - \frac{\pi}{2\omega}$ to get

$$\frac{d\tilde{M}}{dt} \approx -2n\omega\, J_n(2a_0p) \prod_2^\infty J_0(2a_0p^k) \sin(n\omega t - \tfrac{n\pi}{2}) \sin(a_0 - \tfrac{n\pi}{2})$$

$$\equiv -2n\omega\, J_n(2a_0p) \prod_2^\infty J_0(2a_0p^k) \sin(n\omega t + \tfrac{n\pi}{2}) \sin(a_0 + \tfrac{n\pi}{2})$$

By contrast, the result for weak modulation is

$$\frac{d\tilde{M}}{dt} = -2n\omega\, J_n\left(\frac{2\pi Fh}{H}\right) \sin(n\omega t + \tfrac{n\pi}{2}) \sin\left(\frac{2\pi F}{H} + \tfrac{n\pi}{2}\right)$$

In comparison, there are two differences.

Firstly and perhaps most importantly, the measured dHvA frequency is different. The conventional result is F, whereas the exact result gives

$$\frac{F}{\sqrt{1 + (\frac{h}{H})^2}}$$

This means that there is a second order correction in the measured frequency. Under most circumstances, this shift is small, but given the high degree of accuracy which dHvA work boasts, this in some cases may be important. It is important to note that although only the first term in the solution was taken, this frequency correction is exact, that is, none of the higher terms change this result.

The other difference is the amplitude correction $\prod_{k=2}^{\infty} J_0(2a_0p^k)$.

Since $2a_0p \approx 1$, $2a_0p^k << 1$ for $k > 1$. One can show that this infinite product converges to ≤ 1. In the first order term, we can say that the amplitude for strong modulation is smaller than the conventional result, and also that it does not shift the zeros of the Bessel function.

The obvious alternative to expansion in a Fourier series is an expansion in a Taylor series, namely

$$\tilde{M} = \sin\left[\frac{2\pi F}{H + h\cos\omega t}\right]$$

$$= \sin\left[\frac{2\pi F}{H}\left(1 - \frac{h}{H}\cos\omega t + (\frac{h}{H})^2\cos^2\omega t - (\frac{h}{H})^3\cos^3\omega t + \ldots\right)\right]$$

Gathering all the terms for any harmonic $n\omega$ is a formidable task, but if we retain terms only to second order in $(\frac{h}{H})$, we

note that the dHvA frequency becomes

$$\frac{2\pi F}{H}\left(1 + \frac{1}{2}\left(\frac{h}{H}\right)^2\right)$$

which are the leading terms in a Taylor series of our exact result

$$\frac{2\pi F}{H}\left[\frac{1}{\sqrt{1 - \left(\frac{h}{H}\right)^2}}\right]$$

8.4 Modifications to the Apparatus and Analysis for the F $\sim$ 4 MG Search

The major consideration in the design of the detection apparatus was sensitivity and signal to noise. The shift in emphasis from the frequency response dictated several modifications. While the sample-detection coil arrangement remained the same, its output now drove the primary of a transformer (P.A.R. Model AM-1) to take advantage of the low output impedence ($\sim$ 100Ω) of the detection coils. The signal was detected on the second harmonic of a 41.7 Hz sinusoidal modulation field with a P.A.R. 124 phase-sensitive detector. Its notch filter (Q=50) was used to block the fundamental and a Krohn-Hite (model 3322R) bandpass filter (Q=1) was centered on the second harmonic.

The amplitude of the modulation was made to vary as H^2 which kept this amplitude spanning the same number of dHvA

cycles at any field H. Using the zeros of the Bessel function response of the observed magnetization on the modulation amplitude (see section 8.3), the dominant oscillations in any direction could be attenuated by about a factor of 50, allowing an increase in sensitivity of the same factor without saturation. The resulting signal was digitially recorded with 20 bit resolution on magnetic tape. These data were subsequently Fourier transformed with the use of the main U.B.C. computer (Amdahl 470) and a program outlined in Appendix C. With this arrangement, all of the oscillations in lead seen previously were easily identified, however, no sign of the 4 MG oscillations appeared. The search included examination of the Fourier transforms at the second harmonic ($\sim$ 8 MG) to allow for the possibility of a spin splitting zero at the first harmonic.

The result of this negative experiment places an upper bound on the amplitude of these long period oscillations in magnetization. In each of the three major symmetry directions [100],[110], [111], their amplitude must be less than 1 part in 10^4 of the magnetization of the dominant oscillations in each direction. This limit in absolute terms is about $A_{4MG} < 200\ \mu$ G.

The oscillations of Ivowi and Mackinnon (1976) and Tobin et.al.(1969) thus remain an enigma. It is felt that this area of study would benefit greatly by a collaboration of the feedback technique with the Shubnikov-de Haas effect or sound attenuation, where these oscillations appear vividly.

APPENDIX A

FLEXIBLE GEAR ROTATOR

An apparatus was built to rotate the sample about an axis which was 90° away from the axis of the magnet bore (the only direction of access) based on an idea given by Pippard and Sadler (1969). The modifications made to the original design were extensive enough to warrant further description in this appendix. Our compactness requirement restricted the size of the apparatus to a degree where the mechanisms would be substantially smaller than any that had previously been built successfully.

The entire apparatus is constructed from nylon rod except for a Mylar gear. This circular Mylar gear was cut from a piece of 0.003 inches thick sheet. A special jig was made to cut 32 triangular teeth with a razor blade in roughly circular starting material. A square hole (side length 0.075 inch) was cut in the centre with a punch. Through the square hole, a retainer fastened a ring to the gear so that the axis of the ring was perpendicular to the gear axis, and

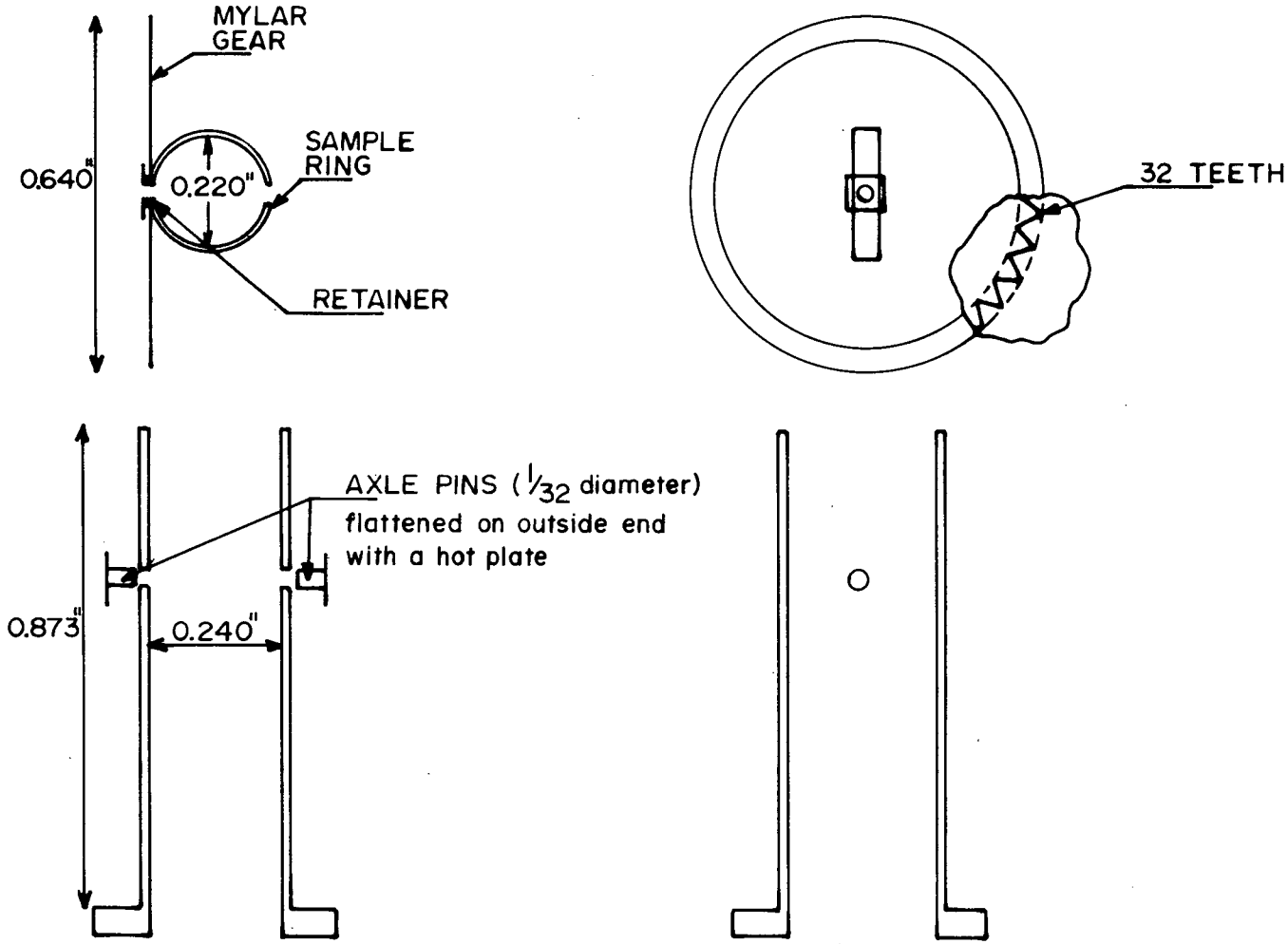

Figure 28. Sample Rotator Assembly

intersecting it(see Figure 28). The retainer, so placed, was welded to the ring with a soldering iron. The square hole ensured the absence of slipping when the gear was turned. The spherical sample was glued to the ring with a small drop of G.E. varnish. Care was taken to apply a minimum amount of varnish to the sample as differential contraction would cause strain upon cooling.

After allowing 24 hours for the varnish to dry, the assembly was placed inside a cylindrical tube by bending the Mylar gear to conform to the shape of the tube. When in place, small axle pins held the gear axis stationary while still allowing it to rotate. As the gear rotates, it flexes to retain its cylindrical shape, and rotates the sample about the axis of the gear. Only the teeth at the top of the gear protrude from the cylinder, where they mesh with a driving gear. The 16 tooth driving gear was made by pushing a hot brass negative into a cylindrical nylon blank, and subsequent machining provided a coupling to the top of the cryostat. The body of the coil former held the driving gear in the proper place to mesh with the Mylar gear. In order to keep the teeth of the driving gear identical to those of the Mylar gear, one finds that the driving gear must rotate about an axis which is off centre. The driving gear with the rotator assembly and coil former is shown in Figure 29. A beryllium-copper spring was used to ensure intimate contact of the gears when cooled

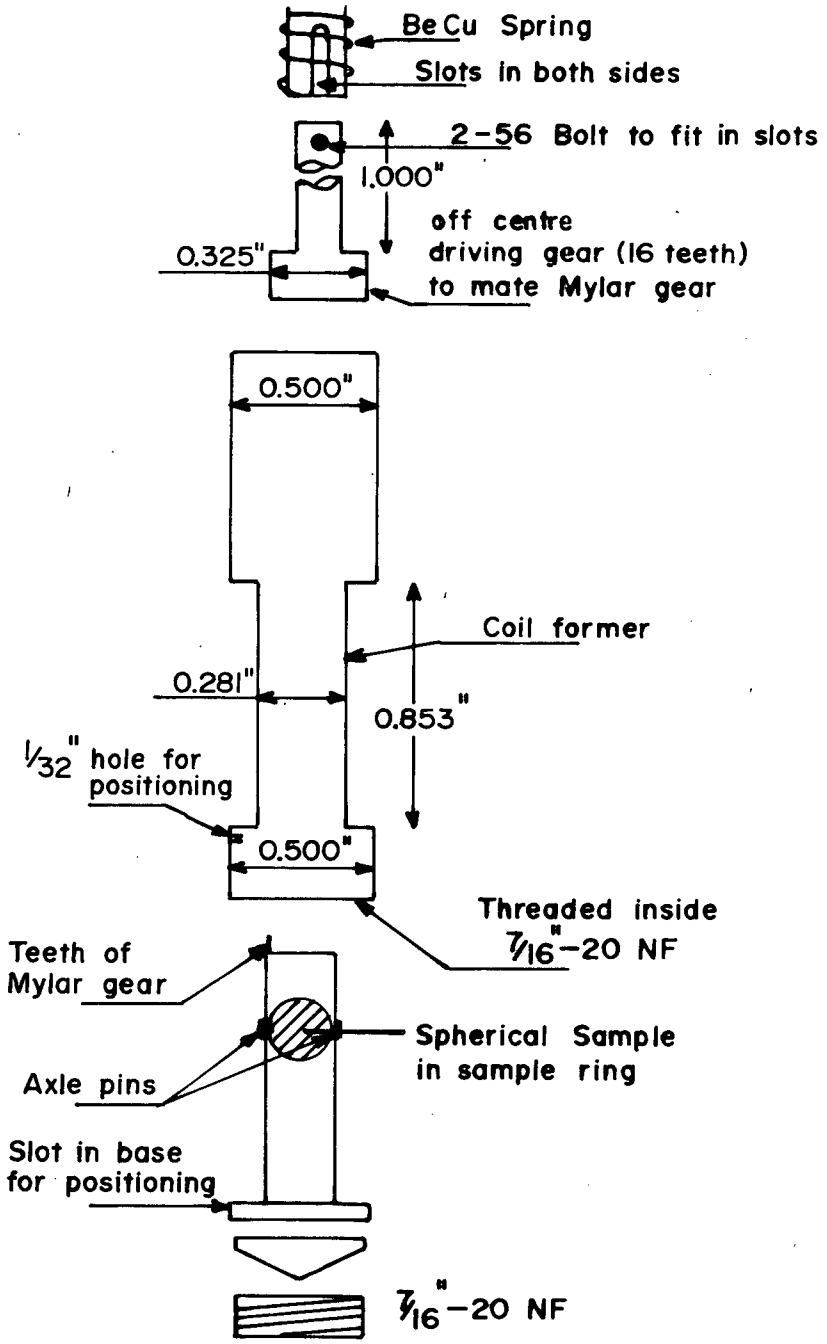

Figure 29. Sample Rotator With Driving Gear, and Coil Former

to liquid helium temperatures. The cylinder holding the sample was inserted into the bottom of the coil former and held rigidly with a 7/16-20 (NF) nylon bolt. The location of its proper rotational position was found by pushing a temporary wire through a small hole in the bottom of the coil former, and into a slot milled into the base of the sample cylinder. This wire was removed after tightening the nylon bolt.

The entire assembly was inserted into the tail of the inner dewar shown in Figure 5. At the top of the cryostat, provision was made to rotate the crystal either by hand, or by electric motor.

APPENDIX B

THE DISCRETE FOURIER TRANSFORM

Since both the spectrum analyzer, and the computer programs use discrete Fourier transforms, the basic definitions will be presented in this appendix. The discrete Fourier transform is defined by

$$A(k) = \sum_{j=0}^{N-1} X_j \, e^{-2\pi i j \, k/N} \qquad k = 0, 1, \ldots, N-1$$

where X_j, $j = 0, 1, \ldots, N-1$ is a set of complex numbers .

The inverse transform is

$$B(j) = \sum_{k=0}^{N-1} A(k) \, e^{2\pi i j \, k/N} \qquad j = 0, 1, \ldots N-1$$

where $B(j) = NX_j$.

The fast Fourier transform programs supplied by libraries often require the input data to be either symmetric or anti-symmetric. Any set of data can be separated into its anti-symmetric and symmetric components. If the set X_i contains

the original data values, then the antisymmetric values are given by

$$X^a_{N/2+1-j} = \frac{1}{2}\ (X_{N/2-j+1} - X_{N/2+j+1})\ \ j=2,\ \ldots\ N/2 - 1$$

$$X^a_1 = X^a_{N/2} = 0.$$

A sine transform can then be applied to X^a. The symmetric values X^S_i are given by

$$X^S_{N/2+1-j} = \frac{1}{2}\ (X_{N/2+j+1} = X_{N/2-j+1})\ \ j=2,\ \ldots\ N/2 - 1$$

$$X^S_1 = X_1,\ X^S_{N/2} = X_{N/2}.$$

A cosine transform can then be applied to X^S.

Applying a window to the original data values usually results in a tradeoff of resolution and sidelobes. The large sidelobes encountered in the use of a square window can hide frequencies of smaller amplitude which are actually far away in the space of the variable k.

The Hanning window is a good compromise, since not much resolution is lost, but the sidelobe amplitude decays very quickly in k space. If the original data is in time t, application of a Hanning window simply involves multiplication of the original data by $\sin^2[\pi(t-t_0)/T]$ where t_o is the

smallest value of t and T is the duration of the record. In effect, the Hanning window rounds off the sharp corners on the edges of the data where the window is opened and closed.

APPENDIX C

COMPUTER PROGRAMS

The computer programs used to generate the results in the body of this thesis are listed in this appendix. For the most part, the programs are written to be self explanatory in regards to their use.

The "Data Reading and Adjusting" program reads the data from the Stevenson interface* after it has been converted to EBDIC from ASCII. The conversion was done by a standard translation routine (*TRANS) in the U.B.C. Computer library. After reading the data, the Fortran program, by use of the function sub-programs, allows the user to create the proper x and y coordinates from the available data. The program then converts the data to a format compatible with all of the remaining programs.

The "Synthetic Data Generator" program allows the user to create any data he pleases and puts it in the proper format. This program was largely used to test the other programs, and

---

*Built by A. Stevenson presently at TRIUMF.

check the resolution.

The "Window" program was used to cut down the side-lobes of the transform. Instead of using the Hanning window, the data were multiplied by a simple sine function spanning 0-π over the window. This gives more resolution than the Hanning window, and the sidelobes are still not too large. This sine window was used because the data at one end of the window (the high field end) were the most important, and they were not cut off so drastically as with the Hanning window.

The analysis program takes the Fourier transform of the data prepared by the earlier routines. One can choose the resolution and the window in k space for the transform. The power spectrum feature was most often used.

The "Plotting" program accepts data from all of the previous routines so that real space and Fourier space data can be plotted. Plotting can be done on the printer, the graphics terminal, or the hard copy Calcomp plotter. The 1/H axis is labelled in the printer plots.

The M.I. Simulation program uses the formulae developed for M.I. in Chapter II, and calculates the result of our experiment described in Chapter VI.

Data Reading and Adjusting

```
1            DIMENSION A(50),D(50)
2            DATA CHAR1/'A'/
3            DATA CHAR2/'D'/
4            PRINT 314
5         314  FORMAT(' NUMBER OF RECORDS? (*25=NUMBER OF DATA PT PAIRS) (I4) ')
6            READ 315,NNN
7         315  FORMAT(I4)
8            NPP=25*NNN
9            WRITE(2,91)NPP
10        91   FORMAT(I5)
11           DO 20 LINE=1,NNN
12           READ(3,1)(A(I),D(I),I=1,50)
13        1    FORMAT(50(A1,1X,F8.0))
14           DO 2 I=1,50,2
15           I1=I+1
16        C  IF(A(I).NE.CHAR1.OR.A(I1).NE.CHAR2) PRINT3,LINE
17        3    FORMAT(' ABNORMALITY IN LINE',I3)
18           D(I)=YFUN(D(I1),D(I))
19           D(I1)=XFUN(D(I1),D(I))
20        2    CONTINUE
21           WRITE(2,21)(D(I),D(I+1),I=2,50,2)
22        21   FORMAT(2E14.7)
23        20   CONTINUE
24           STOP
25           END
26           FUNCTION YFUN(X,Y)
27           YFUN=Y*10.
28           RETURN
29           END
30           FUNCTION XFUN(X,Y)
31           XFUN=1./(1.229*X)
32           RETURN
33           END
```

Synthetic Data Generator

```
      DIMENSION PT(1000)
      PI=3.1415926
      PRINT 200
200   FORMAT(' ENTER NUMBER OF DATA POINT PAIRS(I4)')
      READ 201,NNN
201   FORMAT(I4)
      WRITE(2,205)NNN
205   FORMAT(I5)
      PRINT 202
202   FORMAT(' ENTER HMIN,HMAX IN MS, (2F6.0)')
      READ 203,HMIN,HMAX
203   FORMAT(2F6.0)
      HINC=(HMAX-HMIN)/FLOAT(NNN)
      DO 100 I=1,1000
      PT(I)=0.
100   CONTINUE
      PRINT 1
1     FORMAT('TO CREATE THE SUM OF T*EXP(-B*T)*COS(2.*PI*A*T+D)...T=1/H'/
     1' ENTER B,A,D...(3F6.0)...OR ZERO TO STOP')
6     READ 2,B,A,D
2     FORMAT(3F6.0)
      IF(A.EQ.0.) GO TO 99
      PRINT 7,B,A,D
7     FORMAT(3E10.3)
      H=HMAX
5     DO 3 I=1,NNN
      H=H-HINC
      T=1./H
      PT(I)=PT(I)+T*EXP(-B*T)*COS(2.*PI*A*T+D)
3     CONTINUE
      GO TO 6
99    H=HMAX
      T=1./H
      DO 101 I=1,NNN
      H=H-HINC
      T=1./H
      WRITE(2,4)T,PT(I)
4     FORMAT(2E14.7)
101   CONTINUE
      STOP
      END
```

Window

```
1             DIMENSION X(1000),Y(1000)
2             PI=3.1415926
3             READ(3,1)NNN
4       1     FORMAT(I5)
5             WRITE(2,6)NNN
6       6     FORMAT(I5)
7             DO 2 I=1,NNN
8             READ(3,3)X(I),Y(I)
9       3     FORMAT(2E14.7)
10      2     CONTINUE
11            F=PI/(X(NNN)-X(1))
12            DO 4 I=1,NNN
13            Y(I)=Y(I)*SIN(F*(X(I)-X(1)))
14            WRITE(2,5)X(I),Y(I)
15      5     FORMAT(2E14.7)
16      4     CONTINUE
17            STOP
18            END
```

Analysis Program

```
      REAL T(1000),PT(1000)
      PI2=2.*3.14159265
      READ(3,315)NNN
  315 FORMAT(I5)
      XNNN=FLOAT(NNN)
      DO 9 I=1,NNN
      READ(3,10)T(I),PT(I)
   10 FORMAT(2E14.7)
    9 CONTINUE
      PRINT 1
    1 FORMAT('0ANALYSIS?')
      READ 2,INAL
    2 FORMAT(I1)
      GO TO(3,4,5,6,7,99),INAL
   99 STOP
    3 PRINT 70
   70 FORMAT('0FOURIER REAL TRANSFORM'/' FMIN,FMAX,NUMF?(2F6.0,I4)')
      READ 8, FMIN,FMAX,NUMF
    8 FORMAT(2F6.0,I4)
      WRITE(2,437)NUMF
  437 FORMAT(I5)
      FINC=(FMAX-FMIN)/FLOAT(NUMF)
      F=FMIN
      DO 11 I=1,NUMF
      SUM=0.
      DO 12 J=1,NNN
      SUM=SUM+PT(J)*COS(PI2*F*T(J))
   12 CONTINUE
      SUM=SUM/XNNN
      WRITE(2,13) F,SUM
   13 FORMAT(2E14.7)
      F=F+FINC
   11 CONTINUE
      STOP
    4 PRINT 34
   34 FORMAT('0FOURIER IMAGINARY TRANSFORM'/' FMIN,FMAX,NUMF?(2F6.0,I4)')
      READ 8,FMIN,FMAX,NUMF
      WRITE(2,437)NUMF
      FINC=(FMAX-FMIN)/FLOAT(NUMF)
      F=FMIN
      DO 31 I=1,NUMF
      SUM=0.
      DO 32 J=1,NNN
      SUM=SUM+PT(J)*COS(PI2*F*T(J))
   32 CONTINUE
      SUM=SUM/XNNN
      WRITE(2,13)F,SUM
      F=F+FINC
   31 CONTINUE
      STOP
    5 PRINT 54
   54 FORMAT('0POWER SPECTRUM'/' FMIN,FMAX,NUMF?(2F6.0,I4)')
      READ 8,FMIN,FMAX,NUMF
      WRITE(2,437)NUMF
      FINC=(FMAX-FMIN)/FLOAT(NUMF)
      F=FMIN
      DO 51 I=1,NUMF
```

```
      SUM1=0.
      SUM2=0.
      DO 52 J=1,NNN
      SUM1=SUM1+PT(J)*COS(PI2*F*T(J))
      SUM2=SUM2+PT(J)*SIN(PI2*F*T(J))
52    CONTINUE
      SUM=(SUM1/XNNN)**2+(SUM2/XNNN)**2
      WRITE(2,13)F,SUM
      F=F+FINC
51    CONTINUE
      STOP
6     PRINT 74
74    FORMAT('0LAPLACE TRANSFORM!/' SMIN,SMAX,NUMS?(2F6.0,I4)!')
      READ 8,SMIN,SMAX,NUMS
      WRITE(2,437)NUMS
      SINC=(SMAX-SMIN)/FLOAT(NUMS)
      S=SMIN
      DO 71 I=1,NUMS
      SUM=0.
      DO 72 J=1,NNN
      SUM=SUM+PT(J)*EXP(-S*T(J))
72    CONTINUE
      SUM=SUM/XNNN
      WRITE(2,13)S,SUM
      S=S+SINC
71    CONTINUE
      STOP
7     PRINT 94
94    FORMAT('0LAPLACE-POWER SPECTRUM!/' SMIN,SMAX,NUMS?(2F6.0,I4)!')
      READ 8,SMIN,SMAX,NUMS
      WRITE(2,437)NUMS
      PRINT 105
105   FORMAT(' THE ANGULAR FREQUENCY?!')
      READ 106,A
106   FORMAT(F6.0)
      SINC=(SMAX-SMIN)/FLOAT(NUMS)
      S=SMIN
      DO 91 I=1,NUMS
      SUM1=0.
      SUM2=0.
      DO 92 J=1,NNN
      SUM1=SUM1+PT(J)*EXP(-S*T(J))*COS(A*T(J))
      SUM2=SUM2+PT(J)*EXP(-S*T(J))*SIN(A*T(J))
92    CONTINUE
      SUM=(SUM1/XNNN)**2+(SUM2/XNNN)**2
      WRITE(2,13)S,SUM
      S=S+SINC
91    CONTINUE
      STOP
      END
```

Plotting

```
      DIMENSION X(1000),Y(1000),CHAR(2)
      LOGICAL*1 QUE
      REAL L(75)
      DATA CHAR/' ','*'/
C  READ IN THE DATA
      READ(3,2)N
 2    FORMAT(I5)
      XMAX=-1.E+50
      YMAX=XMAX
      XMIN=1.E+50
      YMIN=XMIN
      DO 3 I=1,N
      READ(3,4)X(I),Y(I)
 4    FORMAT(2E14.7)
      IF(X(I).LT.XMIN)XMIN=X(I)
      IF(X(I).GT.XMAX)XMAX=X(I)
      IF(Y(I).LT.YMIN)YMIN=Y(I)
      IF(Y(I).GT.YMAX)YMAX=Y(I)
 3    CONTINUE
C  FIND SCALING FACTORS
      XS=8./(XMAX-XMIN)
      YS=8./(YMAX-YMIN)
      XSP=50.*XS/8.
      YSP=50.*YS/8.
C  PRINTER PLOT
      PRINT 7
 7    FORMAT(' DO YOU WISH A PRINTER PLOT?...KINDLY ENTER Y OR N')
      READ 8,QUE
 8    FORMAT(A1)
      IF(LCOMC(1,QUE,'Y').NE.0)GO TO 9
      PRINT 10
 10   FORMAT(' HOW MANY PRINTER PAGES WOULD YOU LIKE?...(I2)')
      READ 11,NP
 11   FORMAT(I2)
      INC=N/(NP*60)
      DO 14 I=1,75
      L(I)=CHAR(1)
 14   CONTINUE
      IPNT=1
      DO 12 I=1,N,INC
      L(IPNT)=CHAR(1)
      IPNT=IFIX((Y(I)-YMIN)*YSP+1)
      L(IPNT)=CHAR(2)
      WRITE(2,15)X(I),Y(I),(L(J),J=1,75)
 15   FORMAT(' ',2(E14.7,1X),'(',75A1)
 12   CONTINUE
 9    PRINT 16
 16   FORMAT(' DO YOU WISH A PEN PLOT?...(Y,N)')
      READ 17,QUE
 17   FORMAT(A1)
      IF(LCOMC(1,QUE,'Y').NE.0)STOP
C  PLOT
      CALL PLOT(XS*(X(1)-XMIN),YS*(Y(1)-YMIN),3)
      DO 5 I=2,N
      CALL PLOT(XS*(X(I)-XMIN),YS*(Y(I)-YMIN),2)
 5    CONTINUE
      CALL PLOTND
```

M.I. Simulation

```
      DIMENSION XA1(500),XA2(500),XA3(500)
      DIMENSION XM(512),X1(256),X2(256)
      REAL M,NUD,KAPPA,NCYC
      INTEGER Y,SM
      COMMON XA1MAX,XA2MAX,XA3MAX,HIMAX,HIMIN
      DATA Y/'Y'/
      PSI(RDUM)=ATAN(ETA*TAN(PI*RDUM*DELF*HI-PI/4.))
      A(RDU,AADU)=(AADU+AADU*(1.-ETA)/(1.+ETA))*(SQRT(2.)/2.)*
     1SQRT((1.+ETA*ETA)+(1.-ETA*ETA)*SIN(2.*PI*RDU*DELF*HI))
      M(NUD,ALPHAD)=A1*SIN(X+PSI(1.))
     1+A2*(SIN(2.*X+PSI(2.))-0.5*NUD*SIN(2.*X+2.*PSI(1.)))
     2+A3*(SIN(3.*X+PSI(3.))-1.5*NUD*ALPHAD*
     3 (SIN(3.*X+PSI(1.)+PSI(2.))-0.25*NUD*SIN(3.*X+3*PSI(1.))))
      AT(AB,BB,AL,BL)=SQRT((AB*SIN(AL)+BB*SIN(BL))**2
     1                    +(AB*COS(AL)+BB*COS(BL))**2)
      PI=3.14159
      PRINT 1
    1 FORMAT(' PLEASE ENTER AMPLITUDES OF THE HIGHEST FREQUENCY'/
     1' FIRST,SECOND, AND THIRD HARMONIC (IN GAUSS), AND ETA...(4F4.0)')
      READ 2,AA1,AA2,AA3,ETA
    2 FORMAT(4F4.0)
      AA1=AA1/1000.
      AA2=AA2/1000.
      AA3=AA3/1000.
      PRINT 3
    3 FORMAT(' PLEASE ENTER EPSILON,AND DELTA...(2F4.0)')
      READ 4,EPSIL,DELTA
    4 FORMAT(2F4.0)
      PRINT 5
    5 FORMAT(' PLEASE ENTER THE MEAN FREQUENCY F,'/
     1' AND THE DIFFERENCE IN FREQUENCY DELF(IN MG)...(2F4.0)')
      READ 6,F,DELF
    6 FORMAT(2F4.0)
      F=1000.*F
      DELF=1000.*DELF
      HKAPPA=8.*PI*PI*(1.-DELTA)*F
      PRINT 9
    9 FORMAT(' DO YOU WISH A NON-SMEARED PLOT?...(Y,N)')
      READ 10,NSM
   10 FORMAT(A1)
      IF(NSM.NE.Y)GO TO 200
      PRINT 7
    7 FORMAT(' PLEASE ENTER HMIN,HMAX (IN KG),NUMH...(2F4.0,I3)')
      READ 8,HMIN,HMAX,NUMH
    8 FORMAT(2F4.0,I3)
C   CALCULATE THE NON-SMEARED AMPLITUDE
      HIMIN=1./HMAX
      HIMAX=1./HMIN
      HIINC=(HIMAX-HIMIN)/FLOAT(NUMH)
      HI=HIMIN
      XA1MAX=0.
      XA2MAX=0.
      XA3MAX=0.
      DO 100 I=1,NUMH
      HI=HI+HIINC
      KAPPA=HKAPPA*HI*HI
      A1=A(1.,AA1)
```

```
      XA1(I)=A1
      IF(XA1(I).GT.XA1MAX)XA1MAX=XA1(I)
      A2=A(2.,AA2)
      PSI2=PSI(2.)
      PSI1=PSI(1.)
      XA2(I)=AT(A2,-.5*KAPPA*A1*A1*EPSIL,PSI2,2.*PSI1)
      IF(XA2(I).GT.XA2MAX)XA2MAX=XA2(I)
      A3=A(3.,AA3)
      PSI3=PSI(3.)
      AINT=AT(1.,-0.25*KAPPA*A1*A1/A2*EPSIL,PSI1+PSI2,3.*PSI1)
      PSIINT=ATAN((COS(PSI1+PSI2)-0.25*KAPPA*A1*A1/A2*EPSIL*COS(3.*PSI1
     1          ))/(SIN(PSI1+PSI2)-0.25*KAPPA*A1*A1/A2*EPSIL*SIN(3.*PSI1
     2)))
      XA3(I)=A3*AT(1.,-1.5*A2*A2/(A1*A3)*KAPPA*A1*A1/A2*EPSIL*AINT,PSI3
     1,PSIINT)
      IF(XA3(I).GT.XA3MAX)XA3MAX=XA3(I)
  100 CONTINUE
C  NORMALIZE
      DO 101 I=1,NUMH
      XA1(I)=XA1(I)/XA1MAX*10.
      XA2(I)=XA2(I)/XA2MAX*10.
      XA3(I)=XA3(I)/XA3MAX*10.
  101 CONTINUE
C  PLOT
      XSCALE=15./FLOAT(NUMH)
      CALL PLSTR(ETA,EPSIL)
      CALL PLOT(2.,XA1(1),3)
      DO 102 I=2,NUMH
      CALL PLOT(XSCALE*FLOAT(I)+2.,XA1(I),2)
  102 CONTINUE
      CALL PLOT(2.,XA2(1),3)
      DO 103 I=2,NUMH
      CALL PLOT(XSCALE*FLOAT(I)+2.,XA2(I),2)
  103 CONTINUE
      CALL PLOT(2.,XA3(1),3)
      DO 104 I=2,NUMH
      CALL PLOT(XSCALE*FLOAT(I)+2.,XA3(I),2)
  104 CONTINUE
C  SMEARED AMPLITUDE
  200 IF(NSM.EQ.Y)CALL PLOT(22.,0.,-3)
      PRINT 11
   11 FORMAT(' DO YOU WISH A SMEARED PLOT?...(Y,N)')
      READ 12,SM
   12 FORMAT(A1)
      IF(SM.NE.Y)GO TO 999
      PRINT 15
   15 FORMAT(' ENTER THE P-P MODULATION IN KG (F4.0)')
      READ 16, PPMOD
   16 FORMAT(F4.0)
      PRINT 17
   17 FORMAT(' PLEASE ENTER HMIN,HMAX (IN KG),AND NUMH...',
     1'(2F4.0,I3)')
      READ 18,HMIN,HMAX,NUMH
   18 FORMAT(2F4.0,I3)
      HIMIN=1./HMAX
      HIMAX=1./HMIN
      CALL PLSTR(ETA,EPSIL)
      PMOD=PPMOD/2.
      HIINC=(HIMAX-HIMIN)/FLOAT(NUMH)
      HI =HIMIN
```

```
      XA1MAX=0.
      XA2MAX=0.
      XA3MAX=0.
      DO 300 I=1,NJMM
      HI=HI+HTINC
      HIMINC=(1./(1./HI-PMOD)-1./(1./HI+PMOD))/512.
      HANF=PI/(HIMINC*512.)
      HIMS=1./(1./HI+PMOD)
      HIM=HIMS
C  GENERATE THE SIGNAL FROM ONE MODULATION SWEEP
      DO 301 J=1,512
      HIM=HIM+HIMINC
      KAPPA=HKAPPA*HT*HI
      A1=A(1,,AA1)
      A2=A(2,,AA2)
      A3=A(3,,AA3)
      X=2.*PI*(F*HIM-.5)
C  THE SINE IN THE NEXT LINE IS THE HANNING WINDOW
      XM(J)=M(EPSIL*KAPPA*A1*A1/A2,A2*A2/(A1*A3))*
     1SIN(HANF*(HIM-HIMS))
  301 CONTINUE
C  SEPARATE XM INTO ITS ANTISYMMETRIC (X1),AND SYMMETRIC (X2)
C  COMPONENTS
      DO 302 J=2,255
      X1(257-J)=(XM(257-J)-XM(257+J))/2.
      X2(257-J)=(XM(257-J)+XM(257+J))/2.
  302 CONTINUE
      X1(1)=0.
      X1(256)=0.
      X2(1)=XM(1)
      X2(256)=XM(256)
C  TAKE THE FOURIER TRANSFORM
      CALL S512(X1,X1)
      CALL C512(X2,X2)
C  CALCULATE THE FIELD SPACING OF THE FIRST HARMONIC
      FSP1=1./(HI*HI*F)
C THE NUMBER OF CYCLES PER MOD SWEEP...
      NCYC=PPMOD/FSP1
C  THIS IS WHERE THE FIRST HARMONIC IS IN THE TRANSFORM
C  FORM WINDOWS
      IWL1=NCYC/2.+1.
      IWL2=NCYC*1.5+1.
      IWL3=NCYC*2.5+1.
      IWR3=NCYC*3.5+1.
C  FIND THE MAXIMA OF THE AMPLITUDE SPECTRUM...
      XMAX=0.
      DO 310 J=IWL1,IWL2
      AMP=SQRT(X1(J)**2+X2(J)**2)
      IF (AMP.GT.XMAX)XMAX=AMP
  310 CONTINUE
      XA1(I)=XMAX
      IF(XMAX.GT.XA1MAX)XA1MAX=XMAX
      XMAX=0.
      DO 311 J=IWL2,IWL3
      AMP=SQRT(X1(J)**2+X2(J)**2)
      IF(AMP.GT.XMAX)XMAX=AMP
  311 CONTINUE
      XA2(I)=XMAX
      IF(XMAX.GT.XA2MAX)XA2MAX=XMAX
      XMAX=0.
```

```
178           DO 312 J=IWL3,IWR3
179           AMP=SQRT(X1(J)**2+X2(J)**2)
180           IF(AMP.GT.XMAX)XMAX=AMP
181       312 CONTINUE
182           XA3(I)=XMAX
183           IF(XMAX.GT.XA3MAX)XA3MAX=XMAX
184       300 CONTINUE
185       C   PLOT...
186       C   FIRST HARMONIC IN SQUARES,
187       C   SECOND HARMONIC IN TRIANGLES,
188       C   THIRD HARMONIC IN X'S
189       C
190       C   NORMALIZE
191           DO 320 I=1,NUMH
192           XA1(I)=XA1(I)/XA1MAX*10.
193           XA2(I)=XA2(I)/XA2MAX*10.
194           XA3(I)=XA3(I)/XA3MAX*10.
195       320 CONTINUE
196       C   PLOT
197           XSCALE=15./FLOAT(NUMH)
198           DO 403 I=1,NUMH
199           XPNT=XSCALE*FLOAT(I)+2.
200           CALL SYMBOL(XPNT,XA1(I),.14,0,0.,-1)
201           CALL SYMBOL(XPNT,XA2(I),.14,2,0.,-1)
202           CALL SYMBOL(XPNT,XA3(I),.14,4,0.,-1)
203       403 CONTINUE
204       999 CALL PLOTND
205           STOP
206           END
207           SUBROUTINE PLSTR(ETA,EPSIL)
208           COMMON XA1MAX,XA2MAX,XA3MAX,HIMAX,HIMIN
209           CALL AXIS(1.,0.,'FIRST HARMONIC AMPLITUDE',24,10.,90.,
210          10.,XA1MAX*100.)
211           CALL AXIS(1.5,0.,'SECOND HARMONIC AMPLITUDE',25,10.,
212          190.,0.,XA2MAX*100.)
213           CALL AXIS(2.,0.,'THIRD HARMONIC AMPLITUDE',24,10.,
214          190.,0.,XA3MAX*100.)
215           CALL AXIS(2.,0.,'1/H(KG**-1)',-11,15.,0,0,HIMIN,
216          1(HIMAX-HIMIN)/15.)
217           CALL PLOT(2.,10.,3)
218           CALL PLOT(17.,10.,2)
219           CALL PLOT(17.,0.,2)
220           CALL SYMBOL(17.2,10.,.28,22,0.,-1)
221           CALL SYMBOL(17.48,10.,.28,'=',0.,1)
222           CALL NUMBER(17.76,10.,.28,ETA,0.,2)
223           CALL SYMBOL(17.2,9.,.28,20,0.,-1)
224           CALL SYMBOL(17.48,9.,.28,'=',0.,1)
225           CALL NUMBER(17.76,9.,.28,EPSIL,0.,2)
226           RETURN
227           END
```

BIBLIOGRAPHY

Anderson, J.R. and Gold, A.V. Phys. Rev. 139, No. 5A, A1459 (1965).

Aoki, H. and Ogawa, K. J. Low Temp. Phys. 32 131 (1978).

Condon, J.H. Phys. Rev. 145, 526 (1966).

Condon, J.H., and Walstedt, R.E. Phys. Rev. Lett. 21 612 (1968).

Dingle, R.B. Proc. Roy. Soc. (London) A211, 500 (1952).

Dingle, R.B. Proc. Roy. Soc. (London) A211, 517 (1952).

Everett, P.M. and Grenier, C.G. Phys. Rev. B 18, 4477 (1978).

Gradshyeyn, I.S. and Ryzhik, I.M. Tables of Integrals and Products, Academic Press, N.Y., London (1965).

Gold, A.V. and Schmor, P.W. Can. J. Phys. 54, 2445 (1976).

Ivowi, U.M.O. and Mackinnon, L. J. Phys. F 6, 329 (1976).

Knecht, B. J. Low Temp. Phys. 21, 619 (1975).

Lifshitz, I.M. and Kosevich, A.M. Soviet Phys. - JETP 2, 636 (1956).

Ogawa, K. and Aoki, H., J. Phys. F. 8, 1169 (1978).

Onsager, L. Phil. Mag. 43, 1006 (1952).

Perz, J.M. and Shoenberg, D.J. Low Temp. Phys. 25, 275 (1976).

Phillips, R.A. and Gold, A.V. Phys. Rev. 178, 932 (1969).

Pippard, A.B. Physics of Metals, Vol. 1 : Electrons, ed. by J.M. Ziman, Cambridge University Press, London, P.113 (1969).

Pippard, A.B. and Sadler, F.T. J. Sci. Inst. series 2 2, 101 (1969).

Shoenberg, D. Phil. Trans. Roy. Soc. (London) A255, 85 (1962).

Testardi, L.R. and Condon, J.H. Phys. Rev. B 1, 3928 (1970).

Tobin, P.J., Sellmyer, D.J. and Averbach, B.L. Phys. Lett 28A, 723 (1969).

van Weeren, J.H. and Anderson, J.R. J. Phys. F 3 p.2109 (1973).